X-RAY DIFFRACTION ANALYSIS OF RESIDUAL STRESS IN ZIRCONIA DENTAL COMPOSITES

By

MASOUD ALLAHKARAMI

Bachelor of Science in Physics
Tarbiat Moalem University
Tehran, Iran
2002

Master of Science in Physics
Urmia University
Urmia, Iran
2005

Submitted to the Faculty of the
Graduate College of the
Oklahoma State University
in partial fulfillment of
the requirements for
the Degree of
DOCTOR OF PHILOSOPHY
December, 2012

X-RAY DIFFRACTION ANALYSIS OF RESIDUAL

STRESS IN ZIRCONIA DENTAL COMPOSITES

Dissertation Approved:

Dr. Jay C. Hanan

Dissertation Adviser

Dr. Raman P. Singh

Committee Member

Dr. Khaled A. Sallam

Committee Member

Dr. Tyler Ley

Outside Committee Member

ACKNOWLEDGEMENTS

All my praises and thanks are to the God, the most gracious and the most merciful. I would like to express my heartfelt appreciation to my advisor Dr. Jay C. Hanan for giving me opportunity to work on this project and his continuous encouragement and supports with innovative ideas.

I am thankful of my committee members Dr. Khaled A. Sallam, Dr. Tyler Ley, and Dr. Raman P. Singh. I greatly appreciate helps from Dr. Ken Ede and trying to remember his advice to me “When God closes one door, He opens another”. I acknowledge the assistance from P. Coelho, V. Thompson, E. D. Rekow and M. Cabrera at NYU Dental College and CEO Nautilus dental Studio which provided the samples.

I am grateful to my infinite sources of love, my Dad, Reza Allahkarami, who was my first and great physics teacher and my Mom, Nahid Gholami for being a foundation for all that I have. I am very thankful of my wife Leila Seyed Faraji who has always believed in me and supported me with love through this long way. I am thankful of my extended Seyed Faraji family for all their love and support. I would like to express my thanks and love to my sisters Fatemeh and Maryam Allahkarami. A great deal of help was offered by Dr. Hrishikesh A. Bale from time to time, my best word to acknowledge him is to say, “He is my best college friend”. I thank my fellow Lab mates, Sudheer bandla, Balaji Jayakumar, Advait Bhat, Dr. Yanli Zhang, Reaj Ahmed, Praful Bari, Rohit Vaidya, Ranjan Mahadevan, and Arjun Rajakutty, for all their help and wonderful support. I would like to thanks my friends in MAML group, Kunal Mishra, Arif Rahman, Abhishek Jain, Salahuddin Hamim, Chaitanya, Balaji, Vasu, Austin, Suman, Dhivakar, Abhishek Bhadra, Sadia Nasrin and my HRC friends Mohsen, Payam, Parvaneh, Nahida, Zahra, Hedieh and Jeff.

Research support provided by the Oklahoma Health Research award (project number HR07-134), from the Oklahoma Center for the Advancement of Science and Technology (OCAST) and supported through financial support from the Helmerich Foundation supporting Tulsa’s Vision 2025 and the Helmerich Research Center in Tulsa OK., I would like to express my sincere thanks to them.

Name: MASOUD ALLAHKARAMI

Date of Degree: DECEMBER, 2012

Title of Study: X-RAY DIFFRACTION ANALYSIS OF RESIDUAL STRESS IN ZIRCONIA DENTAL COMPOSITE

Major Field: MECHANICAL ENGINEERING

Abstract:

Dental restoration ceramic is a complex system to be characterized. Beside its essential biocompatibility, and pleasant appearance, it requires being mechanically strong in a catastrophic loading environment. Any design is restricted with geometry boundary and material property limits. Inspired by natural teeth, a multilayer ceramic is a smart way of achieving an enhanced restoration. Bi-layers of zirconia core covered by porcelain are known as one of the best multilayer restorations. Residual stresses may be introduced into a bi-layer dental ceramic restoration during its entire manufacturing process due to thermal expansion and elastic property mismatch. It is impossible to achieve a free of residual stresses bi-layer zirconia-porcelain restoration. The idea is to take the advantage of residual stress in design in such a way to prevent the crack initiation and progression. The hypothesis is a compressive residual stress at external contact surface would be enabling the restoration to endure a greater tensile stress. Optimizing the layers thickness, manufacturing process, and validating 3D simulations require development of new techniques of thickness, residual stresses and phase transformation measurement. In the present work, a combined mirco-tomography and finite element based method were adapted for thickness measurement. Two new 2D X-ray diffraction based techniques were adapted for phase transformation area mapping and combined phase transformation and residual stress measurement. Concerning the complex geometry of crown, an efficient method for X-ray diffraction data collection mapping on a given curved surface was developed. Finally a novel method for 3D dimensional x-ray diffraction data collection and visualization were introduced.

TABLE OF CONTENTS

LIST OF FIGURES

CHAPTER I

1.1 Background

Today dental restorations such as bridges and crowns are made of a combination of different ceramics in complex shapes. Traditionally, to avoid residual stresses, manufacturers have tried to match the thermal expansion coefficient of the typical base zirconia with a porcelain veneer. However, an in-situ confirmation that such a match was successful was never observed. Furthermore, residual stresses not only originate from thermal expiation mismatch, but they also develop as a function of the elastic modulus, Poisson ratio, grain-grain interactions, and other parameters related to processing such as the cooling rate of the dental restoration. Compressive residual stress at the surface of a ceramic or glass has been shown to prevent crack initiation and growth, improving damage resistance. The scope of this work is that residual stress not only on the surface plays a critical role, but the overall state of residual stress significantly governs failure and lifetime of ceramic dental restorations. With new insights, novel crowns could be designed with an understanding of residual stress. In addition, stabilized zirconia is meta-stable and transforms to monoclinic under critical stress situations. Our preliminary results show that zirconia undergoes transformation to relax residual stresses. This is another important factor in design, because this transformation under critical load retards

the failure. Knowledge on phase transformation coupled with residual stress states, layer thickness, and the manufacturing process opens up the keys to designing longer life dental restorations.

1.2 Problem statement

Catastrophic cracking limits the life time of modern crowns made of multilayer ceramics to a few years. Resistance to damage initiation would add years to the useful service life of dental restorative materials. The hypothesis is compressive residual stress, when applied at the surface of a crown, inhibits crack initiation and improves damage tolerance. The main gap to validate the hypothesis is the lack of well adapted laboratory experimental methods for residual stress measurement. Having a constraint of fixed final geometry, identifying the design parameters that could be changed to achieve a compressive residual stress at the crown surface, and a model to predict the residual stress are the next challenges. In addition, stabilized zirconia transforms to monoclinic under critical stress which couples with any residual stress.

1.3 Literature review

With favorable compressive strength, appealing esthetics, chemical inertness, and biocompatibility; ceramics have become widely used as dental restoration materials. With both esthetics and better mechanical properties expectancy continuing, layered structures of high compressive strength core polycrystalline yttrium stabilized zirconia with a porcelain veneer has become a dominant restoration material [1,2]. With a relatively high cost of replacement, and patient life expectancy continuing to increase, the

need for extended service life dental restoration continuous to grow. Recent research in this field is focused on more reliable crowns, since a restoration's service life is limited to a few years until catastrophic fatigue cracking [3,4]. The most common failure mode in the porcelain veneered zirconia system involves chipping and crack propagation in porcelain or along the interface at the porcelain side with little tendency to run through the zirconia core [5,6]. External applied load normally provides a motivation for zirconia tetragonal to monoclinic phase transformation [7,8]. Residual stress plays a critical role in failure of all materials including ceramics. The fabrication process of bi-layer ceramics requires a temperature change from sintering to room temperature. Typically, to avoid residual stresses, manufacturers have tried to match the thermal expansion coefficient of the typical base zirconia with a porcelain veneer [9,10]. However, an in-situ confirmation that such a match was successful was never observed. Residual stresses created as a result of thermal expansion coefficient mismatch may be sufficiently large to influence failure. FEA models predict high stress concentration in dental restoration due to residual stress caused by coefficient of thermal expansion mismatch during manufacturing and by applied loading [11]. Recently, Bale et al [12] performed measurements on the zirconia core of crown systems using Synchrotron X-ray diffraction and found that the magnitude of residual stress in zirconia can be as large as 1 GPa locally after veneering with porcelain, and the magnitude and sign of residual stress can change also. But the magnitude and distribution of residual stress in porcelain has never been measured. Furthermore developing a method that relies on Laboratory X-rays or other more easily accessible systems rather than Synchrotron radiation is a needed. Y.

Zhang et al explored the possibility of measuring the residual stress of both zirconia and porcelain by nanoindentation [13]. Up to now, there have been no studies using 3D FEA to determine the effect of stress induced phase transformation in zirconia on stress distributions. Importing the phase transformation mechanism in models has not been limited by complexity, but there is no proposed method to fairly validate the predicted results. This present study implements an advanced procedure using micro X-ray diffraction with a 2D area detector and precise positioning stage to map the phase transformation over the large complex cross-sectional area of a fractured crown. Although it has been proposed that, zirconia undergoes transformation to relax residual stresses [14], there is a lake of knowledge on well quantified phase transformation coupled with residual stress states. In the case of a dental crown, the bi-layer is not thin compared with the curvature radius of the surface, but the state of residual stress can be estimated from the local thickness of zriconia and porcelain layers. Residual stress in bi-layers depends on relative thickness of the layers [15]. There are reports on residual stress distribution in a bi-layer [16], but they have not studied the effect of changing the relative thickness in their model. Micro-Computed Tomography data, collected by H.A Bale et al [17] contains the required information for thickness measurements. Overall, reviewing the literature revels that, knowledge on phase transformation coupled with residual stress states, layer thickness, and the manufacturing process opens up the keys to designing longer life dental restorations.

1.4 Specific objectives

The following are my specific objectives to achieve for the ultimate goal of designing long life dental restorations.

1.4.1 Test and implement a suitable laboratory residual stress measurement method

The magnitude and distribution of residual stress in the crown system are largely unknown. Determining the residual stress quantitatively is challenging since the crown has such complex contours and shapes [18]. The approach for this aim is based on measuring residual stress on the zirconia side and potentially validating the result with other residual stress measurements [19].

1.4.2 Map contact induced phase transformation of a dental ceramic

Chipping failures observed clinically in bi layer systems of porcelain and zirconia restorations should be coupled with a monoclinic to tetragonal phase transformation in the zirconia layer due to the high stresses. This study implements an experimental method to map the phase transformation, after applying local compressive load until fracture, mimicking the clinically observed chipping failure [20].

1.4.3 Investigate a combined residual stress and phase transformation measurement

Predicting the residual stress plays a key role in designing bi-layer ceramic crowns. Residual stress can be relaxed by phase transformation as the monoclinic crystal has a

larger volume than tetragonal. The objective is to measure both stress and phase transformation on a failure sample. This could determine the stress threshold required for phase transformation to happen.

1.4.4 Develop a New method for X-ray diffraction mapping on curved surfaces

In case of dental crown, a part of surface may block the X-ray beam before reaching the desired point or diffracted rays might be blocked partially or completely before reaching the detector. Considering a complex geometry of a crown an efficient method for X-ray diffraction data collection mapping on a given curved surface is required to be developed. The idea is to use a video-laser auto z alignment system to collect the map of heights on a fine mesh grid. Having the height of the exposure points, surface geometry and surface normals on the 3D surface fit are accessible. An algorithm is essential to calculate the required rotation and tilt angles to coincide the sample normal with the diffraction center before each exposure. Collected diffraction frames results in phase transformation map.

1.4.5 Demonstrate porcelain layer thickness measurement method using X-ray micro tomography

The aim is to utilize tomography data to reconstruct the 3D structure of the crown followed by finite element surface meshing to calculate the minimum distance between nodes on surfaces. Thickness measured using this method can be coupled by bi-material bending equations to approximate the state of residual stress at different locations of the crown.

1.4.6 Model residual across the porcelain layer thicknesses

Developing an analytical and finite element model that predicts the residual stress for complex crown design, especially at the veneer interface is the goal of this section.

1.4.7 Provide a recommendation for porcelain thickness in modern crown design

Understanding the residual stress state and phase transformation in a crown and implementing controlled stresses for a new generation of crowns provides a tool for producing high performance, reliable dental restorations. The objective is to find key roles like lower limit for porcelain veneer thickness.

CHAPTER II

2 Micro x-ray tomography and non uniform thickness measurement

The fabrication process of bi-layer ceramics requires a temperature change from sintering to room temperature. Residual stresses created as a result of thermal expansion coefficient mismatch may be sufficiently large to influence failure. Theoretical models predict residual stress as a function layer thickness. The scale, and to some extent the geometry, changes during the firing process. In the case of complex geometries like dental crowns, micro-X-ray tomography is a unique non-destructive technique for layer thickness measurement. A method of developing a finite mesh model of real components involving complex geometries has been developed through the use of X-ray micro-tomography. This method computes the minimum distance between two triangulated surfaces constructed from tomography data. For each vertex of one surface, it computes the closest point on the other surface. The veneer layer thickness distribution was combined with residual stress curves advancing our understanding of the lower limit threshold of thickness in dental restoration design. An important observation is the

significant range in predicted residual stress in the veneer top surface from a tensile stress of 80 MPa to a compressive stress of -70 MPa as the thickness increased to 0.5 mm.

2.1 Introduction

A wide range of industrially important materials, from aircraft engine parts to dental crown ceramics, are made of bi-layer or multi layer structures. The application of layered ceramics or metal ceramic components is challenged by thermal expansion coefficient mismatch that creates curvature effects and residual stress [21,22]. Timoshenko fist derived a general solution for bi-layer bending due to residual stresses [23]. Considerable efforts [24,25,26] have been devoted to analyzing residual stresses for multilayer systems because of their wide application as microelectronic, optical, and structural components. Residual stress in the interface of a bi-layered material is a function of layer thickness [26,27]. In the case of a dental crown, the bi-layer is not thin compared with the curvature radius of the surface, but the state of residual stress can be estimated from the local thickness of zriconia and porcelain layers. Here we focus on ceramic dental crowns. The base layer almost has a constant thickness, typically around 0.5 mm, and the thickness of porcelain is varied to create the aesthetic and functional geometry of the crown. Micro X-ray tomography slides have been used to reconstruct the geometry of crowns for finite element analysis [12,28,40]. Allahkrami et al used sequence of microscopy images for 3d reconstruction of a fiber model [29,30]. Here we will explain a method that utilizes tomography data to reconstruct the 3D structure of the crown followed by finite element surface meshing to calculate the minimum distance between nodes on surfaces. Thickness measured using this method can be coupled by bi-material

bending equations to approximate the state of residual stress at different locations of the crown.

2.2 Micro-X-ray tomography and non uniform thickness

Micro-Computed Tomography data, collected by H.A Bale and J.C Hanan [12], was used for 3D reconstruction of a bi layered zirconia porcelain. The following discusses a method used to calculate the local thickness of the porcelain layer. There are two surface functions, for zirconia $f_z(x,y)$ and for porcelain $f_p(x,y)$, obtainable from X-ray tomography, as illustrated in Figure 1.

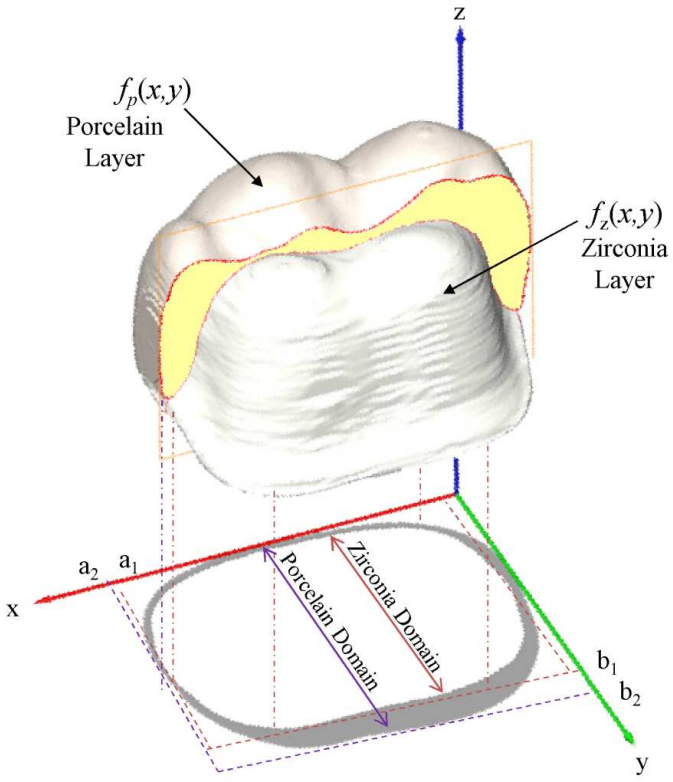

Figure 1 Graphical rendering of tomography from a bi-layer dental crown made of ceramic base covered by porcelain.

Because $f_z(x,y)$ and $f_p(x,y)$ are two locally variant curved functions, the distance between them is not well defied. It is possible to calculate the shortest surface-to-surface distance for the grid points laying on one of the surfaces. Here we are interested to measure the shortest distance between each point on $f_z(x,y)$, the base surface, relative to the outside of the porcelain layer, $f_p(x,y)$ surface. Therefore, the zirconia upper surface is considered a reference surface, and the minimum distance to the porcelain surface at each point is desired. If coordinates are selected as shown in Figure 1, , we are dealing with two real valued functions $f_z(x,y)$ and $f_p(x,y)$ that satisfy $f_z(x,y) \leq f_p(x,y)$ for all point on the domain of $f_z(x,y)$. This is a z-simple geometry because the region is described in a simple way, using z as a function of x and y. This means, for each pair of "x, y" there is one unique corresponding "z" value.

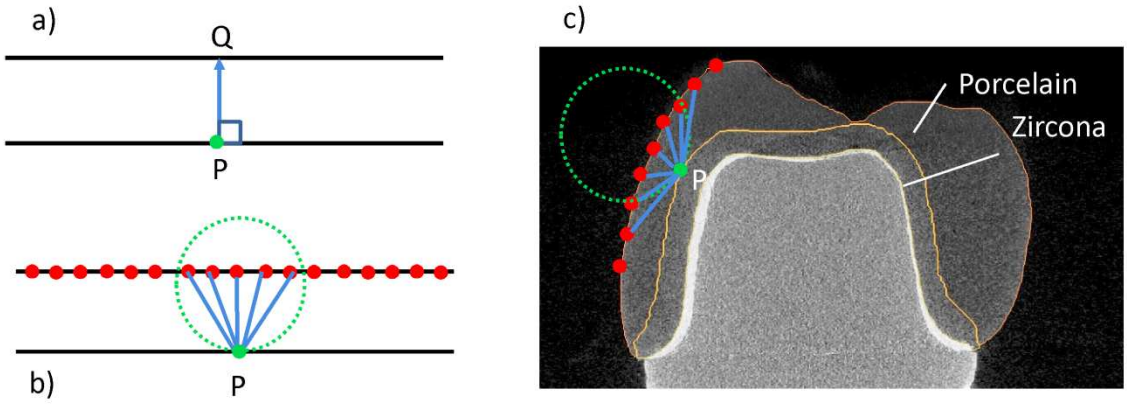

Figure 2 a) Distance between two straight lines b) Minimum distance between the nodes on two straight lines c) Minimum distance between two curved lines.

Figure 2a shows that distance between two parallel lines at s certain point P can be defined as the length of the normal vector that originates at point P and ends at point Q.

Instead, if we grid the top line with very fine steps, the minimum distance between the nodes and point P in Figure 2b is the same as distance PQ in Figure 2a. The same analogy is extendable for the distance between two 3D curved surfaces at a certain point on one of the surfaces, as illustrated in Figure 2c.

2.2.1 Converting tomography to key information

Three dimensional data visualization and finite element triangular surface meshing was carried out in Amira 3.1.1. A customized Matlab code (Appendix 1) was developed to extract the nodes that belong to $f_z(x, y)$ and $f_p(x, y)$.

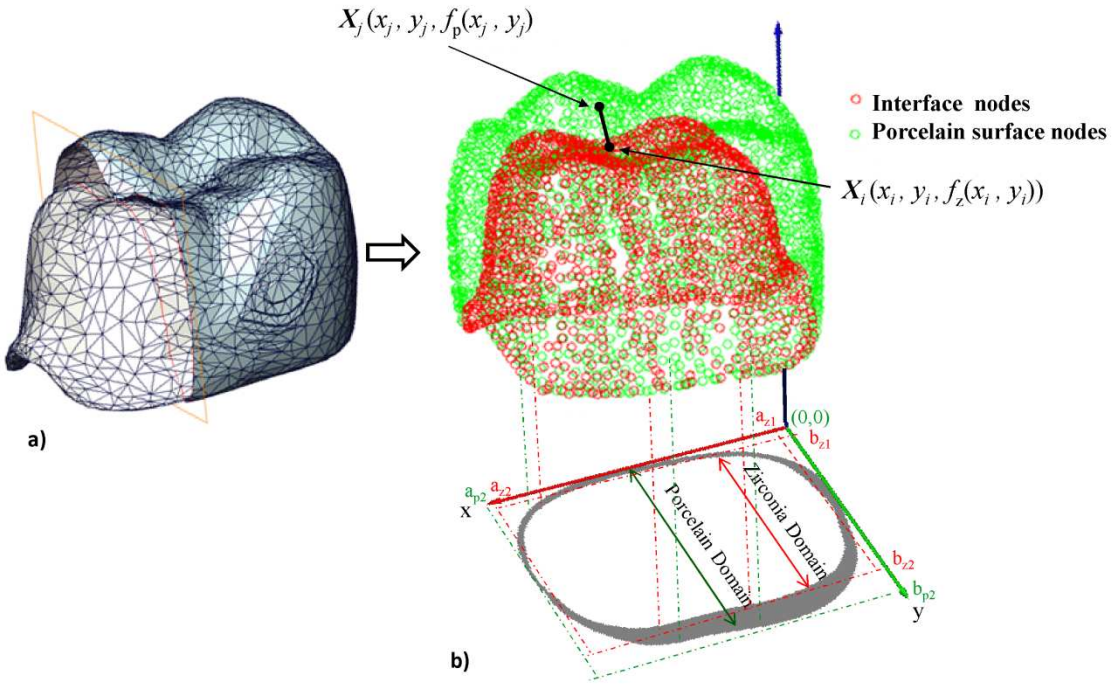

Figure 3 a) Triangular surface meshing of tomographed crown b) Extracted surface nodes

For a better visualization, nodes for the upper surface of the porcelain layer are colored green in Figure 2, and nodes for the interface surface of zirconia and porcelain are determined with a red color (this appears darker in black and white).

2.2.2 Layer thickness distribution

The minimum distance for a point i on the interface surface that has a coordinate of $X_i = (x_i, y_i, f_z(x_i, y_i))$ on the domain $[a_{z1}, b_{z1}] \leq [x_i, y_i] \leq [a_{z2}, b_{z2}]$ is defined as,

$$d(x_i, y_i, z_i) = \min\{\sqrt{(x_i - x_j)^2 + (y_i - y_j)^2 + (f_z(x_i, y_i) - f_p(x_j, y_j))^2}\ ; \text{for all possible j}\} \quad \textbf{2-1}$$

Where j is the index for a point j on the interface surface (zirconia surface) that has a coordinate of $\boldsymbol{X}_j = (x_j, y_j, f_p(x_j, y_j))$ on the domain of $[0,0] \leq [x_j, y_j] \leq [a_{p2}, b_{p2}]$. The distance $d(x_i, y_i, z_i)$ is always positive real number and is equal to zero at intersecting points or overlapped regions. A histogram of the distance measurement is illustrated in Figure 4.

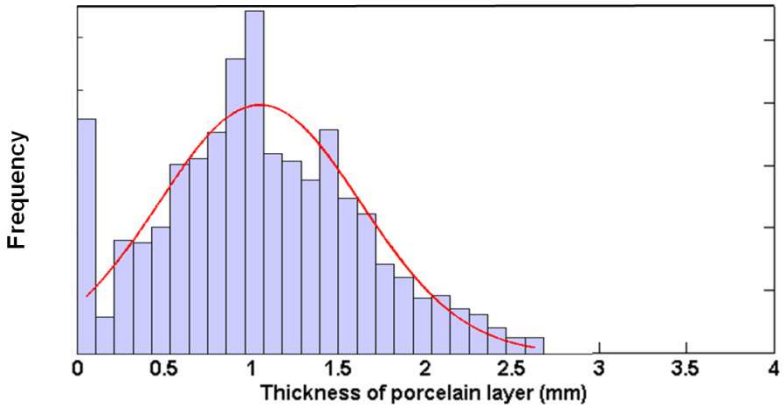

Figure 4 Histogram of minimum distance measurement.

Because the density of nodes in a certain area is a function of surface fluctuation, nodes are randomly distributed on the interface and veneered surface. The region with more surface fluctuation has more density of nodes in comparison with flat regions. This has not affected the accuracy of the minimum distance measurement for a particular node but introduces an error in the histogram of distance distribution, because we are not sampling the domain with equal probability. In addition to histogram of porcelain thickness, using a Matlab code (Appendix 2) a colored 3D map of minimum distance measurement was created. Different rendering views of the results are shown in Figure 5. Each triangle face has three nodes. The average of minimum distance for those three nodes was considered as the face minimum distance. Faces are colored based on their average minimum distance.

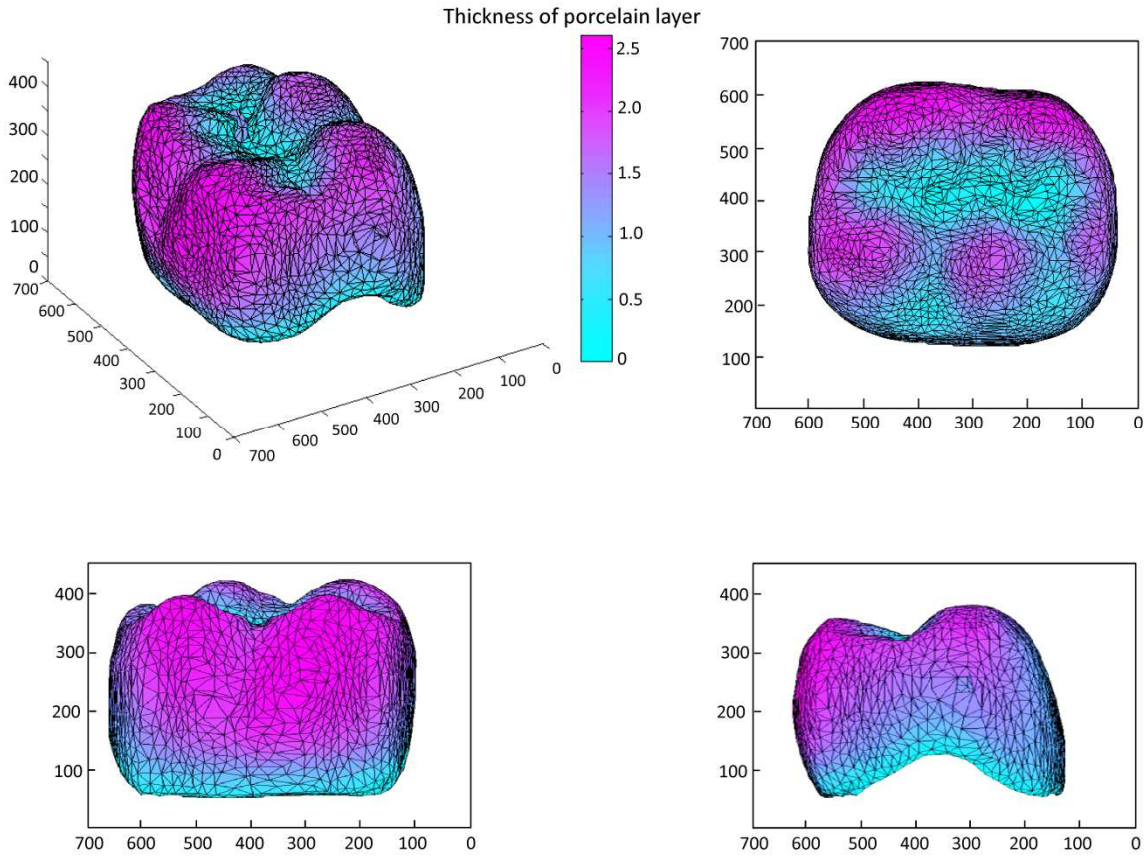

Figure 5 Colored map of minimum distance measurement.

2.2.3 Redistribution of nodes using 3D interpolation

Accuracy of the thickness distribution depends on number of the nodes and how fairly they are distributed on the surface. More number of nodes increases the computation time. Calculation time is reducible by applying a constraint on the searching area to a ball with radius of appropriate r_0 instead of global searching for minimum distance. Increasing the number of nodes does not guarantee equal density of nodes on the surface, because sharp edges and regions faced toward the z direction will have more contribution to the distribution. A simple solution to this is to weight the distribution by node density.

Figure 6a illustrates a 3D interpolation between the interface nodes implemented to create a regular mesh, which provides an easy access to the nodes coordinates through *i* and *j* indexes for programming loops. New set of nodes, selected as the edges of the grid that covers up the surface is illustrated in Figure 6b. Using the same method new sets of nodes can be created for the porcelain surface as well. These two new sets of nodes are distributed with equal density on their projection to the x-y plane. Comparing Figure 6c and Figure 6d, nodes located on the walls of the crown cover more surface area than the nodes on the top.

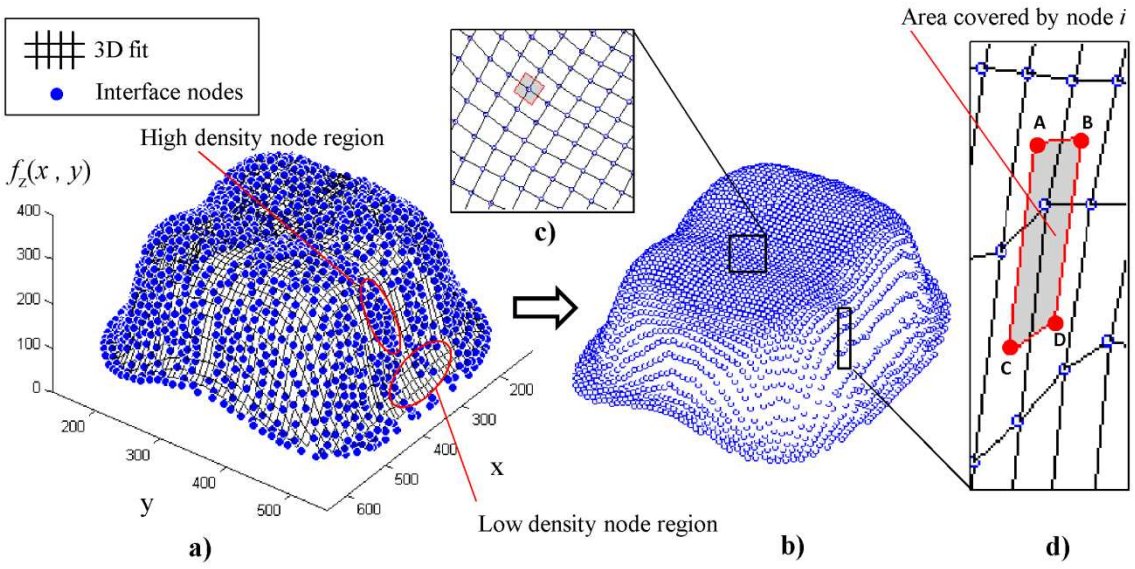

Figure 6 a) randomly distributed nodes (blue markers) with a 3D interpolated surface (black lines). b) Generated regular nodes with an illustration of the area covered by nodes in a relatively flat and a sloped region c) Zoom on high density node region d) Zoom on low density node region.

If we multiply the minimum distance calculated for each node by a unitless weight, corresponding to the area that the node covers, the resulting histogram of the weighted

distance distribution is corrected from the prior node distribution error. Decomposing the surface between the nodes is simply an implementation of Voronoi tessellation decomposition of the surface with the seeds located at the nodes.

These required coordinates labeled with A, B, C and D in Figure 6d, were computed using 3D interpolation. The surface area corresponding to a node located in a point $\boldsymbol{X}_i = (x_i, y_i, f_z(x_i, y_i))$ can be approximated by the average of four cross product absolute values, if given the coordinate of the tetragon vertices that engulfs the node.

$$S(x_i, y_i, f_z(x_i, y_i)) = \frac{1}{4}(\left|\overrightarrow{AB} \times \overrightarrow{AC}\right| + \left|\overrightarrow{AB} \times \overrightarrow{DB}\right| + \left|\overrightarrow{BD} \times \overrightarrow{DC}\right| + \left|\overrightarrow{AC} \times \overrightarrow{CD}\right|) \quad \textbf{2-2}$$

The shortest surface-to-surface distance along the interface surfaces, and the area belonging to the node $S(x_i, y_i, f_z(x_i, y_i))$, was calculated for each node using a Matlab code.

The profile of a calculated Voronoi cell area for nodes along the cross section is illustrated in Figure 7. There are two peaks at both sides of the profile corresponding to the wall area of crown which has more slope and less density of nodes. The flat region between two sharp peaks is related to the top surface of the crown which has greater areal density of nodes.

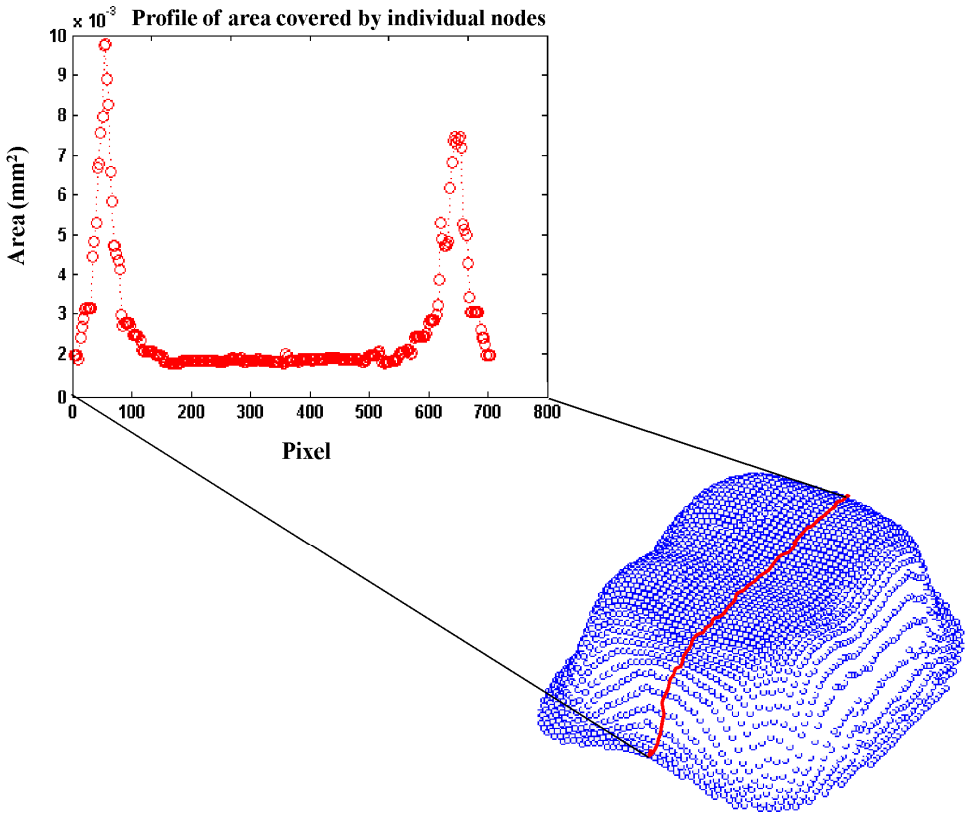

Figure 7 Profile shows the area corresponding to the nodes.

In order to better visualize the effect of the nodes distribution density on thickness calculations and requirement of correction, a contour plot of the area belonging to the individual nodes is shown in Figure 8a. Figure 8b is the histogram corresponding to the contour plot. It can be seen, most of the areas belonging to the top portion of the crown have the same range, but values are much higher for the walls, which confirm the importance of the node distribution correction.

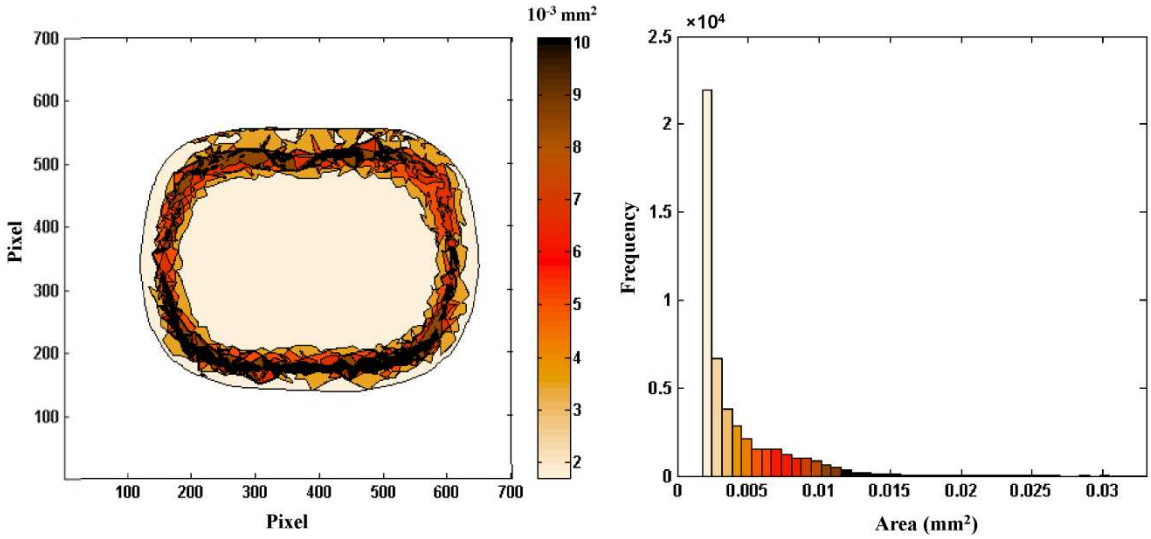

Figure 8 a) Contour plot (top view) and b) histogram of area covered by nodes

2.2.4 Corrected thickness distribution using probability density function

For weighted by area nodes, we cannot simply plot the histogram, but it is possible to calculate the Probability Density Function (PDF), which here is a function that describes the relative likelihood for the thickness of a layer, as a variable, to occur at a given point in the observation space.

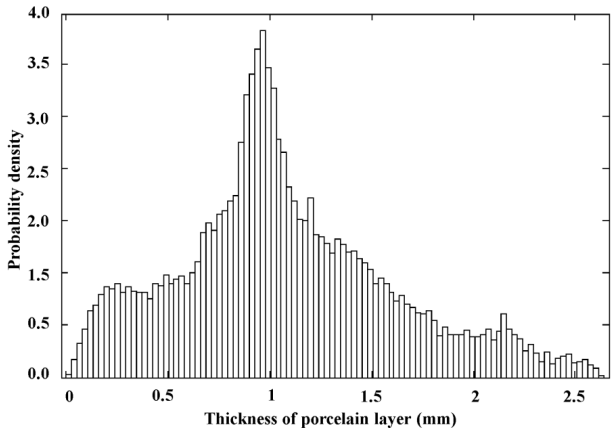

Figure 9 Probability Density Function (PDF) for thickness of porcelain layer in typical porcelain covered zironia base dental crown.

The PDF of minimum distance weighted by node area is shown in Figure 9. This PDF thickness distribution is independent of node density distribution. A histogram of minimum distance measurement (Figure 4) was corrected using PDF information as represented in Figure 10.

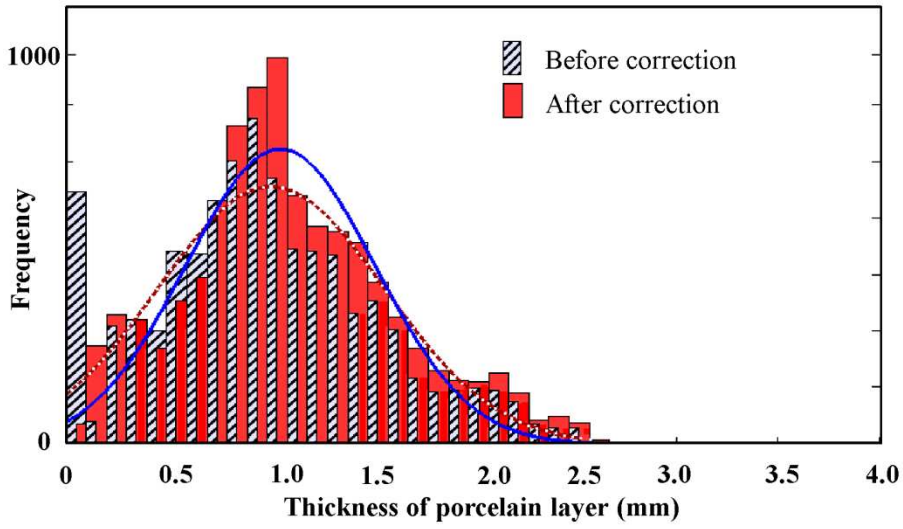

Figure 10 Histogram of minimum distance measurement before and after correction.

Comparing histograms of thickness distribution before and after correction reveals a considerable change at thin thickness region (less than 0.2 mm). Errors in distribution are introduced mostly in thin regions (less than 0.2 mm), because locations with thin porcelain layer thickness have more complexity in geometry variation. In general, meshing software dedicates more nodes to maintain the geometry variations in complex geometry regions which later caused the error in thickness distribution. Using the described technique the correct thickness distribution was measured.

2.3 Analytical model for residual stress prediction in a bi-layer

This analytical model used equations that couple the strain at any point of the ceramic or porcelain to the curvature and displacement of a geometric mid-plane of the two coupled plates. Figure 11 illustrates a cross section of bi-material plates before the residual stresses were in effect and after the resulting deformation due to bending [31].

It was assumed initially that line ABCD is straight and perpendicular to the mid plane and remains straight and perpendicular to mid plane after deformation. Displacements of point B after deformation in directions x, y, and z will be u_0, v_0 , and w_0 respectively. The slope of the bi-material mid plane in the x direction is:

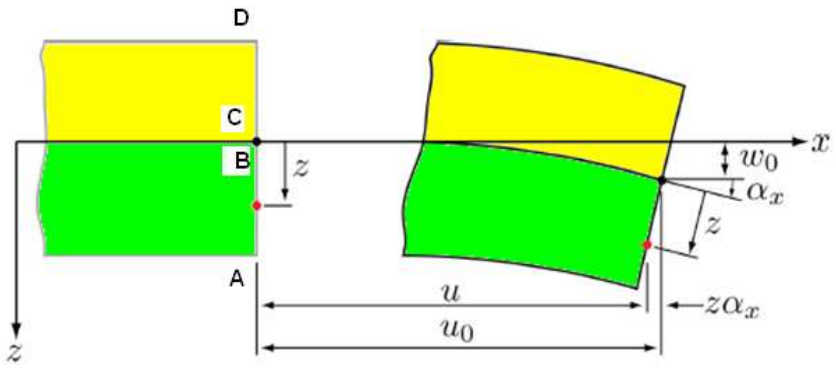

Figure 11 Cross section of bi-material plates before bending and after deformation due to bending [31].

$$\alpha = \frac{\partial w_0}{\partial x} \qquad \textbf{2-3}$$

Where u is displacement in the x direction of a point C located on line ABCD at distance z from the mid-plane which is given by,

$$= u_0 - z\alpha \qquad \textbf{2-4}$$

Combining equation 2-3 and 2-4 we obtain,

$$u = u_0 - z\frac{\partial w_0}{\partial x};\ \ v = v_0 - z\frac{\partial w_0}{\partial y} \qquad \textbf{2-5}$$

Equation 2-5 relates displacement u in the x direction of an arbitrary point to the distance z from the mid-plane. Similarly for the y direction it relates displacement v to the distance z from the geometrical mid plane. Using the definition of strain and neglecting normal strain, ε_z,

$$\begin{Bmatrix} \varepsilon_x \\ \varepsilon_y \\ \gamma_{xy} \end{Bmatrix} = \begin{Bmatrix} \varepsilon_x^0 \\ \varepsilon_y^0 \\ \gamma_{xy}^0 \end{Bmatrix} + z\begin{Bmatrix} k_x \\ k_y \\ k_{xy} \end{Bmatrix} \qquad \textbf{2-6}$$

Where, ε_x^0, ε_y^0 and γ_{xy}^0 are the first derivatives of the displacements *u* and *v*; k_x, k_y, and k_{xy} are the second derivatives of *u* and *v*. Equation 2-6 shows a linear relation between strains and thickness variation in bi-materials. For two dimensional cases, all the terms related to the *z*-axis may be dropped to simplify the stress-strain relation to,

$$\begin{Bmatrix}\sigma_x\\ \sigma_y\\ \tau_{xy}\end{Bmatrix}=\begin{bmatrix}\overline{Q}_{11} & \overline{Q}_{12} & \overline{Q}_{16}\\ \overline{Q}_{12} & \overline{Q}_{22} & \overline{Q}_{26}\\ \overline{Q}_{16} & \overline{Q}_{26} & \overline{Q}_{66}\end{bmatrix}\begin{Bmatrix}\epsilon_x\\ \varepsilon_y\\ \gamma_{xy}\end{Bmatrix} \qquad \textbf{2-7}$$

Stiffness matrixes for zirconia and porcelain layers are [32],

$$\begin{bmatrix}Q_{11} & Q_{12} & 0\\ Q_{12} & Q_{22} & 0\\ 0 & 0 & Q_{66}\end{bmatrix}_{\text{zirconia}}=\begin{bmatrix}215.43 & 47.34 & 0\\ 47.34 & 215.43 & 0\\ 0 & 0 & 84.02\end{bmatrix}\text{(GPa)}$$

$$\begin{bmatrix}Q_{11} & Q_{12} & 0\\ Q_{12} & Q_{22} & 0\\ 0 & 0 & Q_{66}\end{bmatrix}_{\text{porcelain}}=\begin{bmatrix}73.56 & 16.18 & 0\\ 16.18 & 73.56 & 0\\ 0 & 0 & 23.69\end{bmatrix}\text{GPa)} \qquad \textbf{2-8}$$

Mechanical strains denoted by ε^M while $\varepsilon_x^T, \varepsilon_y^T$ and γ_{xy}^T are thermal strain.

$$\begin{Bmatrix}\varepsilon_x^M\\ \varepsilon_y^M\\ \gamma_{xy}^M\end{Bmatrix}=\begin{Bmatrix}\varepsilon_x\\ \varepsilon_y\\ \gamma_{xy}\end{Bmatrix}-\begin{Bmatrix}\varepsilon_x^T\\ \varepsilon_y^T\\ \gamma_{xy}^T\end{Bmatrix}=\begin{Bmatrix}\varepsilon_x^0\\ \varepsilon_y^0\\ \gamma_{xy}^0\end{Bmatrix}+z\begin{Bmatrix}k_x\\ k_y\\ k_{xy}\end{Bmatrix}-\begin{Bmatrix}\alpha_x\Delta T\\ \alpha_y\Delta T\\ \alpha_{xy}\Delta T\end{Bmatrix} \qquad \textbf{2-9}$$

The coefficients of thermal expansion, are denoted by α_{x} and α_{y}. Equation 2-7 is the reduced form of the following general matrix, where A, B and D, are the stiffness matrices, coupling stiffness matrix, and bending stiffness matrix, respectively.

$$\begin{Bmatrix}\sigma_x^T\\ \sigma_y^T\\ \tau_{xy}^T\end{Bmatrix}=\begin{bmatrix}\bar{Q}_{11} & \bar{Q}_{12} & \bar{Q}_{16}\\ \bar{Q}_{12} & \bar{Q}_{22} & \bar{Q}_{26}\\ \bar{Q}_{16} & \bar{Q}_{26} & \bar{Q}_{66}\end{bmatrix}\begin{Bmatrix}\varepsilon_x^0 z + k_x - \alpha_x \Delta T\\ \varepsilon_y^0 z + k_y - \alpha_y \Delta T\\ \gamma_{xy}^0 z + k_{xy} - \alpha_{xy} \Delta T\end{Bmatrix} \quad \textbf{2-15}$$

$$\begin{Bmatrix}N\\ M\end{Bmatrix} = \begin{bmatrix}A & B\\ B & D\end{bmatrix}\begin{Bmatrix}\epsilon^0\\ k\end{Bmatrix} \quad \textbf{2-10}$$

Residual stresses originate within the composite upon firing the porcelain layer on the zirconia at a temperature of 1200 K and cooling to room temperature (298 K). The calculation may be carried out in the following sequence: $\Delta T = 298 - 1200 = -902$

$$\begin{Bmatrix}N_x^T\\ N_y^T\\ N_{xy}^T\end{Bmatrix} = \begin{Bmatrix}-1.7524\\ -1.7524\\ 0\end{Bmatrix} \text{ (GPa·mm); } \begin{Bmatrix}M_x^T\\ M_y^T\\ M_{xy}^T\end{Bmatrix} = \begin{Bmatrix}-0.2301\\ -0.2301\\ 0\end{Bmatrix} \text{ (GPa·mm}^2\text{)} \quad \textbf{2-11}$$

Using the inverted form of Equation 2-10,

$$\begin{Bmatrix}\epsilon^0\\ k\end{Bmatrix} = \begin{bmatrix}A' & B'\\ B' & D'\end{bmatrix}\begin{Bmatrix}N^T\\ M^T\end{Bmatrix} \quad \textbf{2-12}$$

Using Equation 2-12, the matrix mid-plane strains and plate curvatures were evaluated.

$$\begin{Bmatrix}\varepsilon_x^M\\ \varepsilon_{xy}^M\\ \gamma_{xy}^M\end{Bmatrix}_{\text{zirconia}} = \begin{Bmatrix}0.37 - 1.3z\\ 0.37 - 1.3z\\ 0\end{Bmatrix} \times 10^{-3} \text{ and } \begin{Bmatrix}\varepsilon_x^M\\ \varepsilon_{xy}^M\\ \gamma_{xy}^M\end{Bmatrix}_{\text{porcelain}} = \begin{Bmatrix}-0.53 - 1.3z\\ -0.53 - 1.3z\\ 0\end{Bmatrix} \times 10^{-3} \quad \textbf{2-14}$$

$$\begin{Bmatrix}\varepsilon_x^0\\ \varepsilon_{xy}^0\\ \gamma_{xy}^0\end{Bmatrix} = \begin{Bmatrix}-9.8\\ -9.8\\ 0\end{Bmatrix} \times 10^{-3} \text{ and } \begin{Bmatrix}k_x\\ k_y\\ k_{xy}\end{Bmatrix} = \begin{Bmatrix}-1.3\\ -1.3\\ 0\end{Bmatrix} \times 10^{-3} \quad \textbf{2-13}$$

Mechanical strains that cause the residual stresses are calculated in accordance with equation 2-9

Residual stress distribution was obtained by substituting the strains in the equation 2-7

The stress profile is assumed linear across the thickness of a layer. Stresses at a surface layer and interface between two layers were calculated as follows,

Zirconia layer z = 0.5 mm

$$\begin{Bmatrix} \varepsilon_x^M \\ \varepsilon_{xy}^M \\ \gamma_{xy}^M \end{Bmatrix}_{z=+0.5} = \begin{Bmatrix} -2.8 \\ -2.8 \\ 0 \end{Bmatrix} \times 10^{-4} \text{ and } \quad \begin{Bmatrix} \sigma_x^T \\ \sigma_y^T \\ \tau_{xy}^T \end{Bmatrix} = \begin{Bmatrix} -73.5 \\ -73.5 \\ 0 \end{Bmatrix} \text{ (MPa)} \qquad \textbf{2-16}$$

Zirconia layer z = 0 mm

$$\begin{Bmatrix} \varepsilon_x^M \\ \varepsilon_{xy}^M \\ \gamma_{xy}^M \end{Bmatrix}_{z=0} = \begin{Bmatrix} 3.7 \\ 3.7 \\ 0 \end{Bmatrix} \times 10^{-4} \text{ and } \quad \begin{Bmatrix} \sigma_x^T \\ \sigma_y^T \\ \tau_{xy}^T \end{Bmatrix} = \begin{Bmatrix} 97.2 \\ 97.2 \\ 0 \end{Bmatrix} \text{ (MPa)} \qquad \textbf{2-17}$$

Porcelain layer z = 0 mm

$$\begin{Bmatrix} \varepsilon_x^M \\ \varepsilon_{xy}^M \\ \gamma_{xy}^M \end{Bmatrix}_{\text{porcelain } z=0} = \begin{Bmatrix} 5.3 \\ 5.3 \\ 0 \end{Bmatrix} \times 10^{-4} \text{ and } \begin{Bmatrix} \sigma_x^T \\ \sigma_y^T \\ \tau_{xy}^T \end{Bmatrix} = \begin{Bmatrix} -47.6 \\ -47.6 \\ 0 \end{Bmatrix} \text{ (MPa)} \qquad \textbf{2-18}$$

Porcelain layer z = -0.5 mm

$$\begin{Bmatrix} \varepsilon_x^M \\ \varepsilon_{xy}^M \\ \gamma_{xy}^M \end{Bmatrix}_{\text{porcelain } z=-0.5} = \begin{Bmatrix} 11.8 \\ 11.8 \\ 0 \end{Bmatrix} \times 10^{-4} \text{ and } \begin{Bmatrix} \sigma_x^T \\ \sigma_y^T \\ \tau_{xy}^T \end{Bmatrix} = \begin{Bmatrix} 9.7 \\ 9.7 \\ 0 \end{Bmatrix} \text{ (MPa)} \qquad \textbf{2-19}$$

2.3.1 Application of the model for various porcelain thickness

For x-y reference axes, the variation of residual stresses across the ceramic layer thicknesses is shown in Figure 12. Residual stress has a self equilibrating nature, so the

net area in each plot and the moment of the area about any point are zero. The residual stresses were tensile on the zirconia side of the interface and compressive on the porcelain side.

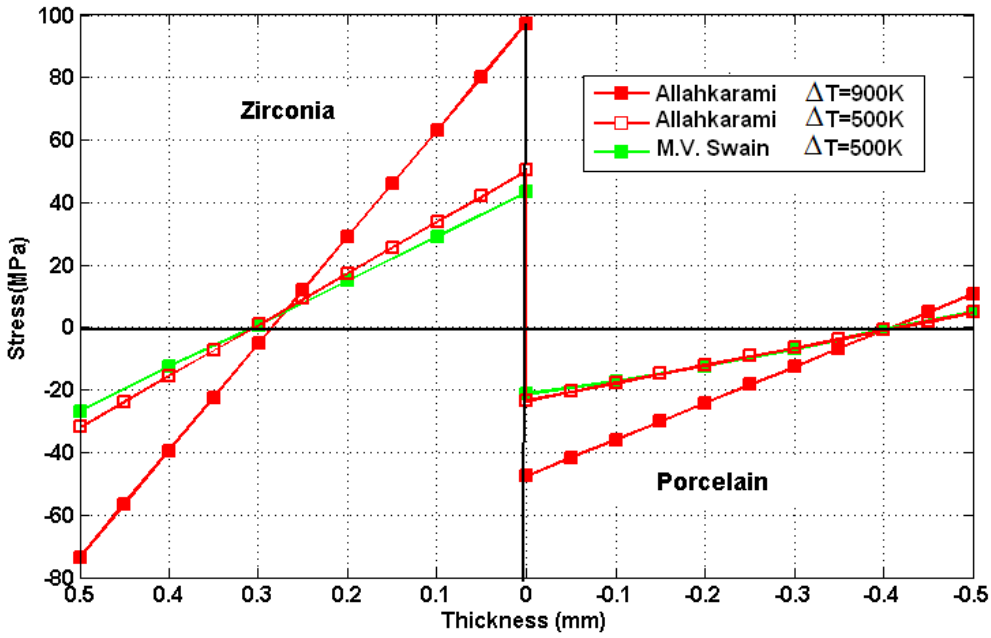

Figure 12 Residual stresses versus thickness of layers (M.V.Swain [38]).

The slope of the residual stress curves depends on the temperature gradient from the firing temperature to the room temperature. Figure 13 shows the predicted residual stress profile for different curing temperatures. Using this model, it is possible to predict the effect of porcelain layer thickness (for fixed zirconia layer at 0.5 mm) on residual stress in particular positions of interest as shown in Figure 4 for bottom of the zirconia layer, interface of the zirconia side, interface of the porcelain side, and top surface of the porcelain. An important observation to note, is the significant step in residual stress from a tensile stress of 80 MPa to a compressive stress of -70 MPa as the thickness of

porcelain layer was increased to 0.5 mm. Furthermore, a gradual increase in residual stress was observed from -70 MPa to -20 MPa as the thickness was further increased to 4mm.

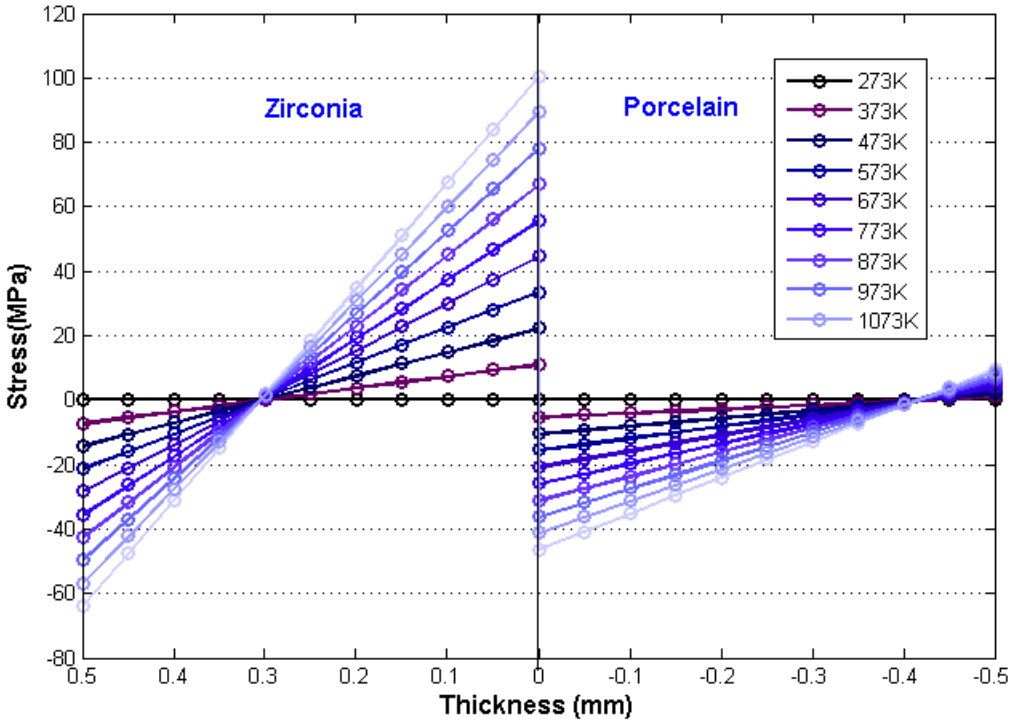

Figure 13 Predicted residual stress profile for different curing temperatures.

2.4 Combined residual stress prediction and thickness distribution

Using the model described in this chapter published earlier [27], it is possible to predict the effect of the porcelain layer thickness (here for a fixed zirconia layer at 0.5 mm) on residual stress in particular positions of interest for the bottom of the zirconia layer, interface of the zirconia side, interface of the porcelain side, and top surface of the porcelain; as shown in Figure 14. (Appendix 4)

Figure 14 suggests that most of the drastic changes in residual stress occur within 0.5 mm of the porcelain thickness. The case of a constant zirconia thickness with varying porcelain thickness is of greater importance due to its relevance to the dental restoration geometries.

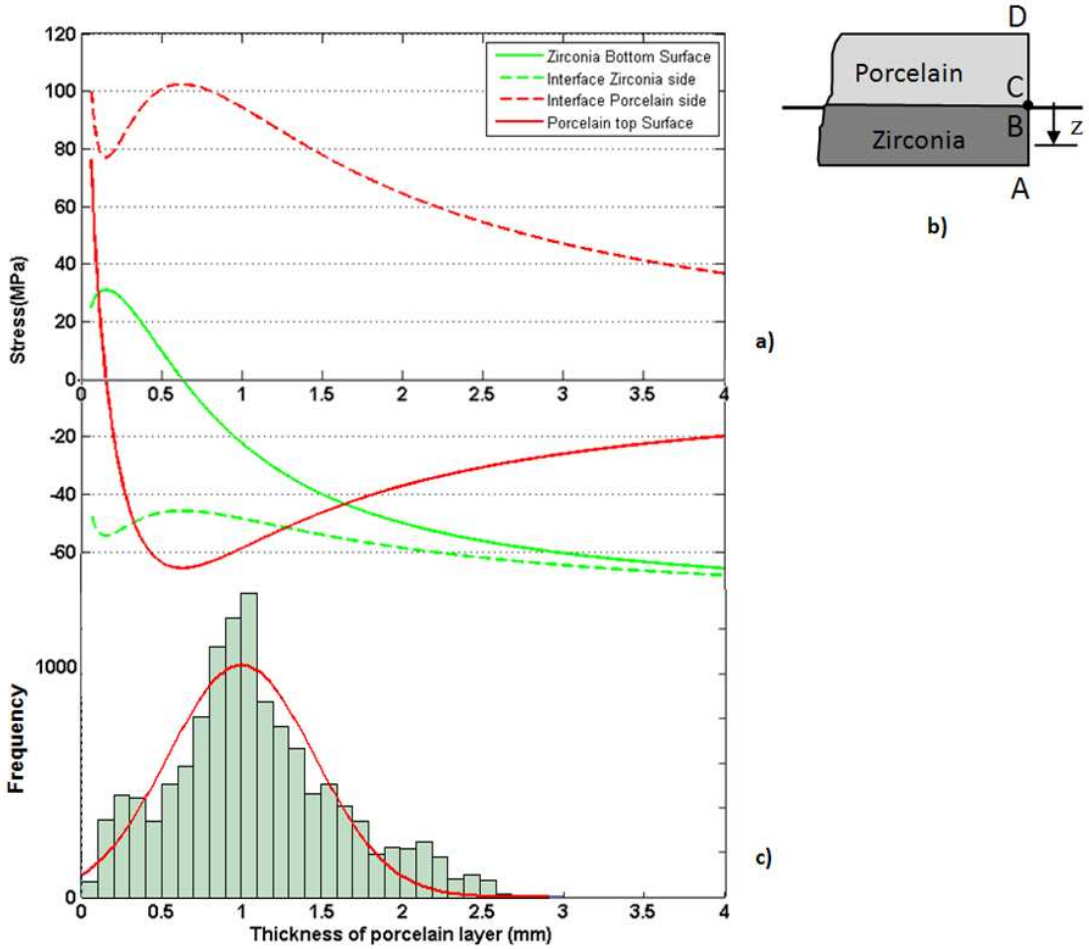

Figure 14 a) Residual stresses in the interface and top and bottom surface as a function of porcelain thickness. b) The locations A, B, C, and D with respect to the bi-layer geometry and 'z' indicates the thickness of zirconia and porcelain. c) Histogram of minimum distance measurement after correction.

The current model considers a perfect joint between the layers. In an improved model the strength of the layers bonding could be introduced to the model. This requires measurement of bounding strength of the two layers. Similar method that has been implemented in the reference [33] could be used for selecting the best bounding material for porcelain-zirconia system.

2.5 Conclusion

The residual stresses between two disks of zirconia and porcelain fired together at high temperature and cooled down to room temperature were predicted. The residual stress was tensile in the zirconia side of the interface and compressive in the porcelain side. The magnitude of the residual stress depends on initial and final temperature as well as the thickness of the porcelain and zirconia layers.

Based on the fundamental equations for strain, an analytical model for a bi-layer ceramic composite was developed. The bilayer model consisting of a 0.5 mm yttria stabilized tetragonal zirconia disk veneered with a 0.5 mm thick porcelain had a predicted residual stress (σ_x) of -60 MPa, 100 MPa, -40 MPa, and 10 MPa for the bottom of the zirconia layer, the zirconia at the interface, the porcelain at the interface, and the top surface of the porcelain respectively. Using a set of generalized equations for thickness, the model simulated results of residual stress with change in thickness. A method of generating surface meshing for finite elements using micro X- tomography of dental crowns was utilized to extract node coordinates on the surface of real crown geometry. The result of this method was used to calculate the thickness of the porcelain layer in a zirconia-

porcelain bi-layer ceramic crown. A histogram of the thickness distribution was combined with a beam bending model residual stress prediction for bi-layer ceramics keeping the thickness of the zirconia layer constant. Combining the model with the thickness measurement suggests development of crowns with controlled porcelain thickness in order to minimize residual stress. Over all, locations where the thickness of the porcelain relative to the zirconia layer is small (<0.2 mm) should be avoided. This is generally the case for the observed crown as only 3.3% of the porcelain was below this thickness. 53% was above 1 mm, which appears a safer thickness when considering the predicted residual stresses. It was found that for this typical molar crown, the thickness of the porcelain layer changed from 0.05 mm to 2.5 mm, and the most probable 43% thickness was around 1±0.2 mm. Predictions of the change in stresses with thickness are non-trivial and would prove valuable in validating experimentally determined values of residual stress. Validated results could lead to recommendations for reduced stress concentration and longer service life in dental restorations.

CHAPTER III

3 Tetragonal to Monoclinic Phase Transformation in Zirconia Dental Crowns

Chipping failures observed clinically in bi layer systems of porcelain and zirconia restorations should be coupled with a monoclinic to tetragonal phase transformation in the zirconia layer due to the high compressive stress. This study implements an experimental method to map the phase transformation, after applying local compressive load until fracture. Such fractures resemble clinically observed chipping failure. More than a thousand 2D micro X-ray diffraction frames collected on the flat surface of a sectioned fractured crown were analyzed to map phase transformations. Yttria-zirconia tetragonal phase transformations to monoclinic zirconia and monoclinic yttria were observed, mostly at the impacted area. A simple map of (101) tetragonal d-spacing strain reveals stress relaxation during phase transformation. Relatively more phase transformation was detected at the inner section of the lingual side, because the initial state of compressive residual stress assists this phase transformation at the inner section of the lingual side of the core while initial tensile stress at the outer sides under the veneer relaxes under compression and initially prevents phase transformation. Phase transformation might occur during the cooling process [34,35], annealing process [36] or

by mechanical stress [37,38]. Here the phase transformation attributed to zirconia is mechanical stress driven.

3.1 Introduction

3.2 Materials and Methods

A standard polycrystalline yttria stabilized tetragonal zirconia ceramic crown core covered by porcelain veneer was subjected to a single load to failure. A 1.9 mm tungsten carbide ball indenter was used to apply load to failure using a customized frame. The chipped region due to failure at one of the cusps was sectioned in two halves using a low speed water cooled diamond saw and was mounted onto an aluminum plate with high strength epoxy glue as shown in Figure 15a. X-ray diffraction was performed with Cu-Kα radiation at tube parameters of 40kV/40mA using a Bruker D8 Discover XRD^2 micro-diffractometer equipped with the General Area Diffraction Detection System (GADDS) and Hi-Star 2D area detector. The detector distance to the center of diffraction was kept at 29.95 cm which covers approximately the area of 20° in 2θ and 20° in χ with 0.02° resolution. To map many spots, a motorized five axis (X, Y, Z (translation), χ (tilt), ϕ (rotation)) stage was used for positioning which can move the measurement spot to the instrument center within 12.5 µm position accuracy and 5 µm repeatability.

The mapping X-ray diffraction scans were performed on the flat surface of the crown zirconia layer using a 0.2 mm pinhole collimator in reflection mode. Although the use of a 200 µm pinhole collimator in comparison with an available 50 µm monocapillary beam decreases the intensity of the X-ray beam on the sample, it provides better crystallite

statistics in this case where the size of grains on average were 0.1 to 0.3 µm. This beam size can provide information from several grains in a single exposure eliminating the need for averaging several scans. Figure 15b demonstrates a graphical representation of the grid over which X-ray diffraction frames were collected. It illustrates how the total area was reduced to eight sub-grid regions named A, B … and H. In each sub region, an XRD map was collected just for area between the two surfaces and not outside locations. Using a sequential list, the system automatically brings each predetermined point to the diffractometer center and performs final height adjustments automatically in the out-of-plane direction with an auto video-laser positioning system before each exposure. In fact, diffraction frames were only collected on the zirconia surface, which is polycrystalline while the porcelain region was ignored because it is amorphous and excluded as "not diffracting" by a threshold on the number of detector counts.

Initial grid points at the region F and selected points for diffraction are shown in Figure 16a and b respectively. Frames on the overlapped area between regions F and G were collected twice to monitor reproducibility. This result reveals an acceptable repeatability within a ±2% difference interval. The exposure times were 120s/frame without rotation, tilt, or XY stage oscillation. The separation step between two grid points was 100 µm in both X and Y directions. A fixed X-ray beam incident angle θ_1 = 14 and detector angle of θ_2 = 14 were used to collect 1083 frames with a 2θ interval of 18° to 38°.

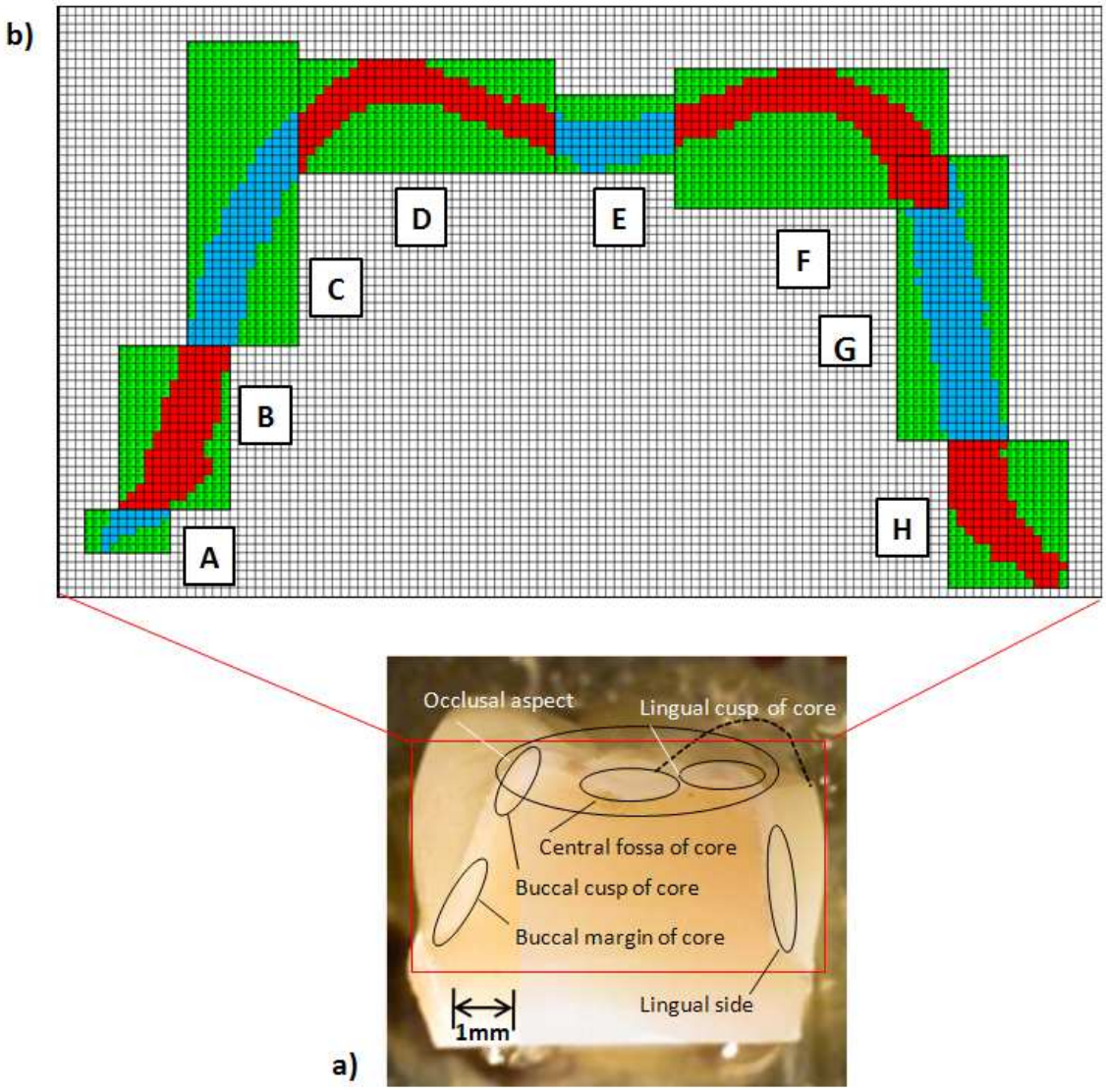

Figure 15 a) Chipped veneer is indicated by a dashed line. b) Graphical representation of the mapped area.

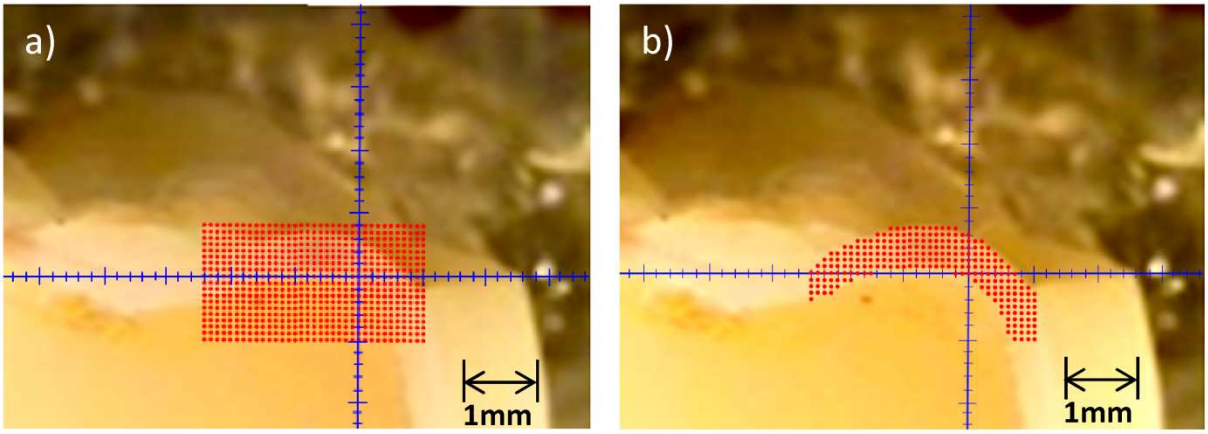

Figure 16 a) initial grid points with 100µm separation steps b) selected point for micro-XRD mapping located on the zirconia surface.

3.3 Results

Selecting a 2θ interval for the frames and finding an optimum exposure time per frame is an important step for designing XRD mapping experiments. Initially, two patterns consisting of 6 frames were collected over a 2θ range from 4.4° to 98.5° for individual points labeled in Figure 17a and b numbered 1 and 2. Point 1 was selected underneath the chipped porcelain cusp in the interface region with zirconia, while point 2 was chosen at the border of the inside surface of the zirconia core. The resulting merged frames using Bruker's Pilot software is illustrated in Figure 17c and Figure 17d. Figure 17e illustrates χ integration of 2D diffraction data as intensity versus 2θ.

X-ray diffraction at location 1 shows zirconia was completely tetragonal and had no observable monoclinic peaks while measurement at location 2 indicates significantly intense monoclinic reflection peaks in addition to tetragonal peaks. The best frame (2θ

range) for phase transformation mapping was the second frame that has high counts per frame as well as high intensity peaks for both the monoclinic and tetragonal phases.

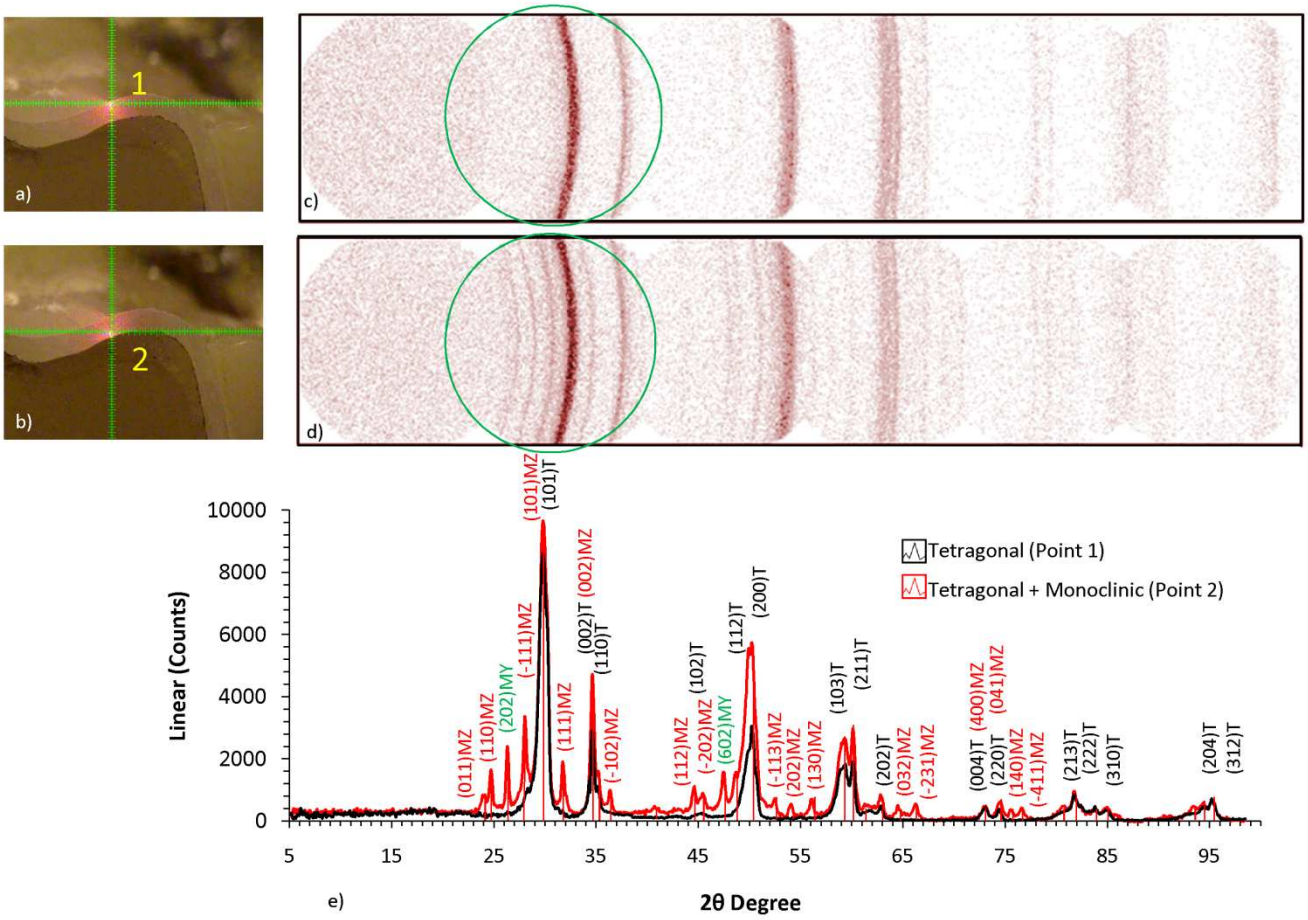

Figure 17 a) A selected point for micro-XRD underneath the chipped porcelain cap, b) a selected point at inside surface of the zirconia, c) six merged diffraction pattern frames in the region that zirconia was completely tetragonal, d) observable monoclinic peaks in addition to tetragonal, e) indexed micro-XRD spectra showing phase identification for two selected regions.

The micro X-ray diffraction pattern collected at point 1 has three tetragonal Zirconium Yttrium Oxide peaks (101, 002, and 110) at 2θ diffraction angles between 18° to 38° according to 01-070-4426 ICDD (International Center for Diffraction Data) phase

identification card while diffraction collected at point 2 in addition to these three tetragonal peaks, has six monoclinic related peaks. These additional monoclinic peaks match card 01-089-9066 for monoclinic Zirconium Yttrium Oxide (011, 110, -111, 111, and -102) and 01-039-1064 for monoclinic Yttrium Oxide (202). They were extracted for all data using GADDS mapping software and results were saved as a matrix.

The peaks at the frame that show monoclinic crystal structure are brighter and that frame has more background scattering compared to corresponding frames with pure tetragonal phase, keeping the same diffractometer parameters and exposure time. Compared to the tetragonal phase, the monoclinic phase has less symmetry which results in more observable peaks. Although during data collection, all system parameters were kept constant, the complex sample geometry and ranges of phase transformation cause different total counts per frame and inconstant background level among locations.

To remove the background effect on mapping, a relative background for each frame was estimated from χ integration over the area that was clear of diffraction (no peaks) for all sets of collected frames. A selected region for relative background calculation is illustrated on a typical frame in Figure 18. Figure 19b instead of the total area under the 3 monoclinic related peaks, the same area under the 3 peaks divided by the corresponding relative background after normalization to one is plotted.

3.4 Discussion

Contour plots of transformed structure labeled as impacted region at Figure 19b indicates that the zirconia poly crystalline tetragonal structure greatly exhibits phase transformation to monoclinic at the impacted region up to 100%. This phase transformation is generally

associated with stress concentration near the damage site and the initial residual stress state. The initial residual stress would be created during firing followed by cooling and the strain interference due to coefficient of thermal expansion mismatch between the core and veneer layers. This initial residual stress can be relaxed during phase transformation as the monoclinic crystal has a larger volume than tetragonal.

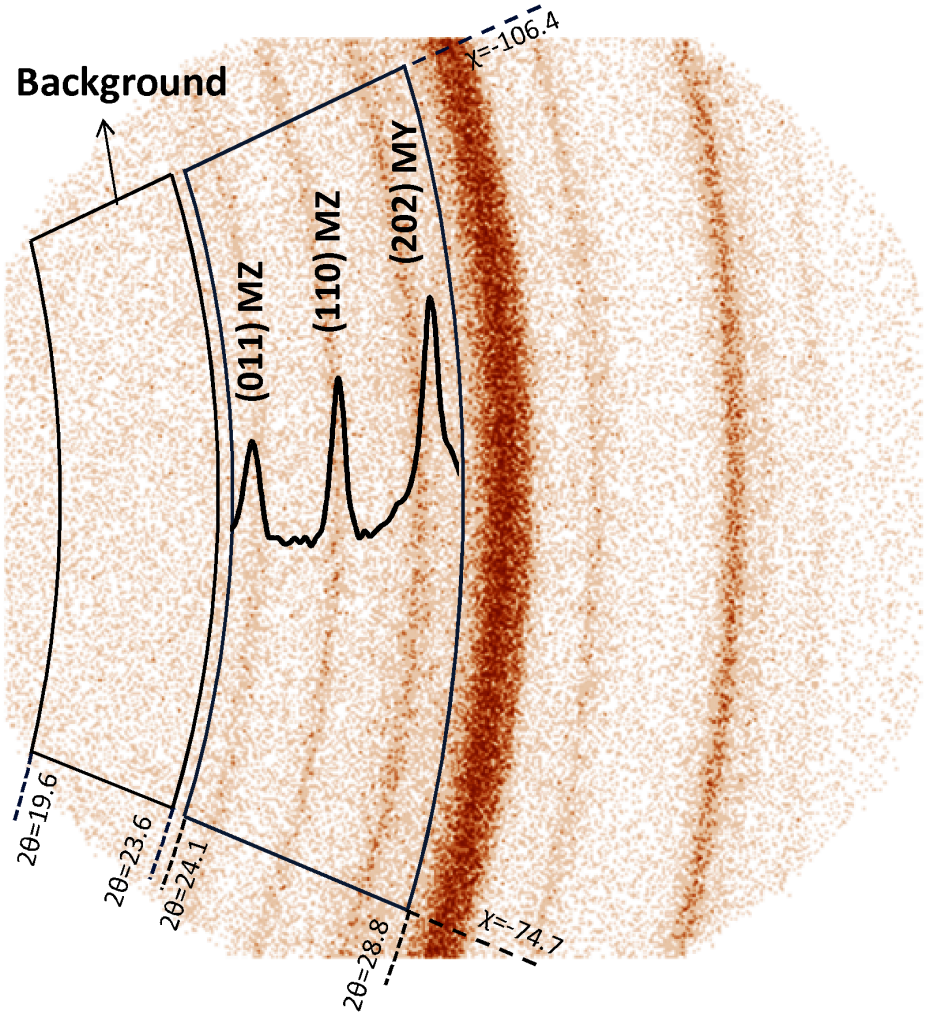

Figure 18 the integration range for 3 monoclinic related peaks and selected region for background estimation.

Interestingly, the phase transformation map reveals that on the lingual side of the zirconia core, the inner mounting surface has more monoclinic phase fraction relative to its outer veneered side. This is also true for the buccal side, but less so. For better illustration, these regions are separated by dashed lines in Figure 19b.

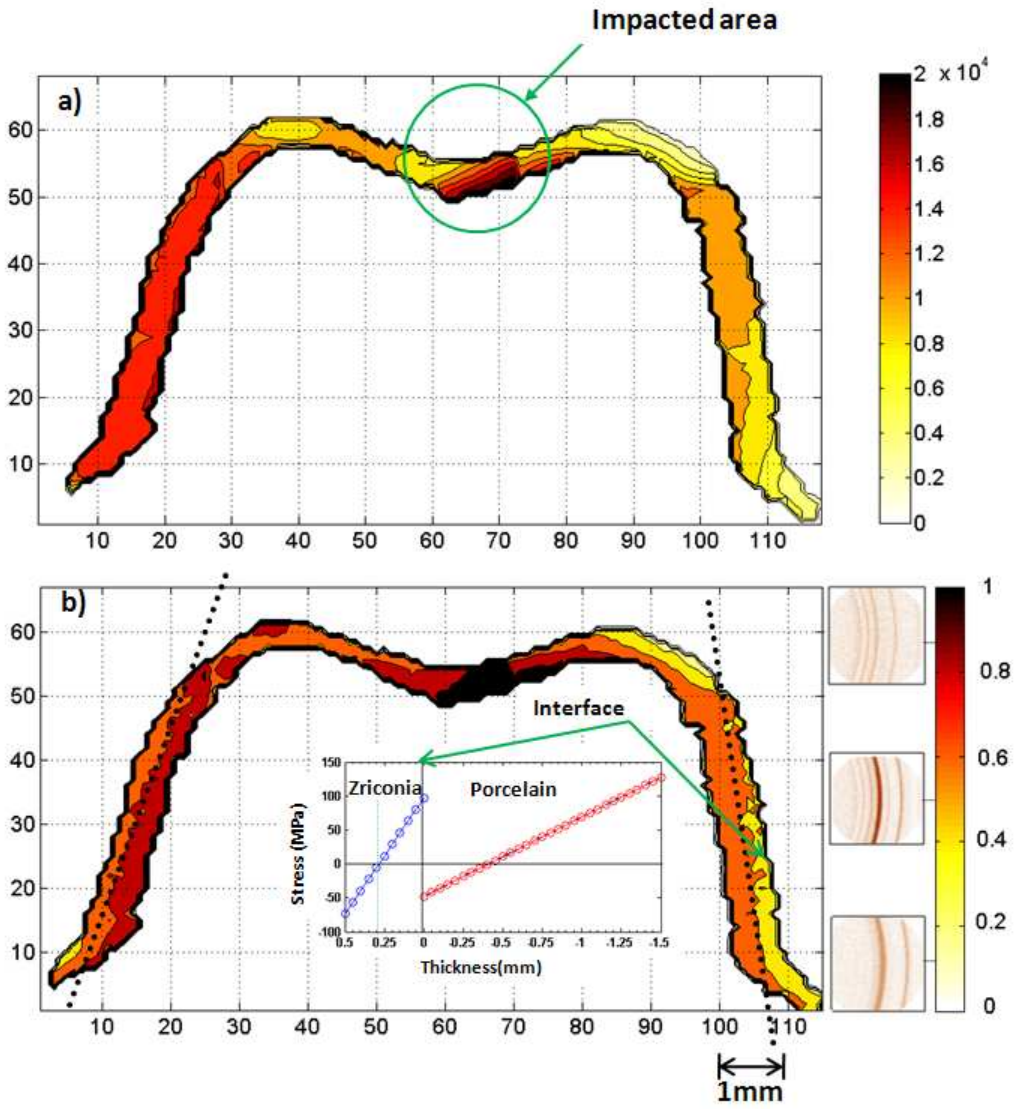

Figure 19 a) Contour plot that represents the total area under 3 selected monoclinic peaks b) divided to relative background and normalized to one contour map plot. Inset shows

theoretical residual stress calculation along the line between surface of porcelain and external surface of zirconia.

Dental crowns have a non-trivial geometry and, in general, the veneering layer is not thin compared with the curvature radius of the zirconia layer. They cannot generally be considered locally flat. But at these side locations, the crown resembles a flat plane with constant 0.5 mm zirconia thickness. It is known that residual stress is a function of a layer's thickness and distance from the interface in bi layer ceramics systems [26,39]. An analytical solution [27] for the residual stress profile for a line that starts at the surface of porcelain and passes through the interface and ends at the external surface of zirconia is shown as inset plot in Figure 19b. The interface stress at the zirconia side is tensile (+100 MPa) and compressive on the external side (-70 MPa) and changes linearly in this interval. When an external compressive load is applied to the crown, the initial tensile residual stress at the veneer side can be relaxed. While the inner section of lingual side, that has initial compression residual stress, undergoes more compression and would be more susceptible to phase transformation.

In order to evaluate this hypothesis that tetragonal zirconia transforms to monoclinic to relax the compression stress, a map of lattice strain related to the (101) plain was implemented in the following way. Common strain mapping involves extracting the lattice strain for a given plane for all data points. Here an interval of less than ± 0.0001 change from the unstressed d-spacing was considered criteria. Shift in the tetragonal (101) peak was considered for strain calculation, and if strain related to this peak in a particular frame was detected in the interval of less than ± 0.0001, the frame was

evaluated as pass (black color areas on Figure 20) otherwise according to the strain magnitude, a corresponding color bar was assigned to the measurement location on the map. It means that frames corresponding to the locations that do not have too much strain in (101) direction will pass. This color and pass map is illustrated in Figure 20.

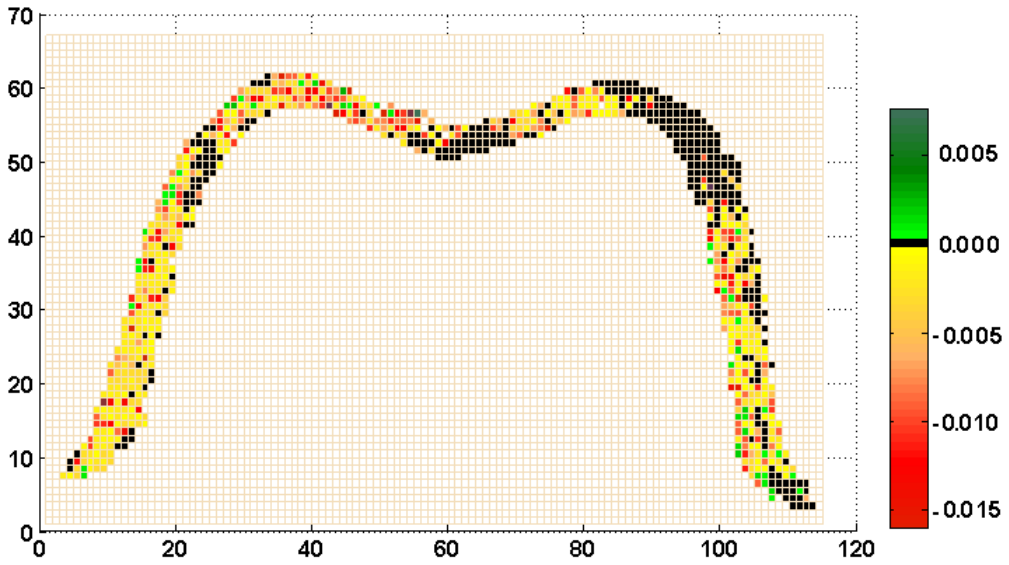

Figure 20 pass and color map for tetragonal related (101) crystal plane lattice strain.

An interesting result is that at both regions where pure tetragonal phase and highly monoclinic phase were observed, there is less strain. In the other words they have less residual stress after fracture. A high fraction of phase transformation and low stress state at the impacted region proves the mechanism of stress relaxation by phase transformation. Although the mechanism of stress relaxation via phase transformation might create some micro cracks that can propagate by fatigue and impacts the total life time of the crown, it slows zirconia from failure under the localized compression load.

This mechanism helps explain reports about the failure of veneers by chipping without exposing the zirconia support layer [5]. When high stress load is applied to the zirconia-porcelain system, high stress state location in zirconia undergoes the stress induced phase transformation providing stress relaxation reducing the potential energy for crack initiation and growth in zirconia layer rather than the porcelain layer.

3.5 Conclusion

Tetragonal to monoclinic phase transformations were observed in 2D micro X-ray diffraction frames from yttria stabilized zirconia using a 200 µm diameter X-ray beam. Over a thousand frames with 100 µm step size were collected over eight sub regions to cover the total cross sectional area of a sectioned crown, which exhibited failure under a single load. A typical frame was indexed and the area under three monoclinic related peaks indicated the phase transformation area for mapping. The zirconia polycrystalline tetragonal structure greatly exhibits phase transformation at the impacted region due to compressive stress concentration. An analytical model for the lingual side, which was approximated as locally flat, indicates that the inner side of the zirconia layer is under compressive residual stress while the other side (veneer) is under tensile stress. In this case, it was observed that the inner section of the lingual side of the zirconia core has more monoclinic phase than the outer side. This is because initial tensile residual stress at the outer section of the lingual side relaxed while the inner section lingual side, that had initial compressive residual stress, underwent more compression and is more susceptible to phase transformation with an external compressive applied load. Results of an elastic strain map for the (101) tetragonal peak suggests stress relaxation by phase

transformation. The pure tetragonal phase and highly monoclinic phase do not show considerable shifts in 2θ corresponding to low lattice strains. Such observations should be typical for this crown design and the methods described here can be used to further review and validate future designs, the selection of veneering materials and the appropriateness of their CTEs, and processing of those crowns, such as different firing programs.

CHAPTER IV

4 X-ray diffraction mapping on a curved surface

An efficient method for X-ray diffraction data collection mapping on a given curved surface was developed. The method uses a video-laser auto z alignment system to collect the map of heights on a fine mesh grid. It also reconstructs the surface geometry and determines surface normals on the 3D surface fit. An algorithm was used to calculate the required rotation and tilt angles to coincide the sample normal with the diffraction center before each exposure. Collected diffraction frames were analyzed to superimpose a phase transformation map on a typical zirconia ceramic sample. With this method, mapping of phase on a complex surface was demonstrated. It is a method broadly applicable to many important studies.

4.1 Introduction

A wide range of industrially important materials, from aircraft engine parts to welds and even dental crown ceramics can have complex shapes and potentially detrimental residual stress or phase distributions. Micro X-ray diffraction is a nondestructive technique that provides the information on mapped regions of interest [40]. In general, X-ray diffraction mapping involves analysis and comparison of several diffraction patterns of

multiple samples that change as a function of two independent variables. Common mapping is restricted to the surface of a flat sample and two independent variables are *x* and *y* coordinates. Some uncommon methods allow true 3-D mapping of stresses, but the software tools in use today still generally restrict users to regularly spaced grids. For 2-D, mapping can easily be done on a selected position of a rectangular grid or with arbitrary distances in both *x* and *y* directions. In recent years, with advances in focusing micro X-ray lenses that provide high intensity, point size beams down to a few micrometers diameter [41], and two dimensional (2D) detectors; short time diffraction measurements down to few seconds have become possible [80]. Accurate motorized XYZ axis stages in a variety of configurations along with an auto *z*-alignment system, such as a laser video system, are available to fulfill the requirement of sample auto positioning to the diffraction center and height adjustment with high precision and repeatability.

Advances in X-ray optics, precise automatic sample positioning, and dramatic reduction in data collection time provide the basic requirements for X-ray diffraction mapping development. Current commercially available mapping algorithms are restricted to collecting data on the surface of relatively flat samples [42]. X-ray diffraction mapping has been implemented for compound control process [43] or many other applications [44,45]. This study demonstrates an efficient algorithm for X-ray diffraction data collection on complex curved shape surfaces. This method relies on the predetermination of locally specified sample rotation and tilt before each exposure and efficiently

overcomes the problem of shadowing by some parts of sample before reaching the desired point or blocking the diffracted beam by another protrusion of the surface.

4.2 Sample shadowing problem and the 2D detector

Because of geometry, collecting appropriate diffraction results at some positions of a curved surface without rotating and tilting is not possible.

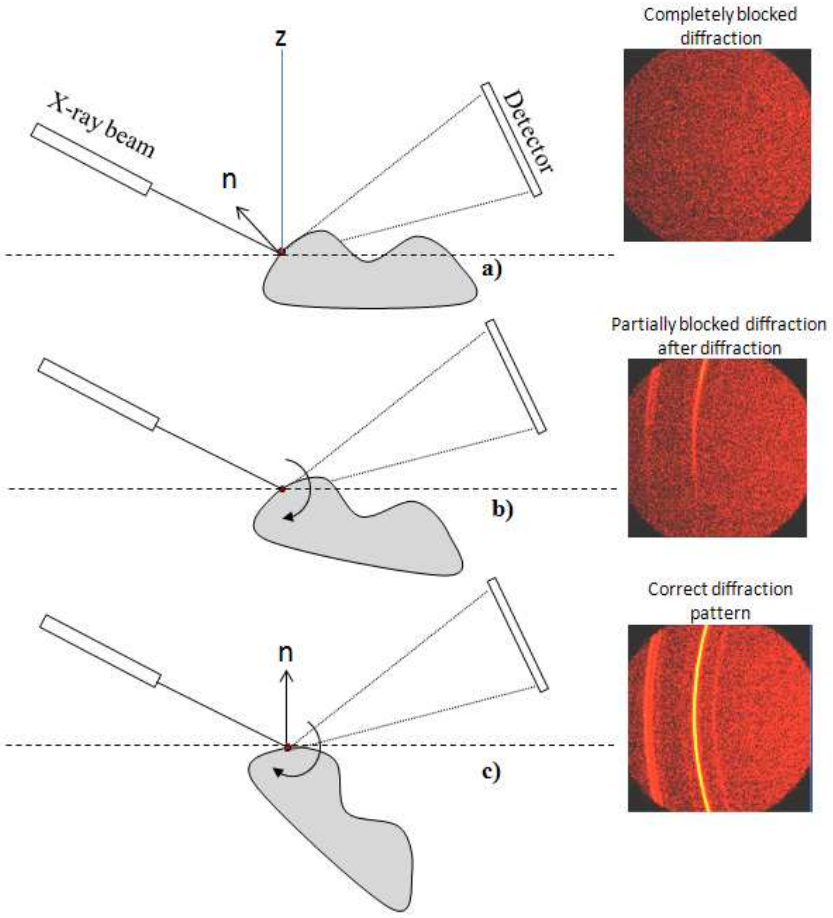

Figure 21 a) A completely blocked diffraction (shadowing) by the sample b) by rotating the sample around exposure point diffraction is partially unblocked c) totally removed detector from shadowing of sample by a proper rotation.

The reason is a part of surface may block the X-ray beam before reaching the desired point or diffracted rays might be blocked partially or completely before reaching the detector.

A blocked diffraction before reaching to the detector schematically is shown in Figure 21a. This shadowing is avoidable by a proper sample rotation around the exposure point. Figure 21and c illustrate two different rotations that could partially and completely solve this shadowing. For a regular curved surface, the best rotation is a rotation that makes the sample surface normal parallel to the instrument z direction, as shown in Figure 21a, and c. In the case of mapping, several measurements on surface is needed, finding proper rotation and tilt angles is challenging and requires knowledge of the local geometry information to calculate the normal vector at each measurement point. Knowing that sample stage rotates or tilts around the center of the instrument which is the same as exposure point, if we bring the measurement point on sample to the center of instrument, all three will coincide. The idea is to calculate the required rotation angles for each specific measurement point. Therefore at each measurement, first we locate the measurement point at center of the instrument and apply its pre calculated rotations as shown in Figure 22. This means each measurement point has its own calculated rotation angles from geometry that will be applied when it is located at center of the instrument for exposure.

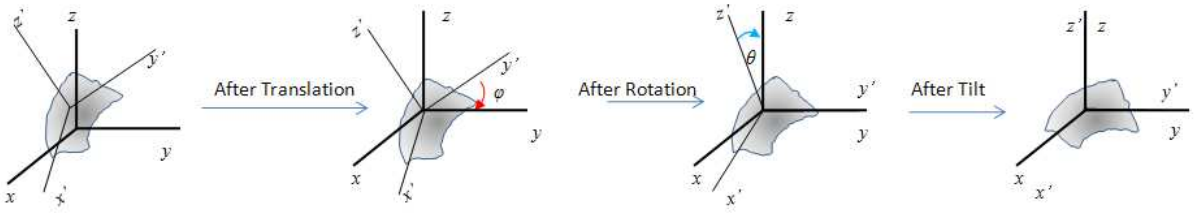

Figure 22 Translation and Euler's rotations required before each exposure.

In this study, the sample is considered to be poly crystalline such that grains are oriented randomly. In polycrystalline materials, just some of the irradiated grains that satisfy the diffraction law, will diffract. Rotating the sample around the exposure point keeps the irradiated volume at exposure location while different set of grains at the same volume might diffract.

4.3 Auto z alignment laser-video system

Laser-video sample alignment assists in positioning the sample into the instrument center before or during data collection. An associated optical microscope allows the user to directly observe the magnified sample, laser pointer, and a cross hair. The cross hair, laser pointer, and X-ray beam must be calibrated to coincide at instrument center. Figure 23 schematically illustrates that by moving the sample up and down, the cross hair, laser, and desired point could be located at the same position.

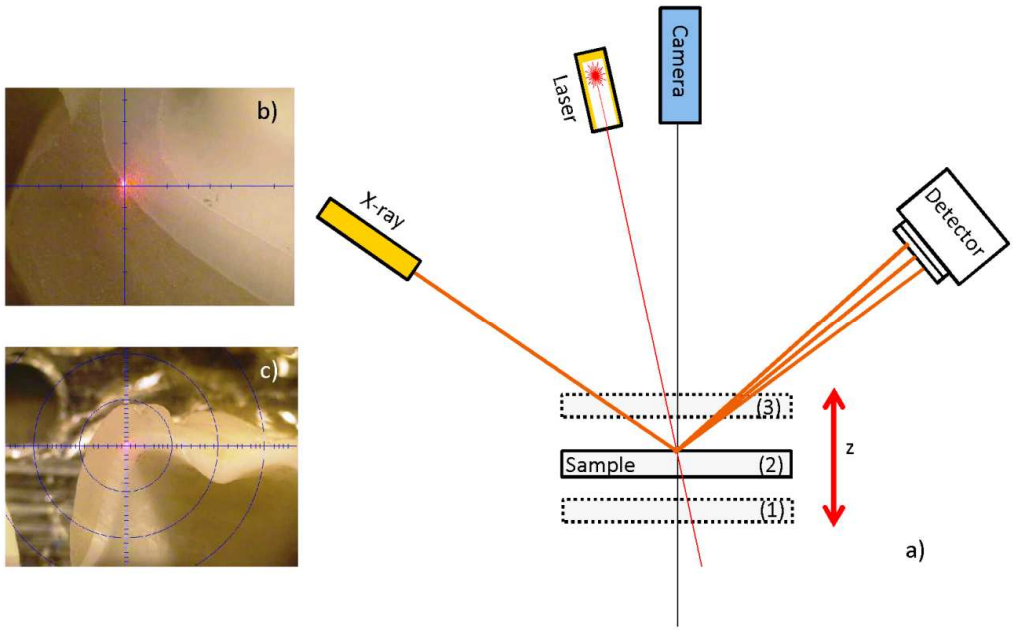

Figure 23 a) Schematic of laser-video sample alignment system in D8 Discover X-ray diffraction b) and c) image of laser spot and crosshair with two different magnifications.

4.4 Topography measurement by laser-video

A polycrystalline yittria stabilized tetragonal zirconia crown was selected for its complex geometry. To find the geometry, heights of 700 points (25×28) on the surface of the crown spaced by 250µm in both x and y directions were measured by the auto z-alignment laser video system. Figure 7a, shows a top view from optical microscopy of the crown with a target grid (red). The initial z values for all points were assigned a convenient constant, and the system was allowed to find the correct z value for the points. The result of determined z values overlaid on a tomography representation of the crown as validation of the measured heights is illustrated in Figure 7b. Point heights obtained from laser video auto z measurement properly superimpose on the tomography geometry,

validating the laser based method for auto geometry correction. An advantage of this laser method is the geometry information available at the current instrument reference frame which eliminates problems related to reference matching, scaling, and rotation transformation involved with using predetermined sample geometries. A predetermined geometry might be collected before installing the sample on the XRD measurement stage using other available techniques such as laser scanning [46] or micro X-ray tomography [47,28].

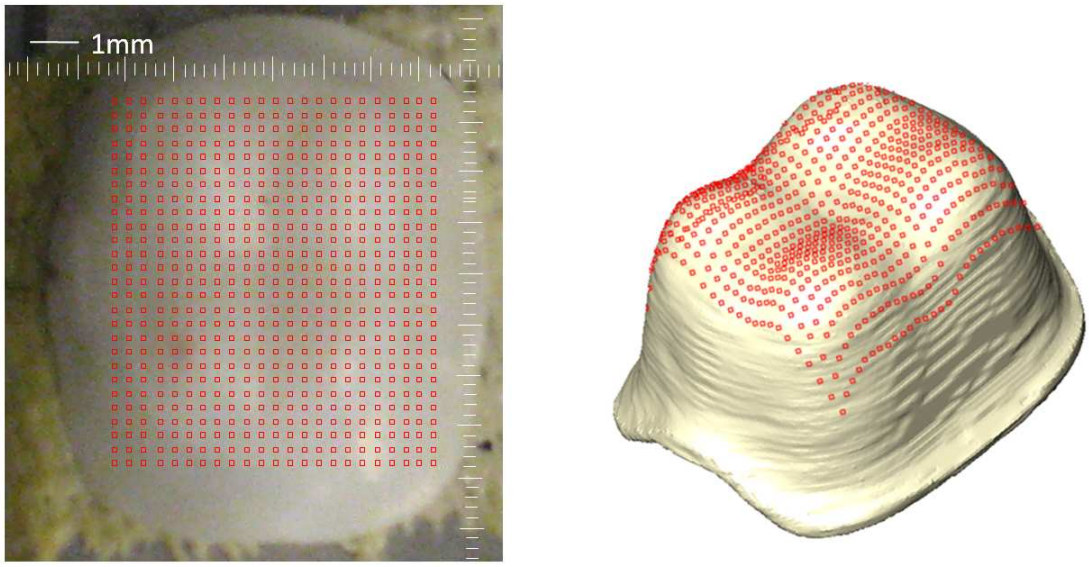

Figure 24 a) Typical optical image from the video system and a top view of the grid (25×28) b) Points heights obtained from the laser video Auto *z* measurement superimposed on a 3-D rendering of the sample surface from tomography.

4.5 Surface normal calculation

Normals to the 3D surface, generate a vector field that assigns a unit length vector $\boldsymbol{n}_i$ at each point $\boldsymbol{X_i}(x_i, y_i, z_i)$ of its domain (mapped area). The vector field $\boldsymbol{n}$ has a component

scalar field n_x, n_y and n_z and is perpendicular to the tangent plane to each surface point of its domain.

$$\boldsymbol{n} = n_x(x,y,z)\,\hat{\imath} + n_y(x,y,z)\,\hat{\jmath} + n_z(x,y,z)\,\hat{k} \qquad \textbf{4-1}$$

Where

$$\boldsymbol{n}.\boldsymbol{n} = {n_x}^2 + {n_y}^2 + {n_z}^2 = 1$$

At each $\boldsymbol{X_i}(x_i, y_i, z_i)$ point of domain there are two directionally opposite unit normal vectors. The normal direction is considered to be pointing outside to satisfy uniqueness. Computed outward pointing unit normal vectors are displayed at Figure 25.

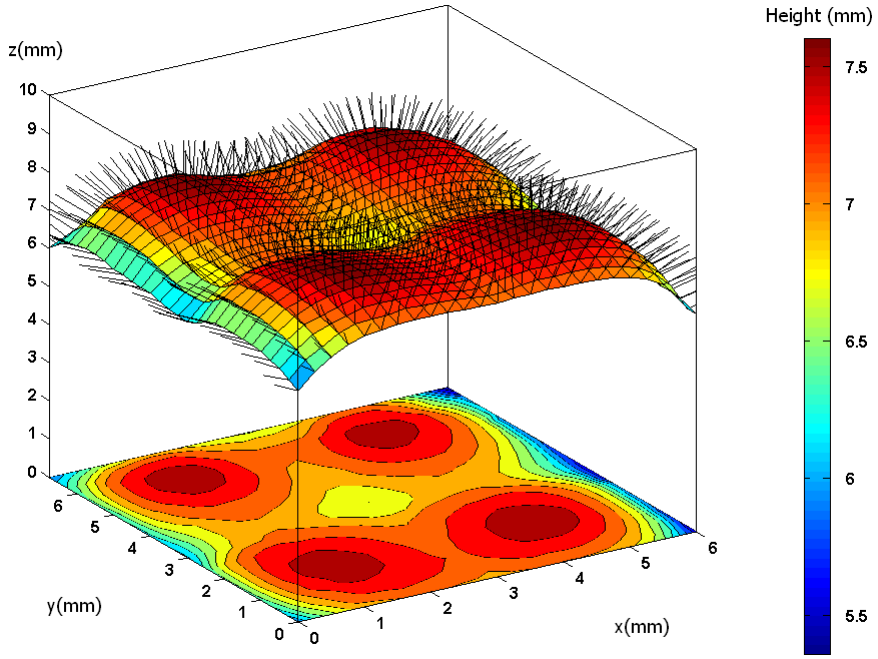

Figure 25 Outward pointing unit normal vectors for domain of measurement points.

Figure 26 shows graphically that by ϕ angle clockwise rotation about z-axis followed by χ degree clockwise tilt around *x*-axis, the sample normal at the point *P* could be collinear with the *z*-axis and equal to $\hat{k}$. In matrix notation two required matrixes are,

$$R_x(\chi).R_z(\phi).\boldsymbol{n} = R_x(\chi).\boldsymbol{n_1} = \begin{bmatrix}1 & 0 & 0\\ 0 & \cos\chi & -\sin\chi\\ 0 & \sin\chi & \cos\chi\end{bmatrix}\begin{bmatrix}\cos\phi & -\sin\phi & 0\\ \sin\phi & \cos\phi & 0\\ 0 & 0 & 1\end{bmatrix}\begin{bmatrix}n_x\\ n_y\\ n_z\end{bmatrix} = \boldsymbol{n_2} \qquad \textbf{4-2}$$

We are looking for the particular rotation ϕ angle in such way that rotates the vector $\boldsymbol{n} = n_x\hat{\imath} + n_y\hat{\jmath} + n_z\hat{k}$ and produces $\boldsymbol{n_1} = \acute{n}_y\,\hat{\jmath} + \acute{n}_z\,\hat{k}$

$$R_z(\emptyset).\boldsymbol{n} = \begin{bmatrix}\cos\phi & -\sin\phi & 0\\ \sin\phi & \cos\phi & 0\\ 0 & 0 & 1\end{bmatrix}\begin{bmatrix}n_x\\ n_y\\ n_z\end{bmatrix} = \begin{bmatrix}0\\ \acute{n}_y\\ \acute{n}_z\end{bmatrix} = \boldsymbol{n_1} \qquad \textbf{4-3}$$

Equation 4-3 is equal to three equations and three unknowns $\acute{n}_y$, $\acute{n}_z$, and ϕ

$$\begin{gathered}\cos\phi n_x - \sin\phi n_y = 0\\ \sin\phi n_x + \cos\phi n_y = \acute{n}_y\\ n_z = \acute{n}_z\end{gathered} \qquad \textbf{4-4}$$

Substituting ϕ from first equation in second equation,

$$\begin{gathered}\phi = \cot^{-1}\left(n_y/n_x\right)\\ \acute{n}_y = \sin\left(\cot^{-1}\left(n_y/n_x\right)\right)n_x + \cos\left(\cot^{-1}\left(n_y/n_x\right)\right)n_y\\ \acute{n}_z = n_z\end{gathered} \qquad \textbf{4-5}$$

The ϕ rotation could transfer the surface normal to be coplanar with *y*-*z* plane while $\acute{n}_y$ has $\pm\hat{\jmath}$ direction. Because the system driver for χ movement has drive limits from -5° to 55° however to help prevent collisions 48° was used as the maximum, only rotation was considered that leads to $\acute{n}_y$ with $-\hat{\jmath}$ direction, in order to use the χ interval of 0 to 48° for the subsequent tilt.

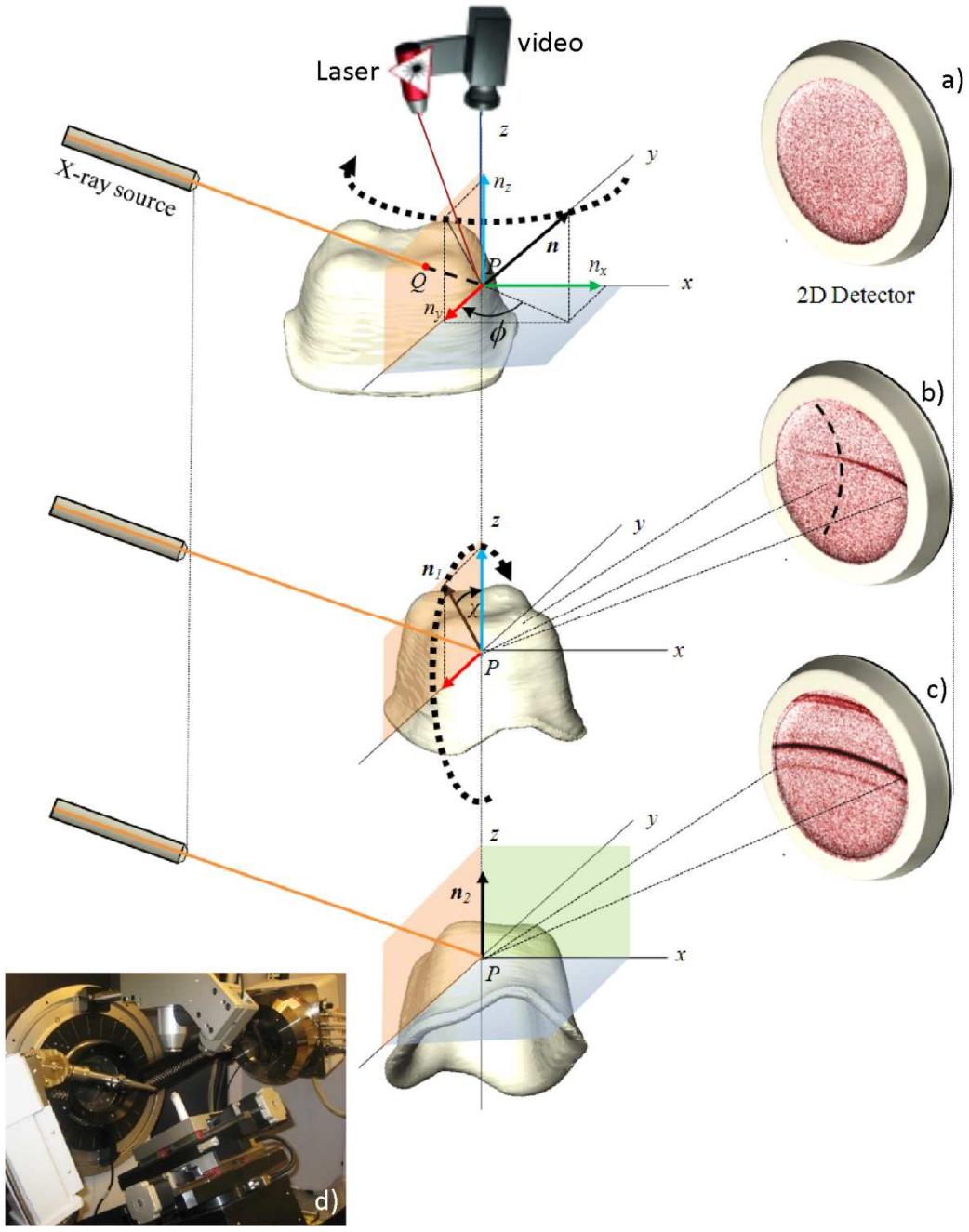

Figure 26 Diagram of example cases showing, a) the X-ray beam stopped by the sample at point Q, b) the Diffracted beam blocked by a part of the sample. c) The configuration after proper rotation and tilt. d) Photograph of the experimental set up. a, b, and c are not to scale.

For this purpose, at the first and second quadrant, $\pi+\phi$ was considered denoting that ϕ has a negative sign at the second and fourth quadrant and $\pi+\phi$ for the fourth quadrant. Figure 27 represents the ϕ angle at different quadrants and required rotation to make $\acute{n}_y$ parallel to$-\hat{j}$.

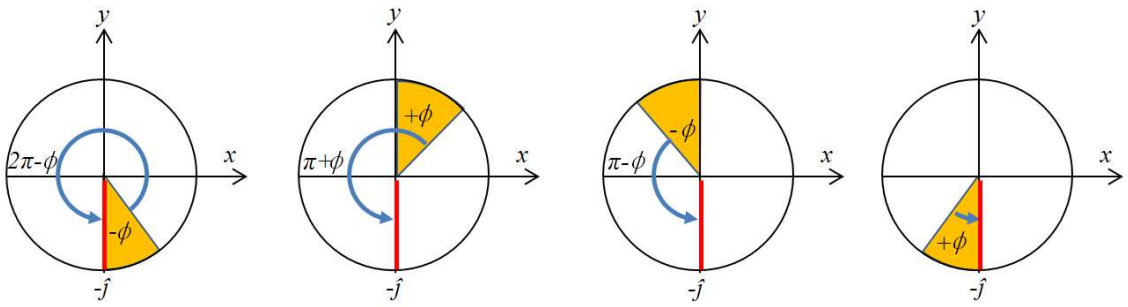

Figure 27 The ϕ angle at different quadrants and required rotation to make $\acute{n}_y$ parallel to $-\hat{j}$.

The next step is to tilt the sample in order make surface normal collinear with the z-axis.

$$R_x(\chi).\boldsymbol{n_1} = \begin{bmatrix} 1 & 0 & 0 \\ 0 & \cos\chi & -\sin\chi \\ 0 & \sin\chi & \cos\chi \end{bmatrix} \begin{bmatrix} 0 \\ \acute{n}_y \\ \acute{n}_z \end{bmatrix} = \begin{bmatrix} 0 \\ 0 \\ n_z'' \end{bmatrix} = \boldsymbol{n_2} \qquad \textbf{4-6}$$

From above equations we can get,

$$\cos\chi.\acute{n}_y - \sin\chi.\acute{n}_z = 0 \Longrightarrow \chi = \tan^{-1}(\acute{n}_y/\acute{n}_z) \qquad \textbf{4-7}$$

Based on the algorithm explained in the previous section, a Matlab code (Appendix 3) was developed that calculates the required tilt and rotation angle for all data points using the z height matrix data. The output result for χ and ϕ are illustrated in Figure 28.

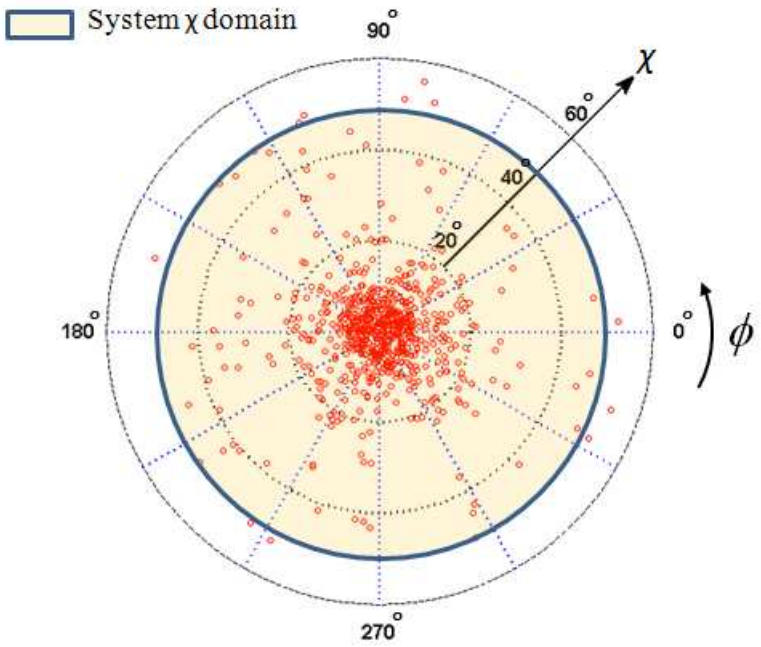

Figure 28 Representation of required tilt and rotation with system tilt drive limit.

Only a few of the 700 measurement points (10 points) reqire a tilt outside our system driving limits, and for those few points, the nearest possible χ were considered. This output was entered in a script file that is understandable for the machine data collection software. Figure 29b shows the calculated ϕ that is an angle in ±90° interval depending on point location on crown.

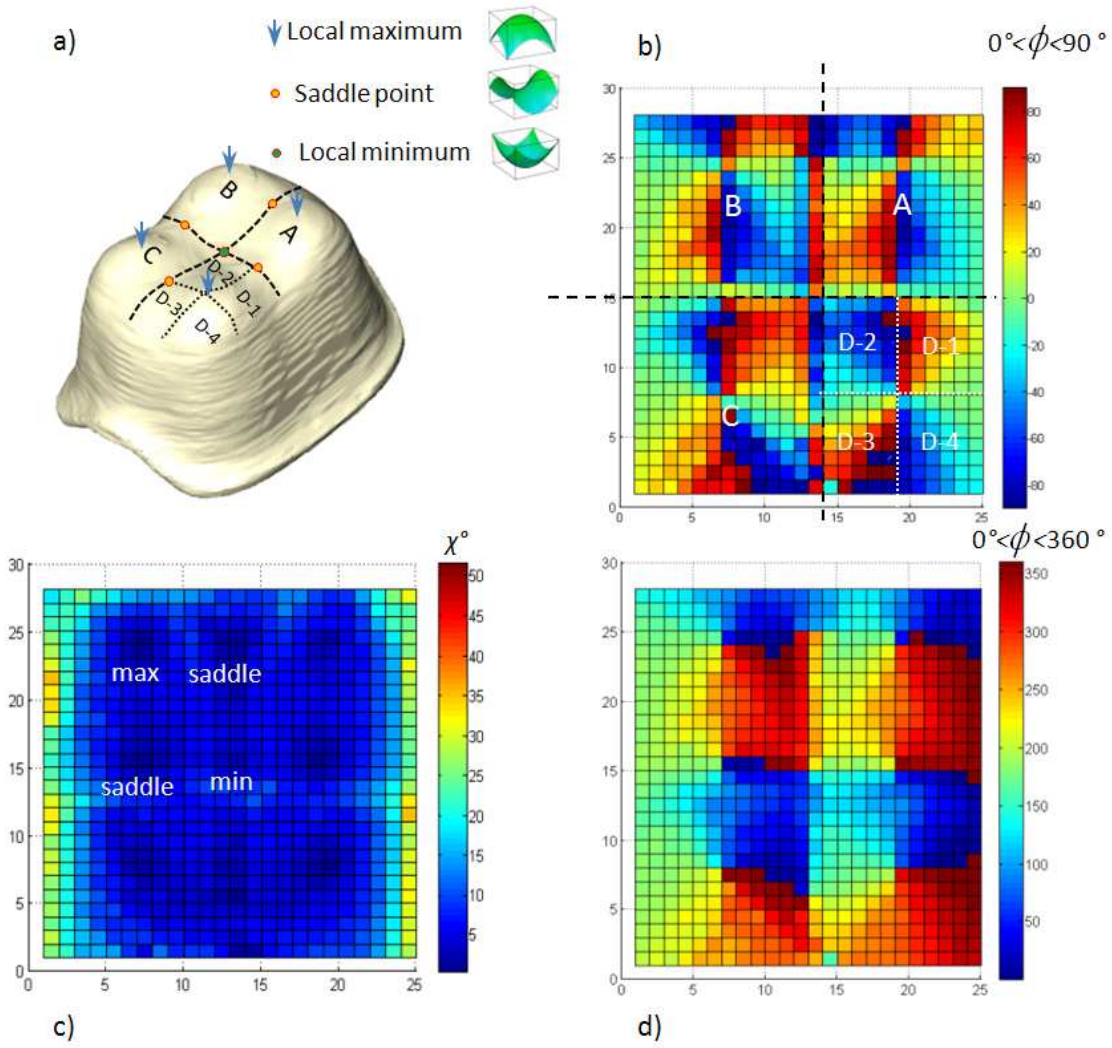

Figure 29 a) Four geometrically similar regions on the crown b) Calculated rotation angle ϕ in ±90° interval c) Required tilt angle χ d) Required rotation angle ϕ in 0-360° interval.

Figure 29c and d show the calculated required rotation (0 to 360°) and tilt values to be fed to the machine respectively for each exposure point on the curved surface. These results are in agreement with what we expect from the symmetry and shape of the crown. For example, we have four similar cusps on the crown and the ϕ matrix (Figure 29) has four comparable sub regions named A, B, C, and D areas in Figure 29a.

4.6 Flow chart

In order to summarize the method, lists the step-wise process of data collection and analysis of diffraction data on a given curved surface.

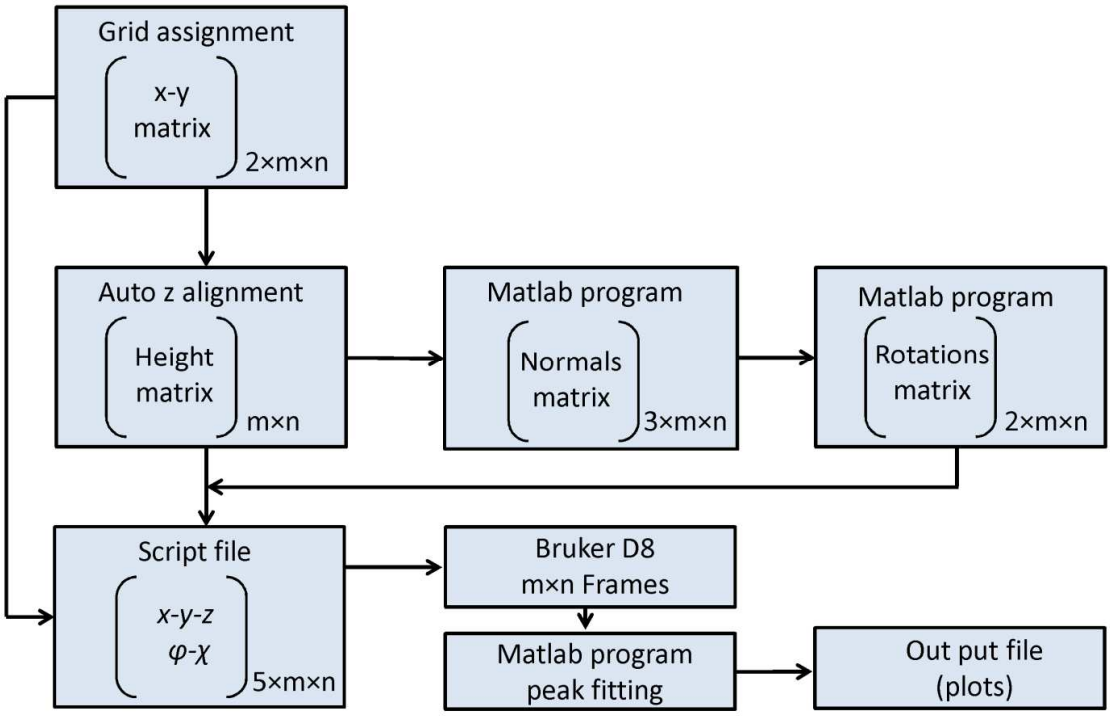

Figure 30 Flow Chart of the data collection procedure.

4.7 Genetic algorithm and collecting time optimization

The aim of this algorithm is to optimize the data collection time of the developed method for X-ray diffraction data collection mapping on a given curved surface. The total data collection time depends on a time needed per each frame and a time required for sample adjustment before each exposure. Assigned exposure time per frame is an arbitrary constant variable but sample adjustment required time between two subsequent adjustments could be minimized. In the interval between two exposures, the system simultaneously translates measurement point to the center of diffraction by *x*, *y* and *z* movement of the stage, tilts and rotates the sample to coincide the sample surface normal with instrument *z* axis. The control system starts *x*, *y*, and *z* movements, tilt, and rotation at the same time. As a result, the total time for this geometry adjustment depends on the slowest driver. The required time for *x*, *y*, and *z* stage movement is always less than the time required for tilt and rotation. Therefore the total sample geometric transformation and rigid body rotations time depend on total required tilt time or rotation time. This required time for the tilt and rotation depend on their initial and final angular position.

$$t = \sum_{i=1}^{N} (t_i^{exp} + t_i^{adj}) = N t_1^{expo} + \sum_{i=1}^{N} \boldsymbol{t_i^{adj}} \qquad 4\text{-}8$$

Where *t* is the total time needed for experiment, t_i^{expo} is exposure time at *i* location, *N* is total number of measurement points and t_i^{adj} is the interval time required for sample adjustment between two exposure**.**

$$\sum_{i=1}^{N} t_i^{adj} = \sum_{i=1}^{N} \max\left(t_i^{rot}, t_i^{tilt}\right) \quad \textbf{4-9}$$

The required time for the system to go to the next angular configuration depends on the current angular position and it is linear function of angular difference.

$$t_i^{rot} = f(\varphi_i, \varphi_{i-1}) = \frac{|\varphi_i - \varphi_{i-1}|}{v^{rot}} + t_{\mathrm{o}}^{rot}$$
$$t_i^{tilt} = f(\chi_i, \chi_{i-1}) = \frac{|\chi_i - \chi_{i-1}|}{v^{tilt}} + t_o^{tilt} \quad \textbf{4-10}$$

Where v^{rot} and v^{tilt}, are constant drivers velocity. t_{o}^{rot} and t_o^{tilt} are additional constant died time required by system to start and stop process irrespective to the magnitude of tilt and rotation. These four constant were obtained from curve fitting on a set of drivers velocity measurements illustrated in Figure 31**.**

The following values were used for optimization program,

$v^{rot} = 6.3 \pm 0.01$ deg/s, $v^{tilt} = 1.00 \pm 0.01$deg/s and $t_{\mathrm{o}}^{rot} = t_{\mathrm{o}}^{tilt} = 10.15 \pm 0.01\ s$.

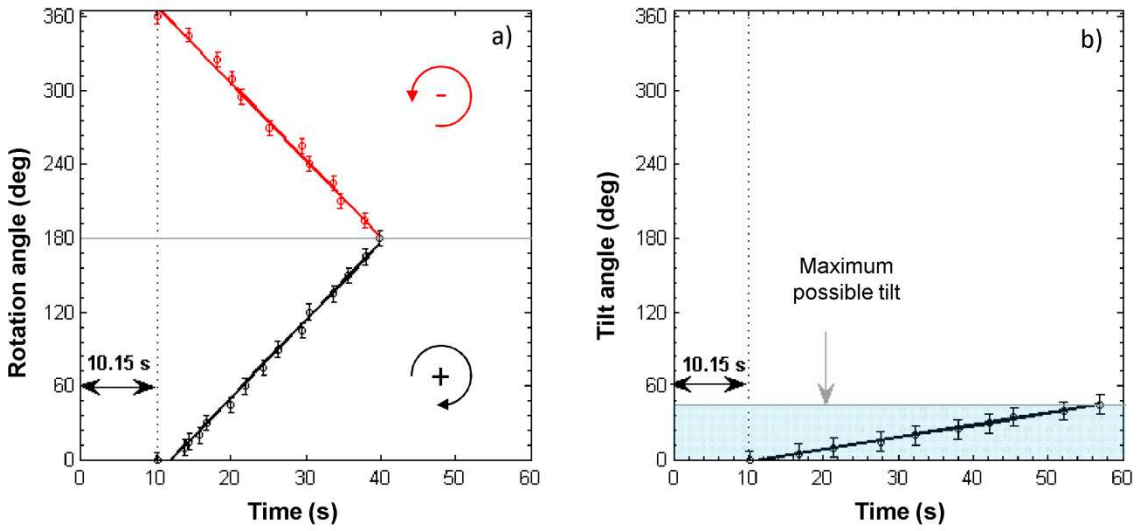

Figure 31 a) rotation angle vs. time b) tilt angle vs. time.

It should be mentioned that the control system will rotate the stage in both clockwise and anticlockwise directions to achieve the desired configuration. It selects the direction that takes less time. Because of this, the maximum required time for rotation is for 180°. The curve is symmetric with respective to this maximum point.

4.7.1 The geometric map from angular space to Cartesian

In this section, we are interested in a mathematical map from an angular space to a subset of $\mathbb{R}^2$ which enables us to implement a conventional genetic algorithm for traveling salesman problem to minimize the required time in our problem of tilts and rotations. The idea is to convert the data from angular space to the Cartesian space, minimize the path and then convert the optimized data back to the angular pace. It should be mentioned that angular space is not polar space because both χ and ϕ are angles. Let domain $\boldsymbol{D}^*$ be a subset of angular space and $\boldsymbol{T}: \boldsymbol{D}^* \rightarrow \mathbb{R}^2$, so $\mathbf{T}$ takes points in domain $\boldsymbol{D}^*$

to points in $\mathbb{R}^2$. Let's denote the set of image points by domain $\boldsymbol{D}$. Figure 32 illustrates a map $\boldsymbol{T}$ that takes a disk region to the rectangular region and $\boldsymbol{T}'$ that maps the rectangular back to a disk region. Using this geometric one to one map, required tilt and rotation angles assumed to be the *x* and *y* coordinates of the targets in Cartesian coordinates illustrated in Figure 33**.**

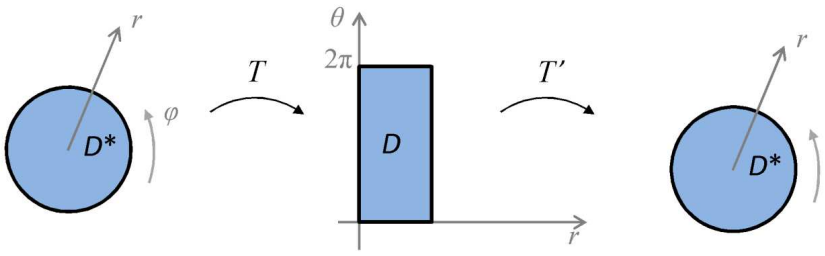

Figure 32 A function *T* from a disk *D to a rectangular region *D* changes the variables between angular space and Euclidean space, and inverse function T' from *D* to *D*.***

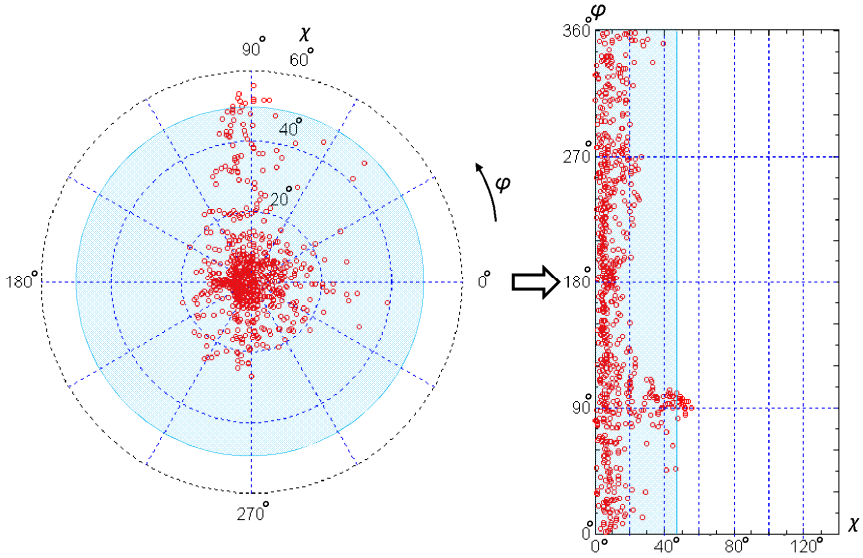

Figure 33 Representation of typical required tilt and rotation with system tilt drive limit. Points outside the blue region require a tilt more than stage range.

4.7.2 Travelling salesman problem (TSP)

Assume a salesman starts from a city and visits each city exactly one time and ends at the original city. The problem is to find the optimized path that takes less time and cost. We use one time visiting each target TSP problem that is slightly modified for the case that the origin is fixed and the path can end at any arbitrary target point without returning back to the origin. Mathematically TSP is a combinatorial problem. The number of possible ways to collect data while the original point is given is (n-1)!. In a case of typical target number like 700 it will be a very large number. Consider that 170! = $7.26\times10^{+306}$. Thus an algorithm for finding the shortest time without checking all possible paths is required for the large number of target points. There are several approaches to this kind of difficult problems such as the ant colony algorithm (ACA) or genetic algorithm (GA) [48].

4.7.3 Result of genetic algorithm optimization

Figure 34b represents initial TSP tour generated by connecting the targets with target number.

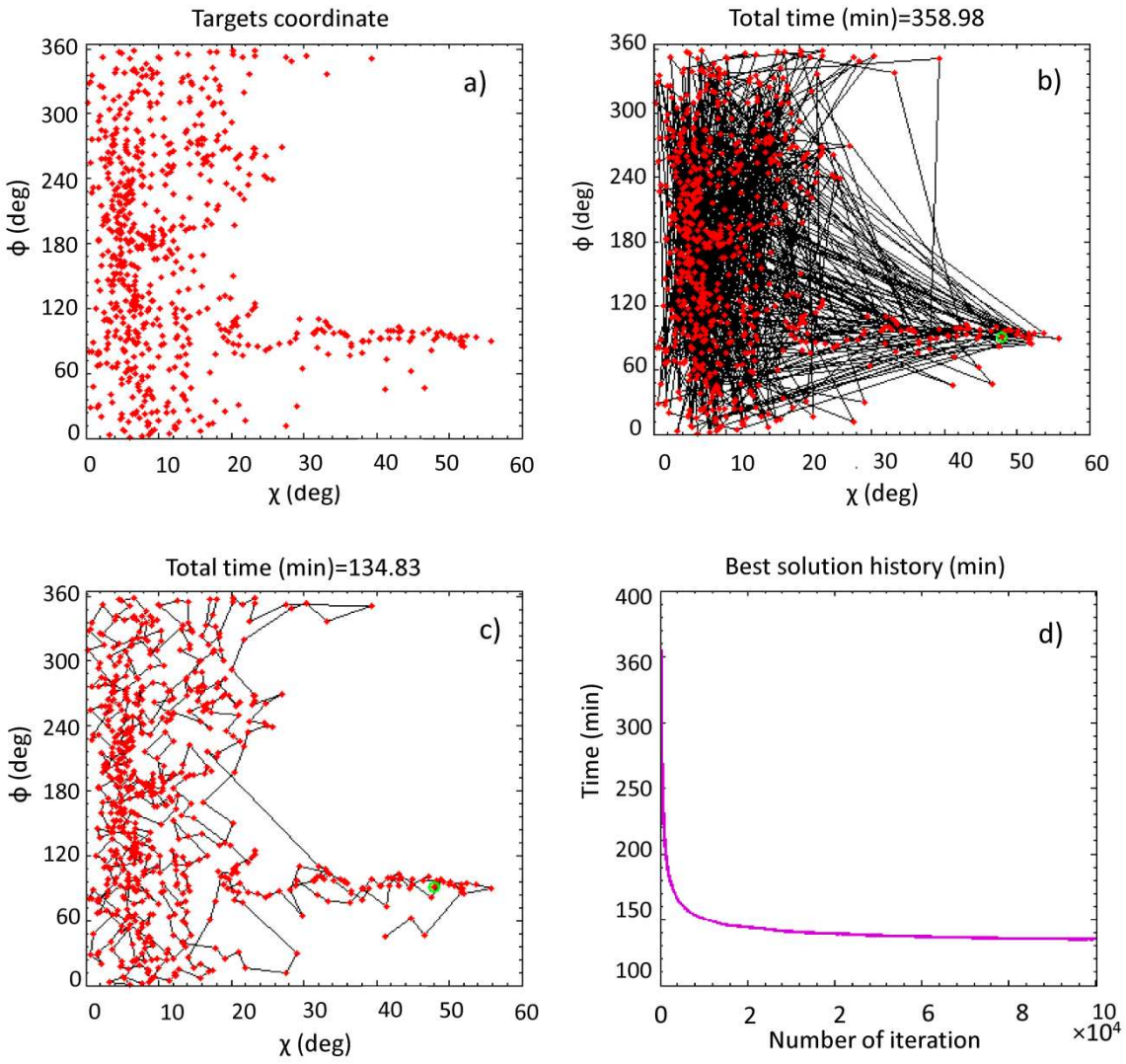

Figure 34 a) targets coordinates b) initial tour generated by connecting the points by their number c) optimized TSP path generated by genetic algorithm d) best solution history vs. number of iterations.

It is clear that targets are not connected adequately in φ and χ space and are not actually optimal. Reconnecting the targets we could generate a shorter path that decrease the required time. Based on this idea a Matlab code for genetic algorithm was implemented. First using a 700×2 tilt and rotation data matrix and speed of the drivers a 700×700 path cost (time in this case) was generated and used for input values for the program**.** Figure 34c demonstrates that GA generated optimal path. Although this is not the absolute minimum answer, but could be one of the best answers that we can achieve. As shown in Figure 34d the required time for the tilt and rotation between the exposures has decreased from 6 hours to 2 hours and 15 minutes, means 37.5% of initial time. Considering that there is a dead time (10.15 s) before each adjustment, the initial time that can be optimized is around 4 hours which is decreased after optimization to 16 minutes. This means a remarkable result around 7% of initial time.

4.8 Results and discussion

4.8.1 Analysis of diffraction data

X-ray diffraction frames collected by this method, were in a proprietary Bruker "gfrm" format which can be opened directly in Bruker's GADDS software. Typical 2D frames are shown in Figure 35 a and b. Frame "a" has both a (-111) monoclinic phase peak and a (101) tetragonal phase peak while frame "b" only has the tetragonal peak. Peaks were

identified according to 01-070-4426 (Monoclinic Zirconium Yttrium) and 01-089-9066 (Tetragonal Zirconium Yttrium Oxide) ICDD (International Center for Diffraction Data) phase identification cards.

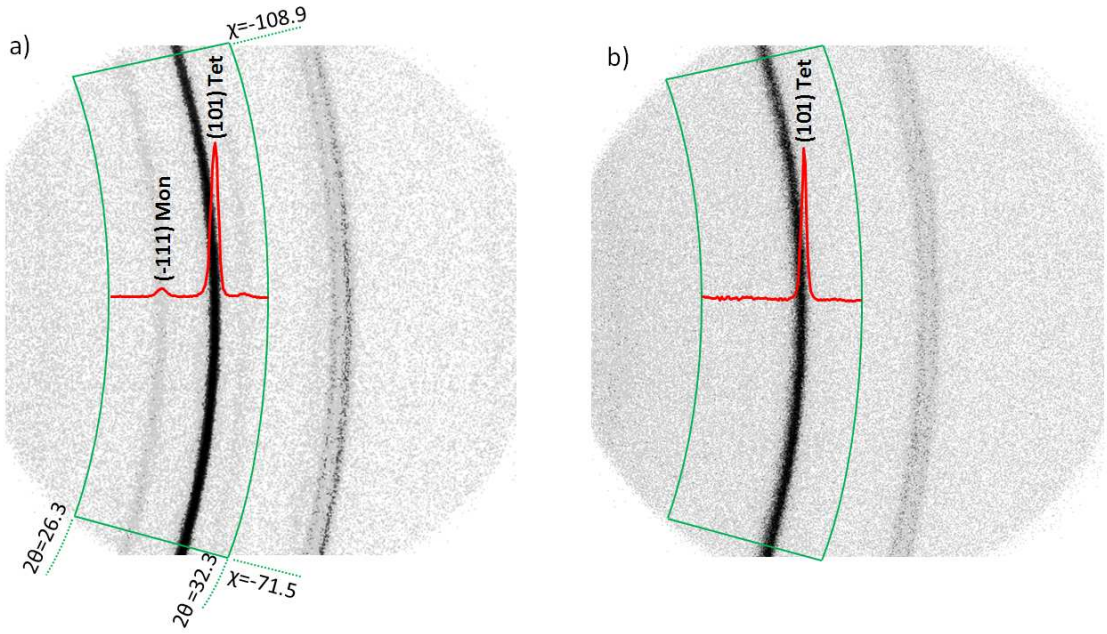

Figure 35 a) Typical frame from the location that has both tetragonal and stress induced monoclinic phases. b) Typical frame related to the location on the crown which has only the tetragonal phase.

A script file was used to integrate the diffraction rings at an angular range of $-71.5 \leq \chi \leq -108.9$ and $26.3 \leq 2\theta \leq 32.3$ for all 700 frames using GADDS software. Integrated results were imported to the Matlab workspace for base line and peak fitting. A 30% Gaussian-70% Lorentzian function was selected for peak fitting and initial values were estimated from parameters provided from peak fitting on a typical data by OriginPro7 software.

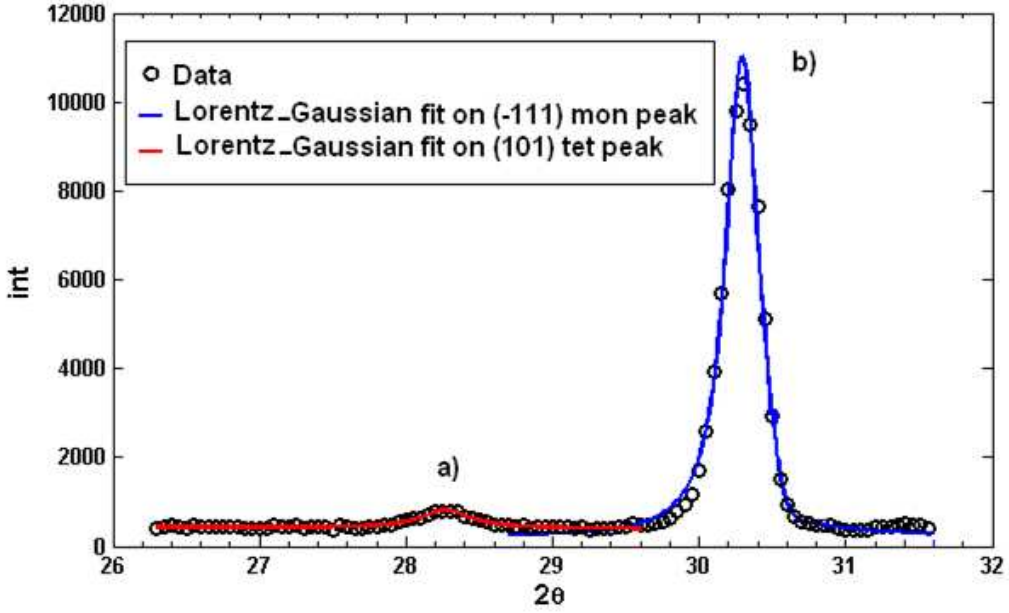

Figure 36 XRD pattern for the selected region that potentially involves both major tetragonal (101) and monoclinic (-111) phase peaks, a) Lorentzian fit on monoclinic related peak, b) Lorentzian-Gaussian fit on tetragonal related peak.

4.8.2 Monoclinic to tetragonal phase ratio for zirconia sample

Pure tetragonal zirconia is not a stable phase at room temperature, but the addition of 3% Yittria maintains the tetragonal structure during initial cooling. Appealing esthetics, chemical inertness, and biocompatibility of yttria-stabilized zirconia, in addition to is high toughness, makes this ceramic one of the most demanded dental restoration materials [1,2]. A crack tip arresting mechanism by stress-induced tetragonal-to-monoclinic phase transformation in the vicinity of propagating cracks for yttria-stabilized zirconia is thought to cause increased fracture toughness [3,4]. Catastrophic fatigue

cracking limits the lifetime of zirconia based crowns covered by porcelain [49,50]. Chipping and crack propagation in porcelain or along the interface at the porcelain side is one of the most common failure modes in the system. Due to the residual stress from the cooling process, the tetragonal structure may partially transform to the monoclinic in bilayer system of zirconia and porcelain. This stress induced phase transformation is attributed to thermal expansion mismatch between porcelain and zirconia. Current results indicate that even in the absence of porcelain, sintered tetragonal crowns may partially transform to monoclinic. Dental ceramics are produced by high temperature sintering of a compact powder which is machined to the desired shape, to achieve a fully dense crown. Due to geometry complexity of the crown, the cooling rate of the ceramic might not be uniform all over the crown causing inhomogeneous shrinkage. Depending on size and local geometry, this non uniform shrinkage results in local compression or tension residual stress. When stress reached to the critical level tetragonal zironia system might relax some part of the residual stress by phase transformation to the monoclinic structure. Figure 37b illustrates a map of the ratio of a monoclinic peak (-111) to the tetragonal peak (101). Comparing height projection of the crown in Figure 37a, and the phase ratio map in Figure 37b, the largest values for this phase transformation were observed at crown's geometric local maximums. In spite of the fact that there are localized variations a correlation between the height of the measured point and phase ratio exists, as is shown in a scatter plot (Figure 37c). For better visualization, the monoclinic to tetragonal phase ratio is superimposed to the 3D geometry and illustrated in Figure 37d.

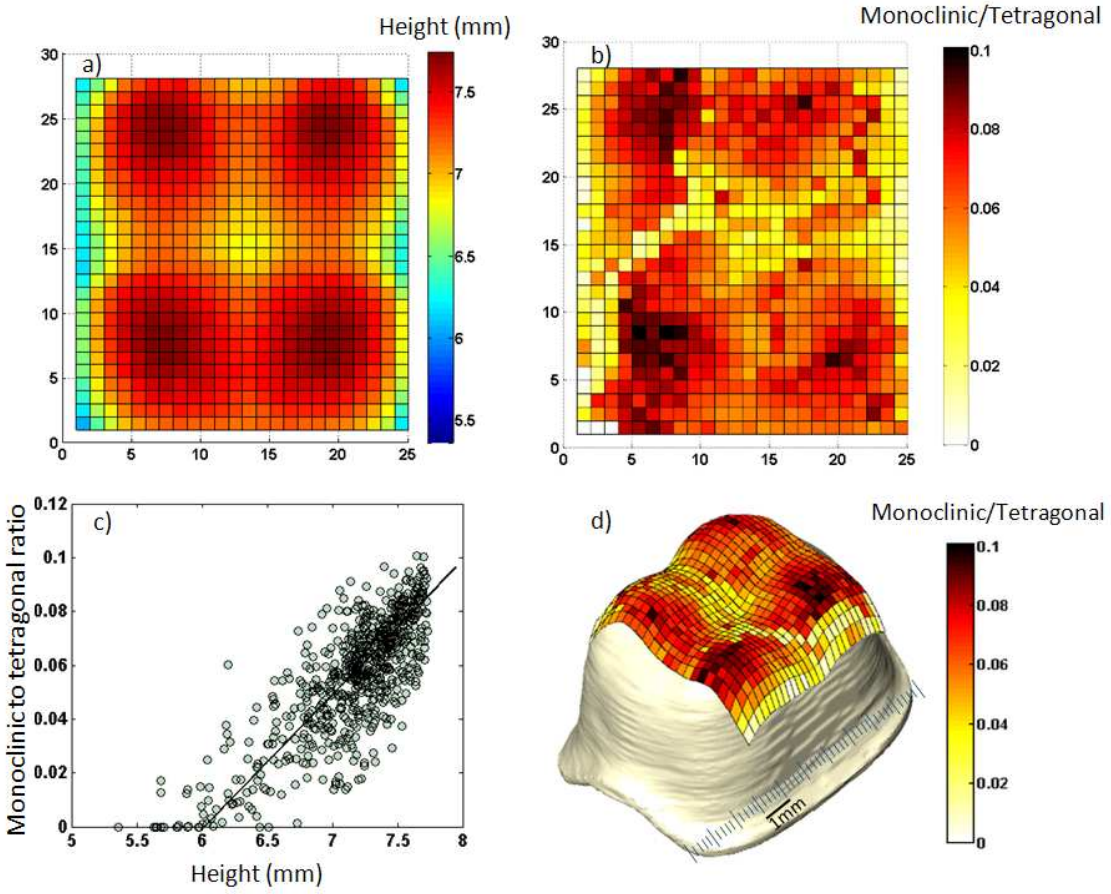

Figure 37 a) Height or geometry projection in xy plane. b) Map of monoclinic peak to tetragonal peak ratio. c) Scatter plot. d) Phase ratio map overlaid on 3D geometry.

4.9 Conclusion

A new approach for characterizing curved surface properties using micro X-ray diffraction was developed. Frames were collected automatically point by point in a single scan set up on rectangular grid projected on the curved surface. The algorithm first utilizes a video laser alignment system to measure the geometry. Points heights obtained appropriately overlay on the tomography geometry, validating the method. A program was developed to determine the normal to the surface at each measurement position.

Based on each normal, a proper local tilt and rotation angle was determined and repeated for all points. Results feed to a script formatted for the system control software. This method was tested experimentally for data collection on a typical dental crown as a complex curved surface. In a single scanning process, 700 frames were successfully collected. Results from analyzed patterns provide phase ratio mapping superimposed to the actual geometry. A correlation between tetragonal to monoclinic phase transformation and height of the local position was observed. This method is general and relevant to other material systems where geometry is complex.

CHAPTER V

5 Residual Stress Delaying Phase Transformation in Y-TZP Bio-restorations

Engineering the residual stress at the complex geometry of bi-layer porcelain -zirconia crown prevents crack initiation and improves the mechanical performance and lifetime of dental restoration. In addition to external load, the stress field depends on initial residual stress before loading. Residual stress is the result of factors such as the thermal expansion mismatch of layers and compliance anisotropy of zirconia grains in the process of sintering and cooling. Stress induced phase transformation in zirconia extensively relaxes the residual stress and changes the stress state. The objective of this study is to investigate the coupling between tetragonal to monoclinic phase transformations and residual stress. Residual stress, on the surface of the sectioned single load to failure crown, at 23 points starting from the tetragonal reach position and ending at monoclinic reach location were measured using the micro X-ray diffraction $\sin^2\psi$ method. An important observation is the significant range in measured residual stress from a compressive stress of -400 MPa up to tensile stress of 400 MPa and up to 100% tetragonal to monoclinic phase transformation.

5.1 Introduction

There is a growing interest for all ceramics restorations as replacement for metal alloys [1,51,52]. All-ceramic restorations have both the required high strength mechanical properties and appealing esthetics. However, they often fail early and unexpectedly, typically within the first 5 years of service [53,54]. Fatigue tests on a modified Y-TZP core, designed with reduced height of the proximal walls and occlusal surface, reveals improved all-ceramic crown reliability [55]. There are several other design factors that can be changed. Further optimization is achievable through understanding and engineering residual stresses. For example, accounting for stresses from phase transformations, base-veneer layer thicknesses [39,56], and the manufacturing process [57]. All ceramic restorations in modern dentistry are mostly made of machined alumina or zirconia cores veneered with porcelain to the required shape before heat a treatment process. Sintering involves firing the two layered structure at a temperature that the veneer fuses to the core. In zirconia-porcelain restorations, sintering the zircoina layer joins grains strongly and reduces porosity. This densification occurs by atomic diffusion in the solid state phase. On the other hand, sintering of porcelain is achieved by formation of a large volume fraction of liquid phase in which matter transport occurs mainly by viscous flow. The viscous flow remains as an amorphous glass after cooling. Crowns fabricated by this method aim for favorable high toughness and crack resistance of zirconia and appealing esthetics and biocompatibility of porcelain. Although the porcelain composition can be customized to reduce its thermal expansion coefficient mismatch with zirconia [58,59] even with the metal bases [60] or by implementing a

graded material [61], generally there is a residual stress at the interface of the two layers [62] and other critical locations of the complex geometry crown. This residual stress creation is avoidable, but requires some changes to the current procedure. Since the thermal expansion of components are a function of temperature and cooling rates and there are multiple firing processes involved, including a finite element analysis based method [63,47,28] and analytical modeling [27] are necessary. High energy synchrotron beam radiation has been implemented to measure residual stress tensors in ziconia core crowns using polychromatic Laue micro diffraction [40,64] and biaxial residual stresses were measured using the $\sin^2\psi$ method with monochromatic micro X-ray diffraction [62]. Laboratory micro X-ray diffraction is a well established technique and has been utilized widely for industrial application [65,66]. Stress measurements using X-ray diffraction techniques are generally limited to crystalline materials, but they have the advantage of providing simultaneous precise information on stress and phases. In this work, using this advantage of diffraction, the method and results of biaxial residual stress measurement using laboratory micro X-ray diffraction equipped with a two dimensional area detector is presented. In the present chapter, advances in focusing micro X-ray lenses that provide high intensity, point size beams down to a few micrometers diameter, and two dimensional (2D) detectors, accurate motorized XYZ axis stages in a variety of configurations along with a laser video auto z-alignment system were adapted to fulfill the requirement of reasonable measurement time and accuracy.

5.2 Experimental procedure

5.2.1 Material

A typical clinically available ceramic crown made of tetragonal zirconia stabilized by the addition of 3 mol % yttrium oxide (3Y-TZP) core and porcelain veneer was selected for this study. To create a stress induced phase region, the required failure load (500N) was applied to one of the crown caps using a 1.9 mm tungsten carbide ball indenter with a custom load frame [67]. At failure, only the porcelain veneer was chipped off without failure of the supporting zirconia core layer. The impacted crown was sectioned in two halfs by water cooled low speed diamond saw before mounting it on onto an aluminum plate with high strength epoxy glue. Polishing was not implemented to avoid potential damage to the section. Figure 38 a shows an optical image of the crown after it was sectioned into halves. Figure 38 b illustrates a scanning electron microscopy (SEM) image of the zirconia-porcelain interface. Cutting marks left behind by the diamond cutter are visible just on the zirconia side. While in low magnification bonding between porcelain and zirconia appears uninterrupted, a higher magnification image of the interface exposes small micro cracks less than 5 µm running along the interface. Edax element mapping illustrated in Figure 38 d shows the distribution of zirconium element at interface region of zirconia-porcelain.

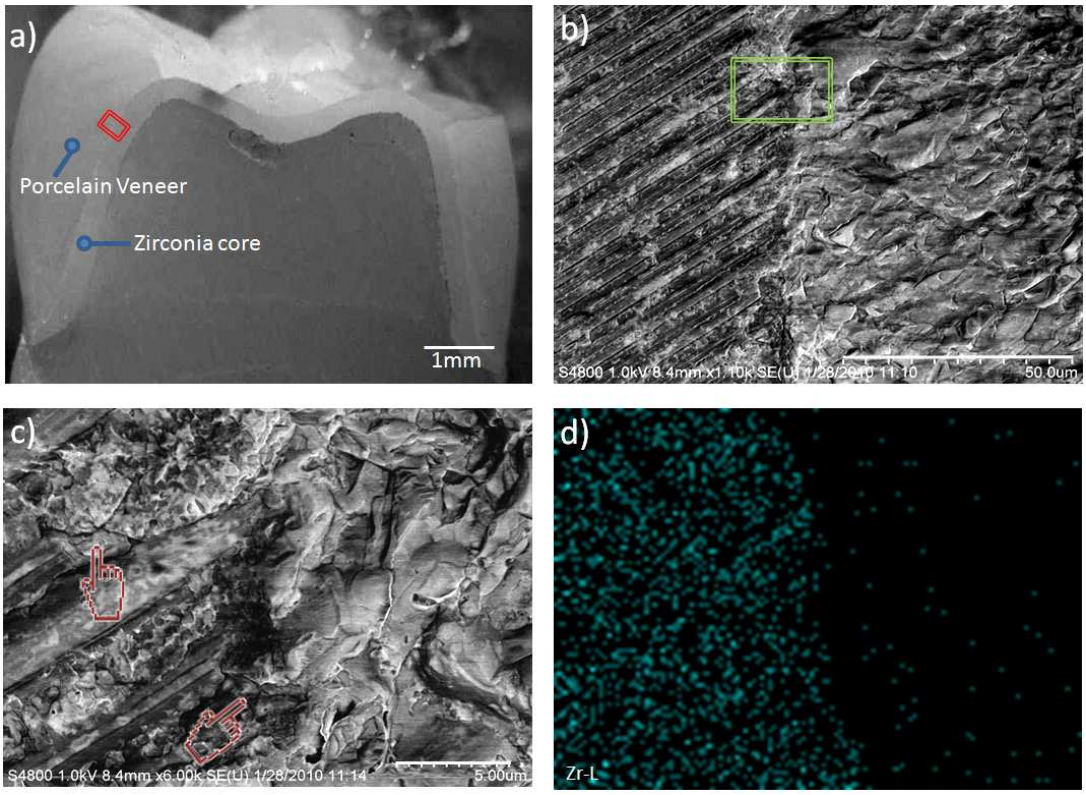

Figure 38 An optical microscope image of sectioned sample. b) SEM micrographs of interface c) zoom image d) Edax element mapping shows the distribution of zirconium element at interface of zirconia and porcelain.

5.2.2 Method

To find the best line for residual stress measurements, initially an X-ray micro-diffraction mapping global search was done using the Bruker D8 Discover XRD2 micro-diffraction system equipped with a Hi-Star 2D area detector and General area Diffraction Detection System (GADDS). The maximum detector distance (299.5mm) by this system was selected because frames collected at higher detector distance have more strain resolution and here peaks were better distinguished although their intensity decreases. At 300 mm the detector simultaneously covers the area of 20° in 2θ and 20° in ψ with a 0.02°

resolution. Two intervals for 2θ at each diffraction point (X, Y) was considered, first a frame from 18° to 38° for phase analysis and then a frame from 63° to 83° interval in high 2θ was selected for $\mathrm{Sin}^2\psi$ bi axial stress measurements.

Mapping X-ray diffraction was performed by collecting 186 frames at 2θ between 18° and 38°, Cu-K_α radiation at tube parameters of 40 kV/40mA, with a 0.1 mm diameter collimator, in reflection mode, a fixed X-ray beam incident angle (θ_1=14°), a detector angle of θ_2=14°, with 120s/frame exposure times, and 100µm separation step in both X and Y translation stage directions. Residual stress for a selected line were measured by the same system at 23 points along a line scan using a mono capillary with a 50 µm diameter focused micro X-ray beam along the line which connects two side of zirconia layer.

5.2.3 Peak selection for residual stress measurement

Since there is a larger peak shift $\boldsymbol{\Delta(2\theta)°}$, and less chance of a displacement error for higher$\boldsymbol{2\theta}$, it is appropriate to find a peak at high $\boldsymbol{2\theta}$ angles. The selected peak is better to have sufficient intensity and be separated from other peaks. Figure 39a shows the typical whole labeled XRD pattern of stabilized zirconia and a selected high 2θ angle (004) ring for residual stress measurements. Figure 39b illustrates that a frame's background intensity decreases at high 2θ angles, which improves the signal gain. Using Bragg's law for $\lambda = 1.54178\text{Å}$ and given $\theta_0 = 73.065$ and 004 ring,

$$\frac{1}{d_{\mathrm{hkl}}^2} = \frac{h^2 + k^2}{a^2} + \frac{l^2}{c^2} \rightarrow \frac{1}{d_{004}^2} = \frac{0^2 + 0^2}{3.60670^2} + \frac{4^2}{5.18020^2} \rightarrow d_{004} = 1.2951\text{Å} \qquad \textbf{5-1}$$

The peak shift is expressed in degrees [68],

$$\Delta(2\theta)^\circ = -2\frac{180}{\pi}\frac{1+\nu}{E}\sigma_\phi tan\theta\, sin^2(\psi) \Longrightarrow \sigma_\phi = \frac{^\circ\Delta(2\theta)\pi}{-360 tan\theta sin^2(\psi)}\frac{E}{1+\nu} \quad \textbf{5-2}$$

For given maximum sensitivity 0.01° (System limit to accurately position the angles), E=205 MPa, ν =0.22, minimum σ_ϕ as a function of 2θ and ψ can be obtained. For a typical 2θ=146.13° and ψ=12°, a residual stress with magnitude of ±1 MPa is measurable.

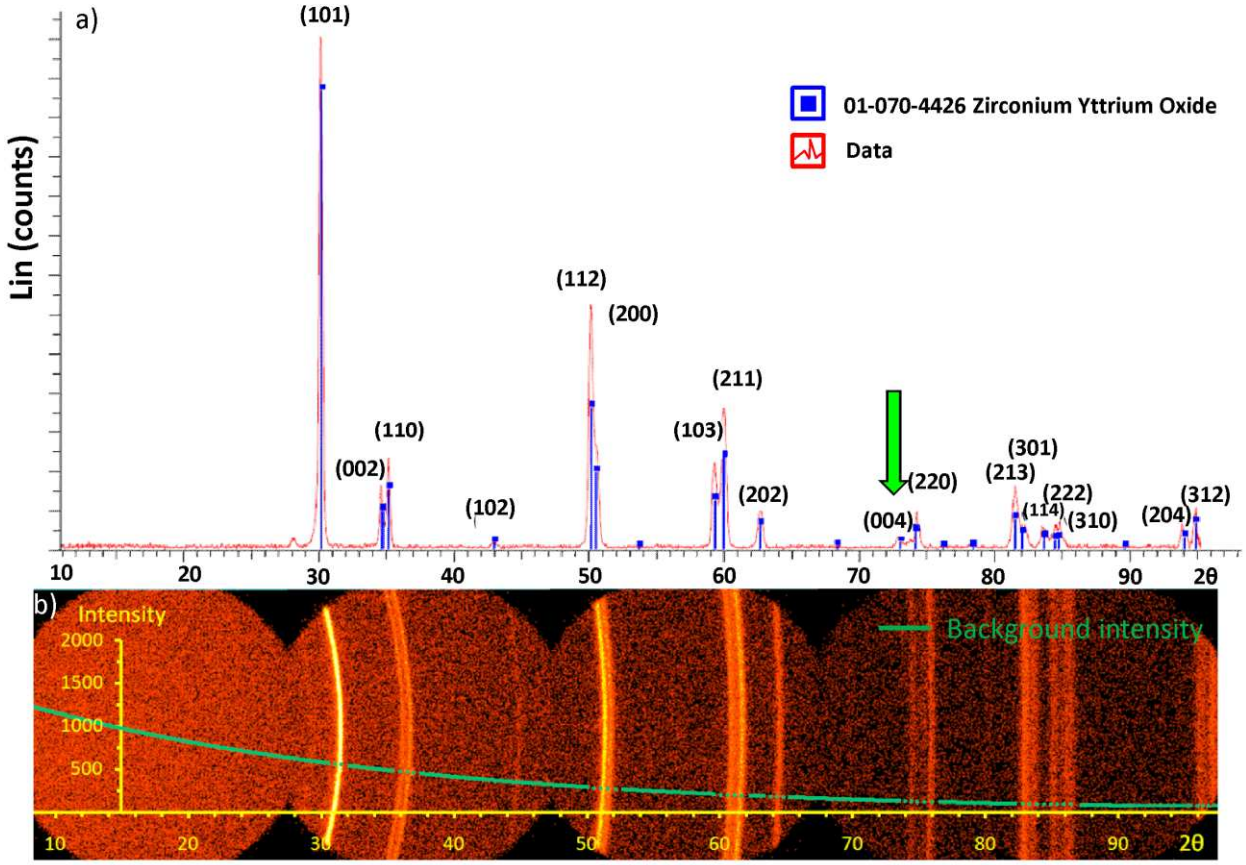

Figure 39 a) X-ray diffraction pattern of tetragonal zirconia and selected (004) peak b) background intensity decreases vs. 2θ.

5.2.4 Choosing an appropriate time per frame

As all XRD stress measurement methods are based on peak location shifts, determining the exact peak position is an important step and requires adequate peak fitting. A proper peak fitting requires high quality data. Collecting the frames at high 2θ angle with a 50 µm collimator by a laboratory X-ray system requires long time exposure on the order of an hour per frame because the total intensity that reaches by detector is as low as 25 counts per second. Collecting several numbers of frames requires finding a reasonable time per frame. A set of frames with times from 1 minute to 120 minutes were collected. Results frame and selected integrated region are illustrated in Figure 40a and b respectively. A Matlab code was developed to fit a combination of two Pearson VII functions [69] on (004) and (220) peaks as shown in Figure 40c. The curve y(2θ) is the intensity as a function of angular position 2θ that we want to fit on measured intensity I(2θ) around the (004) and (200) peaks. Because the (004) and (200) peaks overlap, a combination of two functions each represent one of the peaks.

$$y\,(2\theta) = \mathrm{A}_1 f_1(2\theta - 2\theta_1) + \mathrm{A}_2 f_2(2\theta - 2\theta_2) \qquad \textbf{5-3}$$

Where, A_1, A_2, θ_1 and θ_2 are intensity of fitted peaks and angular position of fitted peaks centers, respectively.

$$f_i\,(2\theta - 2\theta_{\mathrm{i}}) = [1 + K_{\mathrm{i}}^2(2\theta - 2\theta_{\mathrm{i}})^2]^{-M\mathrm{i}} \qquad \textbf{5-4}$$

Where K_{i} determines the width of the fitted curve and Mi governs the rate of decay of the tails. For $M_{\mathrm{i}} = 1$, the profile is purely Cauchy, for $M_{\mathrm{i}} = 2$, a Lorentzian function, and for M_{i} =infinity, the profile is purely Gaussian.

Although increasing the exposure time per frame provides reasonably less noisy data, there is an experimental upper limit for collection time after which the ratio of the signal to noise remains constant. The Mean Square Error (MSE) of the data from the fitted curves that represents the signal to noise ratio is plotted in Figure 41, and based on that, a 45 minute exposure was selected per frame.

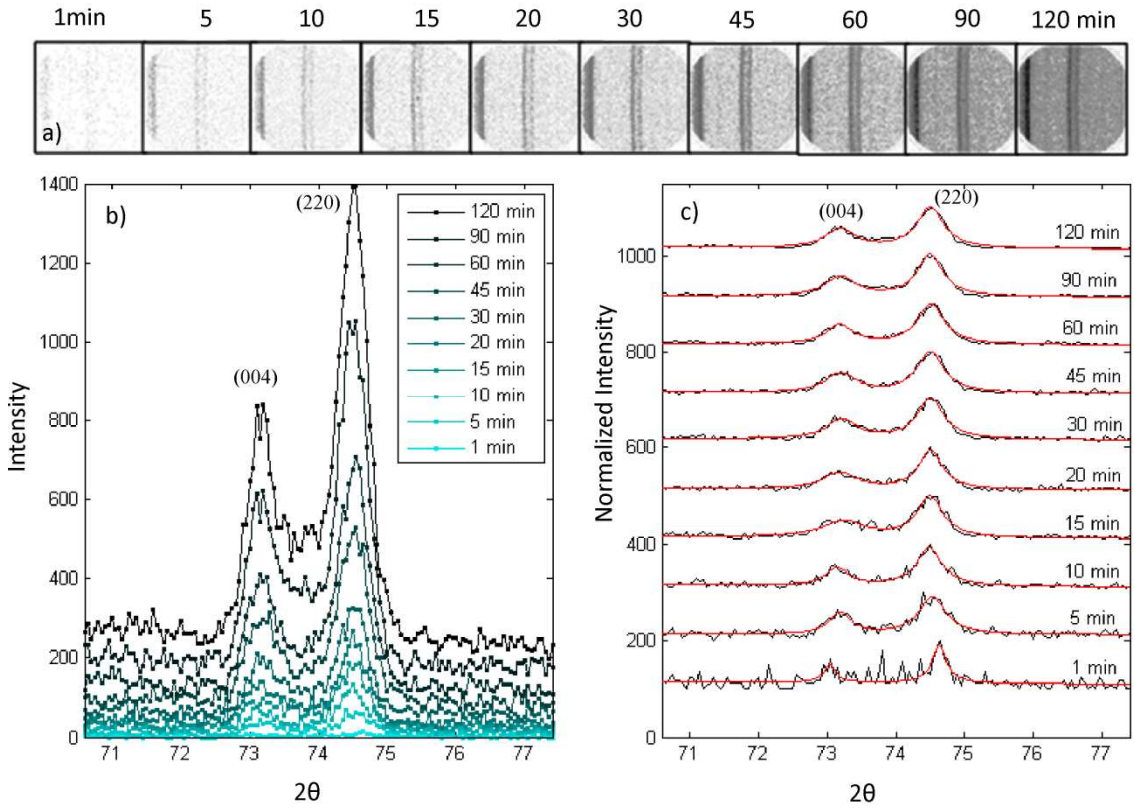

Figure 40 a) frames with various times b) integrated pattern c) normalized and fitted peaks by two Pearson VII functions.

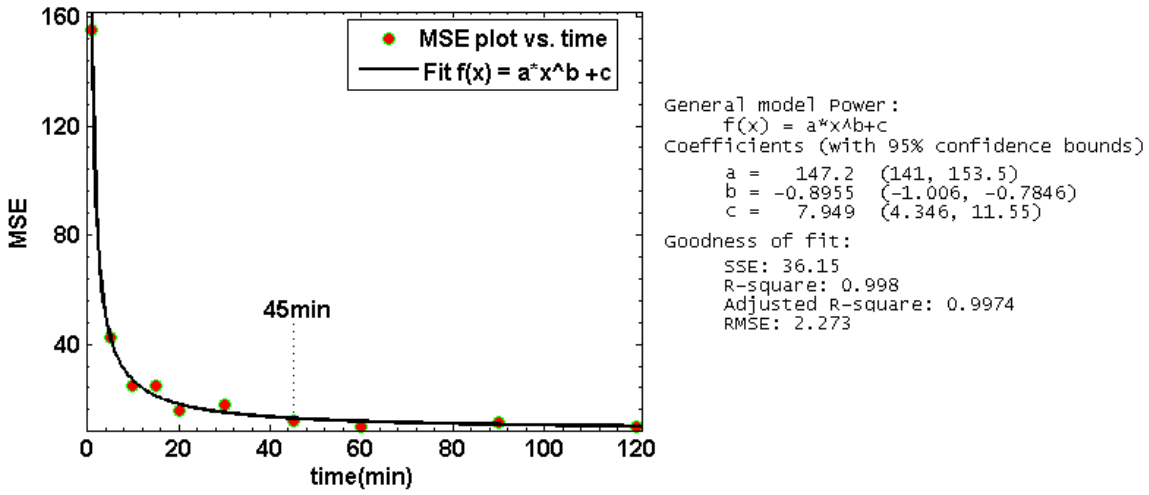

Figure 41 square error of curve fits on (004) and (220) peaks saturates by 45 min.

5.3 Results and discussion

Since the main objective of this experiment is to investigate the relation between the stress state and the degree of tetragonal to monoclinic phase transformation in zirconia, finding the line between two points on the complex cracked geometry of crown that starts from tetragonal phase and ends in monoclinic phase is critical. The area suspected to have stress induced phase transformation was mapped to find the best line for residual stress measurement, shown in Figure 42a. The areas under 3 monoclinic related peaks were normalized to the maximum area for all collected frames, illustrated in Figure 42b. To validate this map, the area under a normalized tetragonal peak is mapped in Figure 42c. From both maps the best location with the desired property of monoclinic phase in one side and tetragonal on the other side across the thickness of zirconia layer is apparent. Without the map, it would be difficult to find such a path, as the tetragonal phase may just partially transform to monoclinic under the impact load.

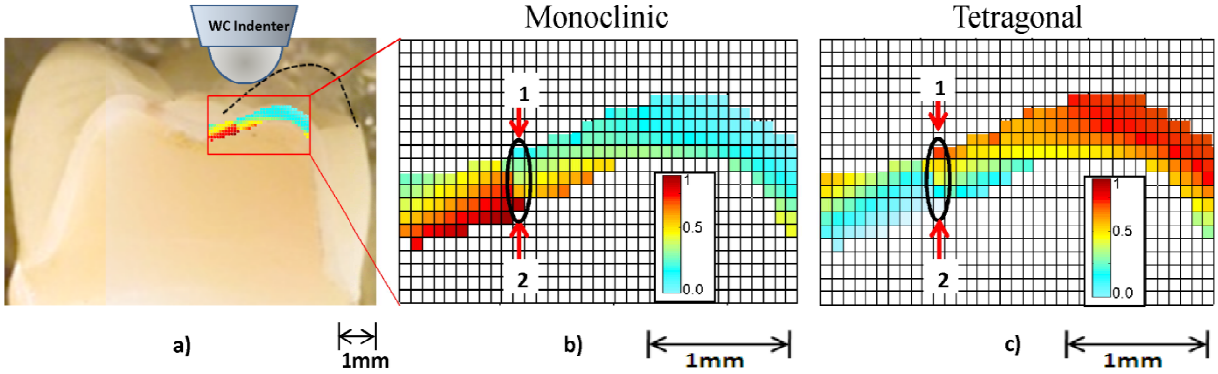

Figure 42 a) Optical microscope photo of a sectioned failed crown. The box outlines the location of the X-ray map, b) High resolution X-ray diffraction map of the total area under (011,110, and 101) monoclinic peaks c) Map of the area under the (101) tetragonal peak.

Along the line that connects the two sides of the zirconia layer, 23 points were selected for a line scan using a 50 μm mono capillary optic (also indicated in Figure 49a). Two intervals for 2θ at each point were considered, one frame from 18° to 38° and a frame from 63° to 83°. Frames at the first interval were collected for phase analysis, because at this interval both monoclinic and tetragonal peaks are bright and have enough separation. The second interval at high 2θ was selected for $Sin^2\psi$ stress measurements.

The frame in Figure 43a shows only the tetragonal crystal structure while Figure 43b shows just the monoclinic structure corresponding to the point 1 and 23, labeled on Figure 49b. Frames collected in between the pure tetragonal and monoclinic phases, were integrated to yield intensity versus 2θ diagrams. Diffraction patterns across the selected line for all measurement points (illustrated in Figure 43a), reveal a gradual phase transition. Similarly, the tetragonal to monoclinic phase transition is confirmed at high 2θ frames (shown in Figure 44c).

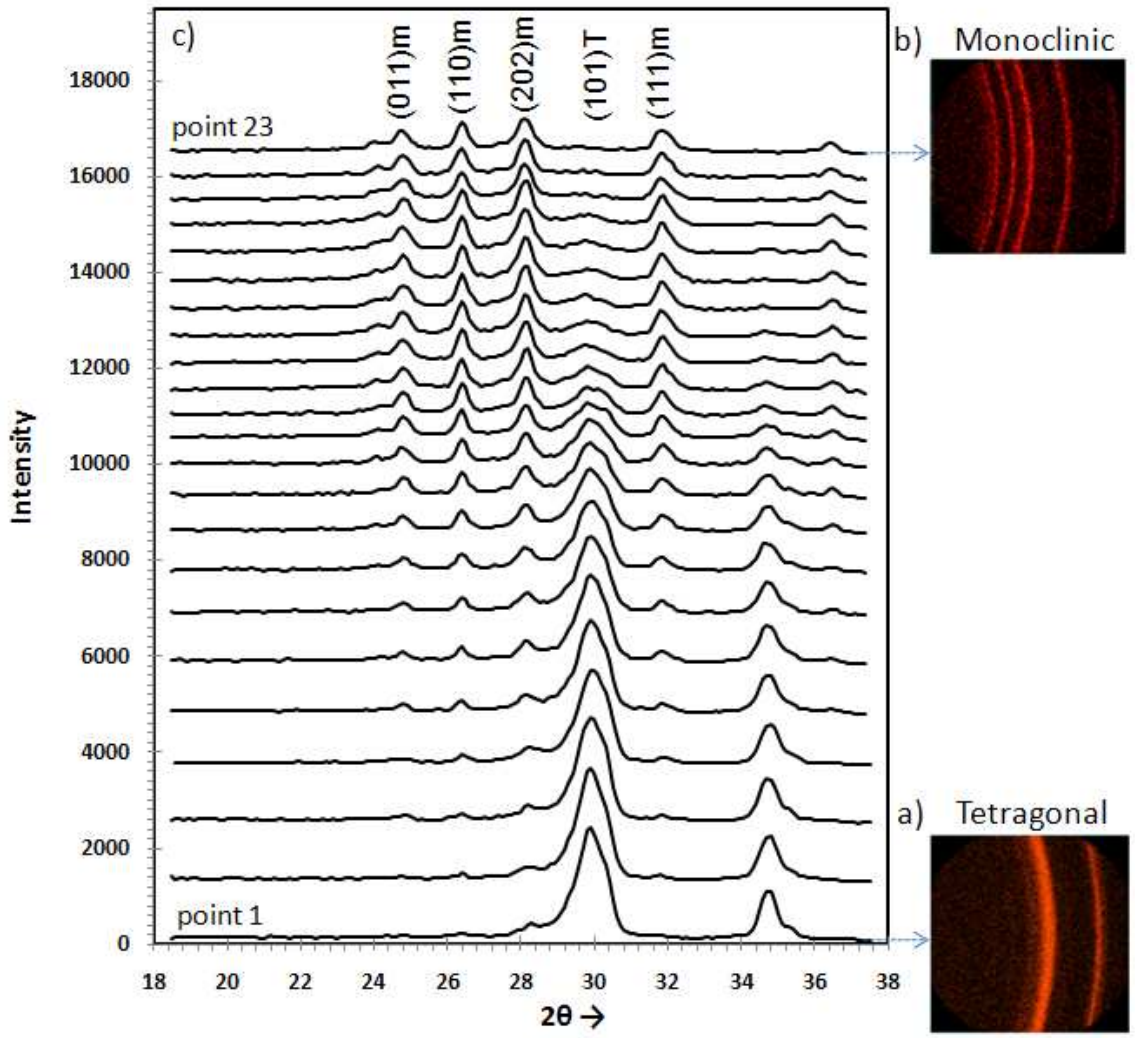

Figure 43 a) Tetragonal 2-D diffraction image (2θ=18° to 38°). b) Monoclinic 2-D diffraction image. c) Integrated rings giving intensity versus 2θ diagrams, starting at the zirconia porcelain interface and proceeding across the zirconia layer.

The mapping process was repeated on a sectioned crown without impact. It did not show monoclinic phase. This suggests that the phase transition discussed above was created by impact damage. The external load created a stress field that finally caused the failure of the veneered layer while the zirconia did not fail but transformed. The gradient of

phase transformation from zero to 100 percent that was observed is understood if we consider the role of residual stress.

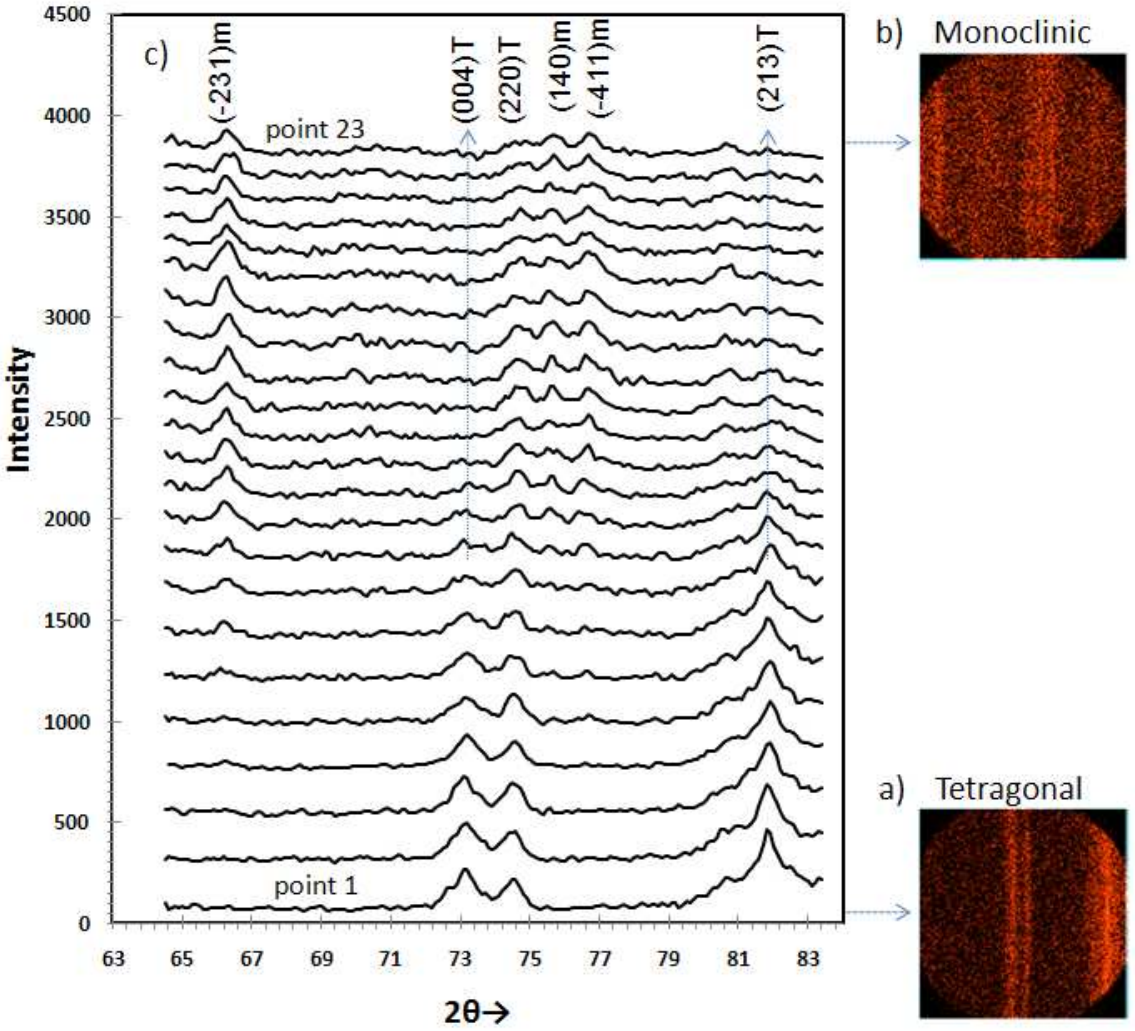

Figure 44 a) Tetragonal 2-D diffraction image (2θ=63° to 83°). b) Monoclinic 2-D diffraction image. c) Intensity versus 2θ diagrams across the thickness, from integrated rings.

In order to measure residual stress at each point, four frames with different sample tilt value were collected to cover 60° of ψ angle. Using a sequential list, the system

automatically located each predetermined point to the instrument center of diffraction using a motorized five axis (X, Y, Z, ψ (tilt), ϕ (rotation)) sample stage. Angles are shown schematically in. Final height adjustments in the Z-direction were made by an auto video-laser system before each data collection.

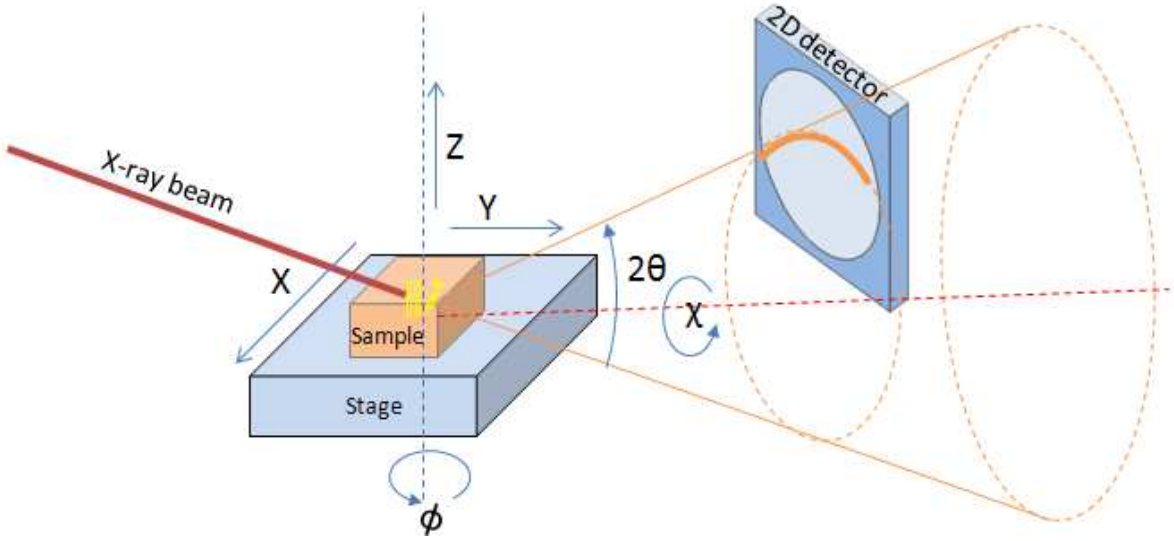

Figure 45 Schematic of the sample orientation and position of the 2d detector with respect to the diffraction cones. χ is the angle subtended by the diffraction rings on the 2D detector.

The applied stress was concentrated in small area underneath the ball indenter tip, a good candidate location for phase and stress analysis is a line scan right under the indenter load. Figure 46 b shows the location of exposure points selected on a line that connects the bottom and top side of the zircona layer. Frames collected from points 1 and 23 illustrated in Figure 46 c and d are substantially different. This difference indicates stress induced change in crystal structure.

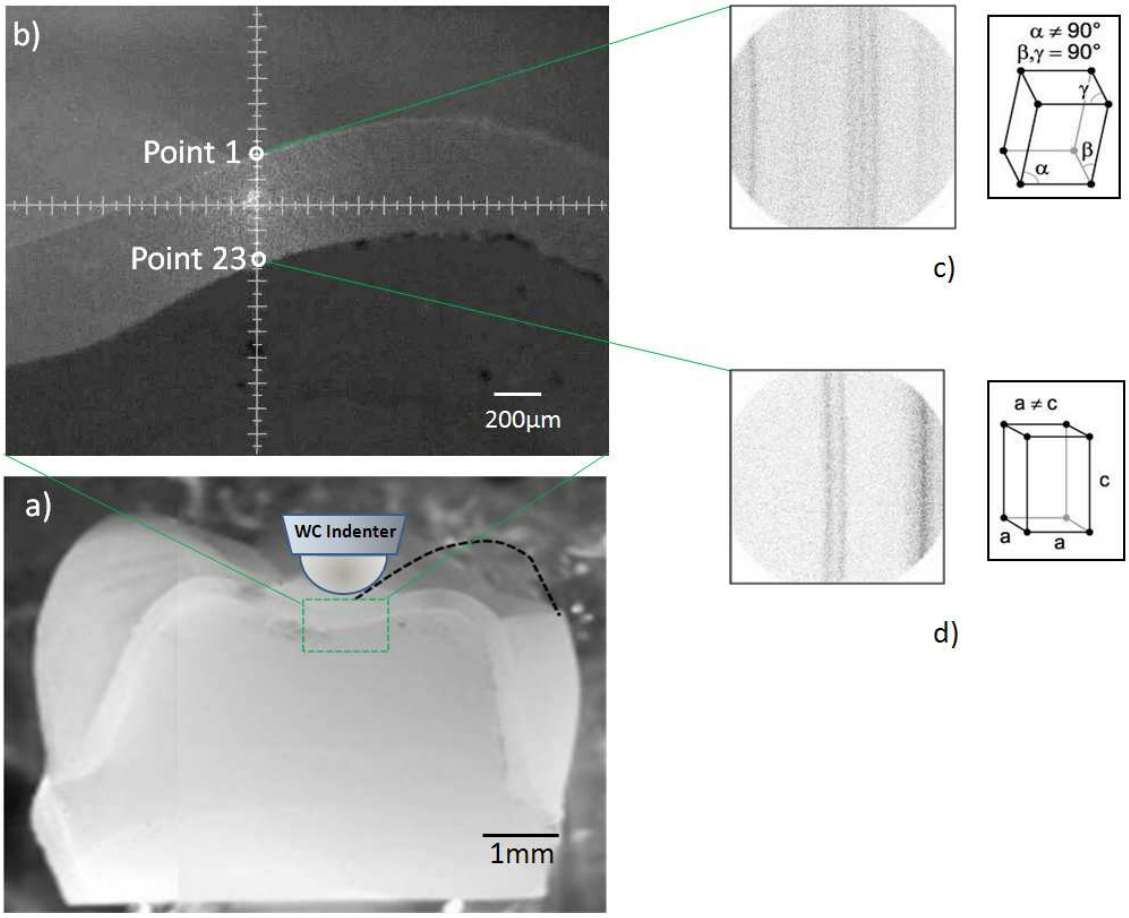

Figure 46 a) An optical microscopy image of the measurement location on the crown b) exposure points, starting at the interface between zirconia and porcelain (point 1) and proceeding across the zirconia layer away from the interface (point 23) c) Monoclinic 2-D diffraction image (2θ=63° to 83°) d) Tetragonal 2-D diffraction image (2θ=63° to 83°).

5.3.1 Observation of phase transformation from X-ray diffraction frames

A mosaic pattern of frames collected along the cross section line that connects the surfaces of the zirconia layer under the indentation point qualitatively reveals phase transformation, as shown Figure 47. Frames collected at locations 1 and 23 have different sets of rings identifying the two different phase of zirconia, but frames at the middle of the length (frame number 12) show both phases.

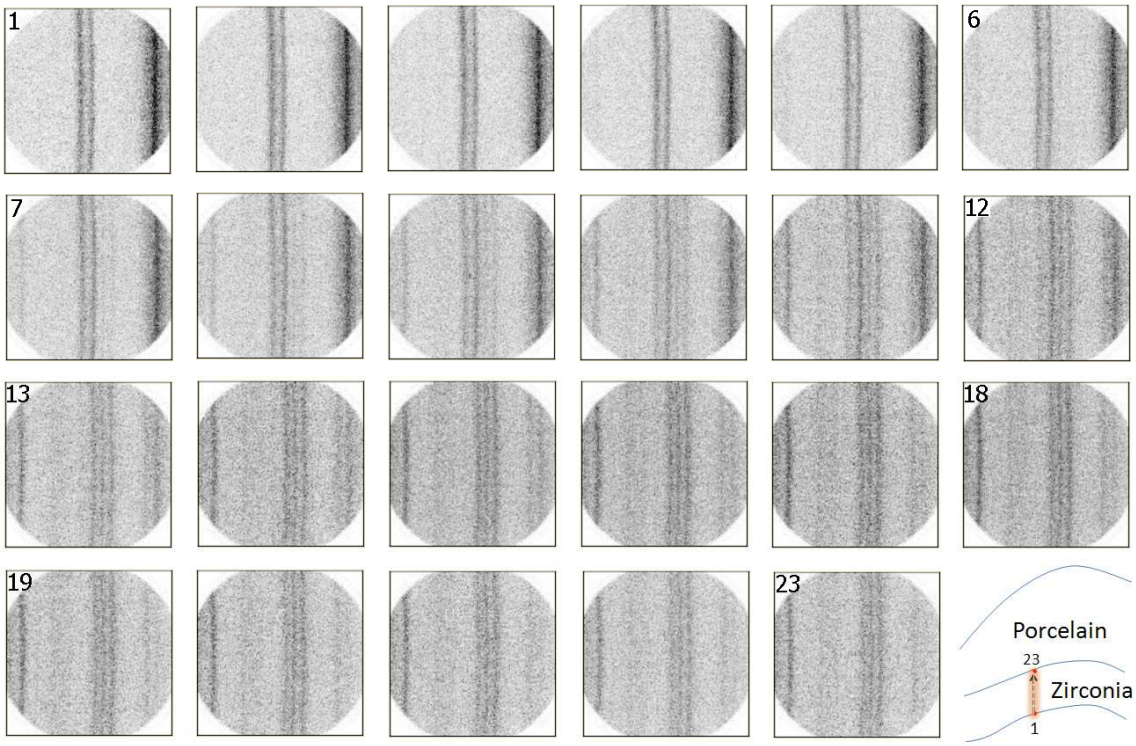

Figure 47 Mosaic pattern of 2D XRD frames along the cross section from the inside surface to the porcelain interface that cover the χ = 0° to 20° segment of diffraction cones.

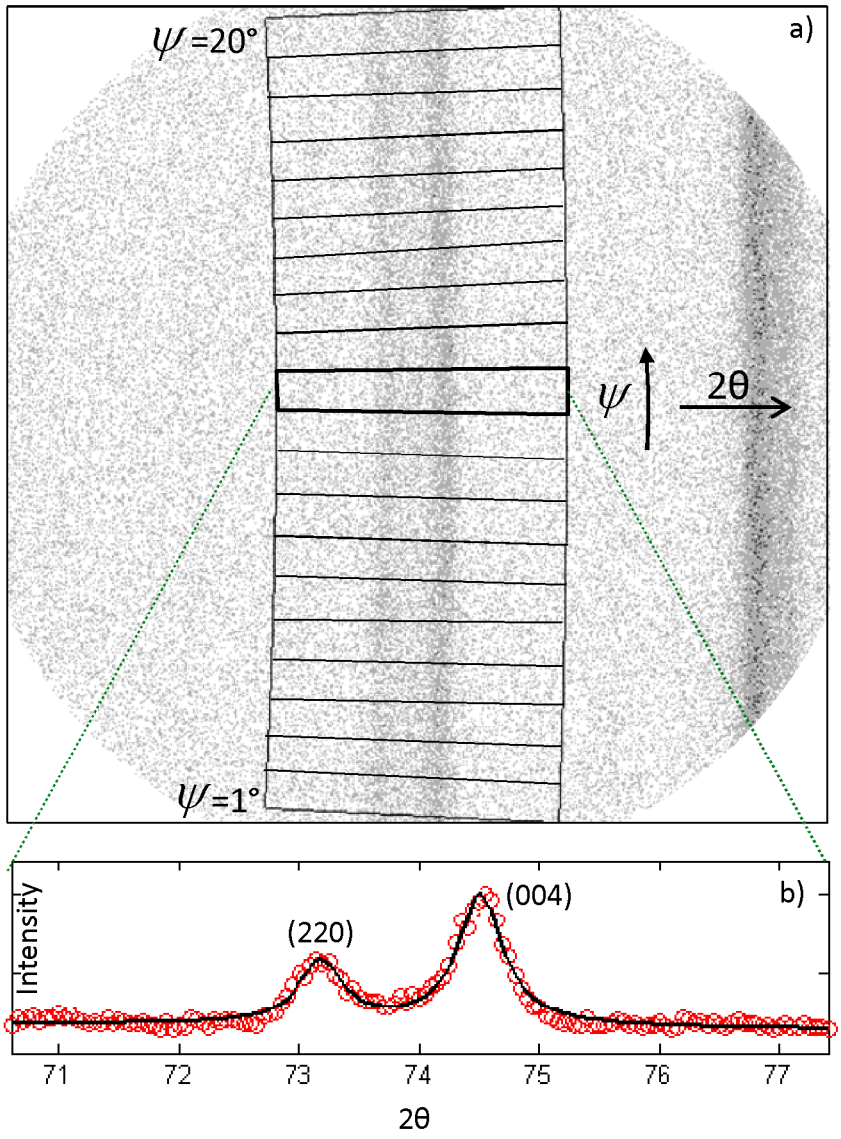

Figure 48 a) Typical segmented diffraction frame. b) Integrated intensity profile, fitted by two Pearson VII functions for a 1° highlighted segment.

Figure 48a, illustrates a typical frame with a segmented region that involves (004) and (220) rings. The integrated intensity for each segment was fitted by two Pearson VII functions using a Matlab program.

The (004) tetragonal zirconia peak at 73.065° and (231) monoclinic zirconia peak were selected for stress calculation using the sin2ψ method. The ψ range was segmented into smaller integration segments of a 1° ψ range. The residual stress for every scan point was evaluated from sin2ψ versus ψ curves using the following equation [68],

$$\sigma_{\phi} = \frac{\text{Slope}}{d_{\psi=0}} \cdot \frac{E}{1+\nu} \qquad 5\text{-}5$$

Based on the slope and the intercept ($d_{\psi=0}$) the residual stresses were determined. It is convenient to use $d_{\psi=0}$ as stress free reference value, which typically leads to an error of only 0.1% [68]. The error bars in measured stresses were determined based on the confidence bound of the peak fitting and variance of seven measurements at each location. The calculated confidence bound corresponds to a 2θ range that itself corresponds to a range in *d*-spacing.

Figure 49b shows combined residual stress measurement results with tetragonal to monoclinic phase transition ratio in percent. The biaxial residual stress was found to range from -400 MPa to 400 MPa for the scanned line. An important point to note is initially at point 1 the stress was -400 MPa (compressive) and gradually increased to +400 MPa (tensile) at point 7, and then dropped to zero (average) after this peak. The gradual changes in the phase transformation ratio with this gradual stress change from compression to tensile, then to zero, revels a residual stress relaxation from phase transformation. This mechanism of phase transformation prevents the zirconia layer from crack growth in its application as a dental material combined with a porcelain veneer. Considering the fact that meta stable tetragonal zirconia transforms to monoclinic due to

tensile stress, and the current observed relation between stress and phase ratio, determines an important role for compressive residual stress at the zirconia layer interface.

Before applying any external load to a typical zirconia-porcelain crown, depending on cooling process, geometry and relative thickness of layers, a residual stresses from -100 MPa to +100 MPa is expected along the thickness of zirconia layer. If the zirconia layer is in compression before applying external tensile load, initially the compressive residual stress might be compensated and only further tensile loading would result in phase transformation. It is here that the meta-stable tetragonal zirconia relaxes the tensile stress by performing phase transformation and likely delays crack initiation. It was observed from Figure 49 that stresses go to zero at about 50% phase transformation. The current measurement was performed in one line scan on a (004) peak and focusing mostly on introducing the technique. As future work, more measurements at other locations of the crown and considering other peaks would be beneficial. However, the technique is powerful and these first results are sufficient to indicate some interesting behavior. The transformation to a majority monoclinic phase 1.5 mm from the interface would also mean communication of stresses from gran-to-grain within this tetragonal phase becomes limited. Thus the stress in the monoclinic phase would dominate in this region. The transformation to monoclinic during impact would have been associated with a volume expansion. Once the driving force from the applied load was released, the residual stress state would have changed.

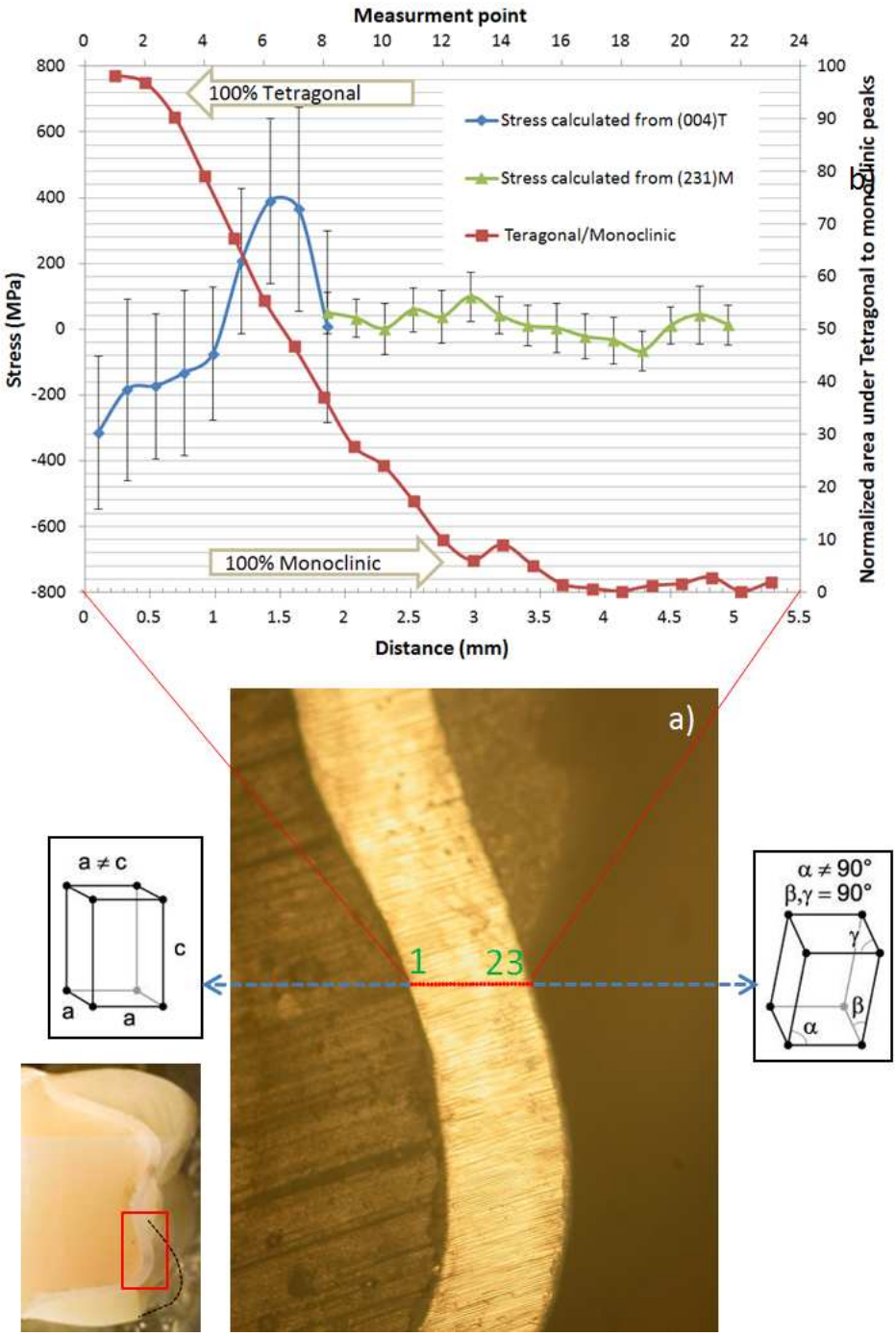

Figure 49 a) 23 exposure points, starting at the interface between zirconia and porcelain (point 1), proceeding across the zirconia layer away from the interface (point 23). b) Combined phase transition and residual stress along the line scan.

It is possible that this volume change is also associated with micro-cracking. Future work could also include microscopic evaluation to observe cracking. That micro-cracking would have limited residual stresses in this part of the sample and supports the current observation of nominally 0 MPa stress beyond 1.8 mm from the interface. Further future work could also include observing the stresses in the direction parallel to the interface. The stresses examined here were aligned primarily perpendicular to the interface. In addition, implementing this method on a specimen fatigued to failure would be clinically relevant.

5.4 Conclusion

The overall state of residual stress is an important factor in failure and lifetime of ceramic dental restorations. Novel crowns could be designed with an understanding of residual stress' critical role. A method of combined phase transformation and residual stress measurement were adapted for dental crown studies. Stabilized tetragonal zirconia, currently a dominant material for dental restoration, is meta-stable and transforms to monoclinic under critical stress. Current results couple phase transformation and residual stress measurement. This is an important factor in design, because this transformation under critical load retards failure. A significant range of residual stress from a compressive stress of -400 MPa up to tensile stress of 400 MPa and up to 100% tetragonal to monoclinic phase transformation were observed for an impacted crown under a single load to failure. Knowledge on phase transformation coupled with residual stress states, layer thickness, and the manufacturing process opens up the keys to designing longer life dental restorations.

CHAPTER VI

6 Three Dimensional X-Ray Diffraction Cone Detection and Visualization

A new method of sensing and analyzing three dimensional X-ray diffraction cones was introduced. Using a 2D area detector, a sequence of frames was collected while moving the detector away from the sample with small equally spaced steps and keeping all other parameters constant. A three-dimensional dataset was created from the subsequent frames. The three-dimensional X-ray diffraction pattern detection (XRD^3) contains far more information than a one-dimensional profile collected with the conventional diffractometer and two-dimensional X-ray diffraction (XRD^2). The present work discusses some fundamentals about XRD^3, such as data collection method, 3D visualization, diffraction data interpretation and potential application of XRD^3 in various diffraction fields.

6.1 Introduction

Exposing photographic films was the first way for detecting diffracted X-rays. An X-ray affects film like visible light. Film designed for X-rays has thicker emulsion than normal photographic film to increase absorption. Film detectors are thin, flexible, and have high resolution and dynamic range, though accuracy can be an issue. Films were replaced by counter detectors in powder X-ray diffraction systems much earlier than replacement of

photography film in digital cameras. A point detector needs only to move step by step on circumference of a circle centered on the powder spacemen to record diffracted intensity as counts per second vs. diffraction angle (2θ). Having Intensity vs. diffraction angle (2θ) is enough to compare the pattern with known spectra. In the past twenty years, due to the advances optics and computing power, remarkable advances have been demonstrated to replace point detectors with two dimensional detectors. In the case of samples with texture, large grain size, or small quantity, the integrated data from a 2D detector has better intensity, resolution, and statistics resulting in better phase identification and quantitative analysis [70]. These same advantages also enable practical use of smaller beam sizes. Two dimensional detectors have been adapted for most of X-ray diffraction techniques. The speed of collecting diffraction data using a 2D detector is typically several orders of magnitude faster that a 1D point or line detector. In the case of phase analysis, 2D diffraction data should be integrated first to 1D intensity versus diffraction angle to be comparable with ICDD cards, but still has remarkable advantage in reduction of data collection time and capability of illustrating spottiness or local texture in a diffraction ring. 2D detectors have been implemented to measure residual stresses with high sensitivity, speed and accuracy since whole or a part of the diffraction ring can be measured simultaneously capturing orthogonal components of the strain [71]. Two dimensional detectors are appropriate for large grain and textured samples and Pole figures can be measured at fine steps for texture analysis [18].Two dimensional detectors are appropriate for large grain and textured samples and Pole figures can be measured at fine steps for texture analysis [72,73]. Recently, Allahkarami *et al*. introduced the idea of

using 2D detectors with proper sample rotation and tilts for diffraction mapping on curved surfaces [74]. Their method relies on avoiding sample shadowing of the detector and is only practical using 2D detectors, especially in case of textured samples. Although the case of phase identification requires integration steps on recorded frames, it gives better intensity and statistics for phase ID and quantitative analysis, particularly for small quantities of a phase [75, 76].

Three-dimensional detection of diffracted X-rays from exposed material is of fundamental importance for many X-ray diffraction techniques and applications [77]. However, accessing the three-dimensional diffracted X-ray data seems practically impossible with laboratory systems. This kind of X-ray detection would benefit from a 3D array of detectors without introducing disturbance or absorption of the X-ray while it is passing though the detector. In addition to the triangulation method useful for detecting grain depth [78], Bunge *et al.* used a sweeping method based on continuous movement of area detector for texture analysis [79]. The idea of 3D detection of X-ray using laboratory scale XRD system was discussed by Bob B He in his book on two dimensional X-ray diffraction [80]. In a chapter on innovation and future development he has introduced concepts of a three-dimensional detector and its potential application. This study demonstrates an efficient way for 3D detection and visualization of X-ray diffraction data. During data collection, a 2D area detector collects frames at different distances from the center of diffraction in a stepwise manner in order to be used as 3D data set. It should be noted that we use the term 3D detection of diffracted X-ray for the technique and not 3D-XRD. The term 3D-XRD already has being used for 3D map of

sample microstructure in three dimension X-ray microscopes, a method to be distinguished from what is introduced here [81].

6.2 Experimental procedure

Polycrystalline Alumina (Nist 1976a) was selected for this study. X-ray diffraction was performed with Cu Kα radiation at tube parameters of 40 kV/40 mA using a Bruker D8 Discover XRD^2 micro-diffractometer equipped with the General Area Diffraction Detection System (GADDS) and a Hi-Star two dimensional area detector. A laser–video Z-alignment system was used for sample alignment. Using the 2D detector, 47 diffraction patterns containing several Bragg peaks from alumina were collected starting with a 70 mm sample to detector distance (SDD) to 300 mm at 5 mm steps. At each step, only the sample to detector distance was increased. All other parameters were kept constant. The experimental set up with the detector at two different positions is shown in Figure 50.

The angle between the detector surface normal vector and the direction of diffracted beam was kept constant. The X-ray beam incident angle θ_1 and detector angle θ_2 were 20°. The exposure time was 60 s/ frame with an 800 µm diameter beam. The detector distance changed manually at each step. System calibration including determining the precise sample to detector distance and beam center, which involves flood field correction and spatial correction were performed [42]. At each distance after calibration, the sample to detector distance was validated with the value on the scale and the detector center verified. The 00-046_1212 ICCD Powder diffraction file was used for peak matching in calibration.

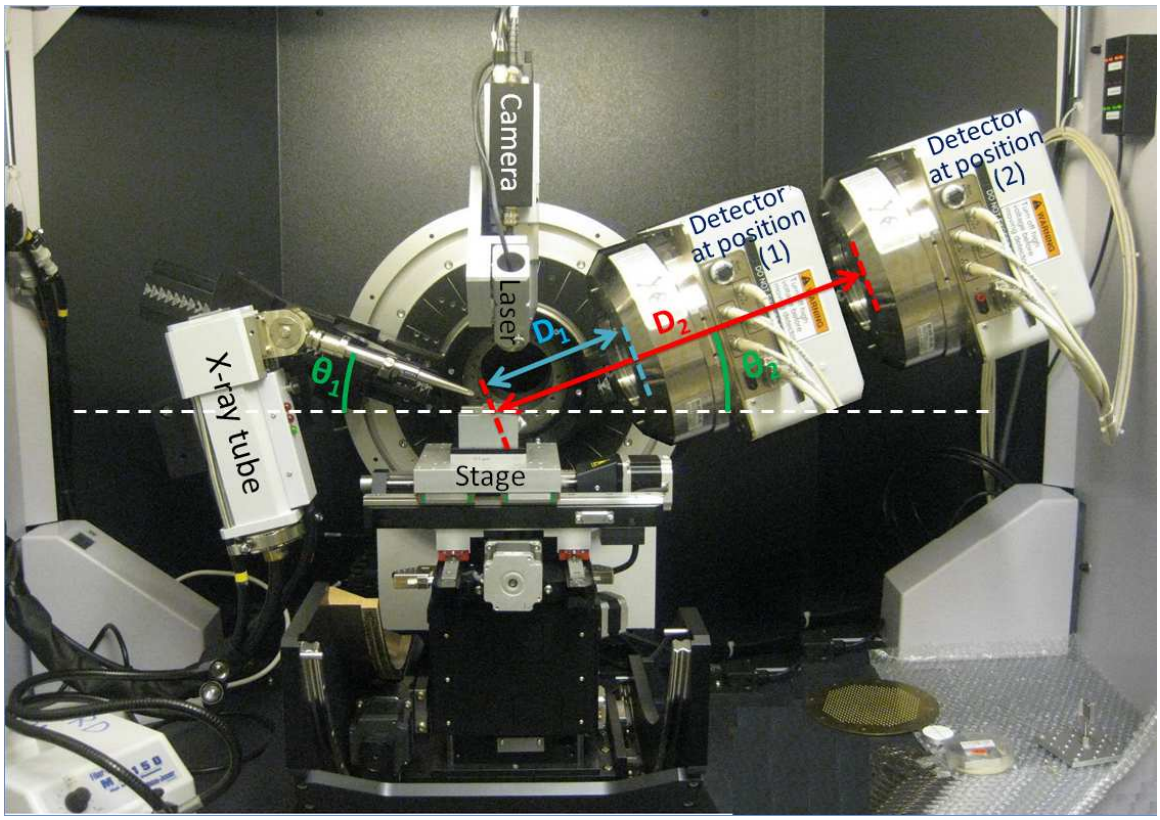

Figure 50 Experimental setup using Bruker D8 discover X-ray diffraction system. A laser camera alignment system was used to position the sample at the focal point of the X-ray beam.

6.3 Results and discussion

Figure 51 shows the comparison between the conventional 1D diffraction pattern, 2D diffraction pattern, and three dimensional detection of a diffraction pattern from the alumina powder. As dimension of the acquired data increases, more information is available for diffraction analysis such as stress analysis, phase identification, particle size and shape and texture [82]. In discussions of diffraction, the word "cone" is taken to mean "double cone," i.e., two cones placed apex to apex.

.

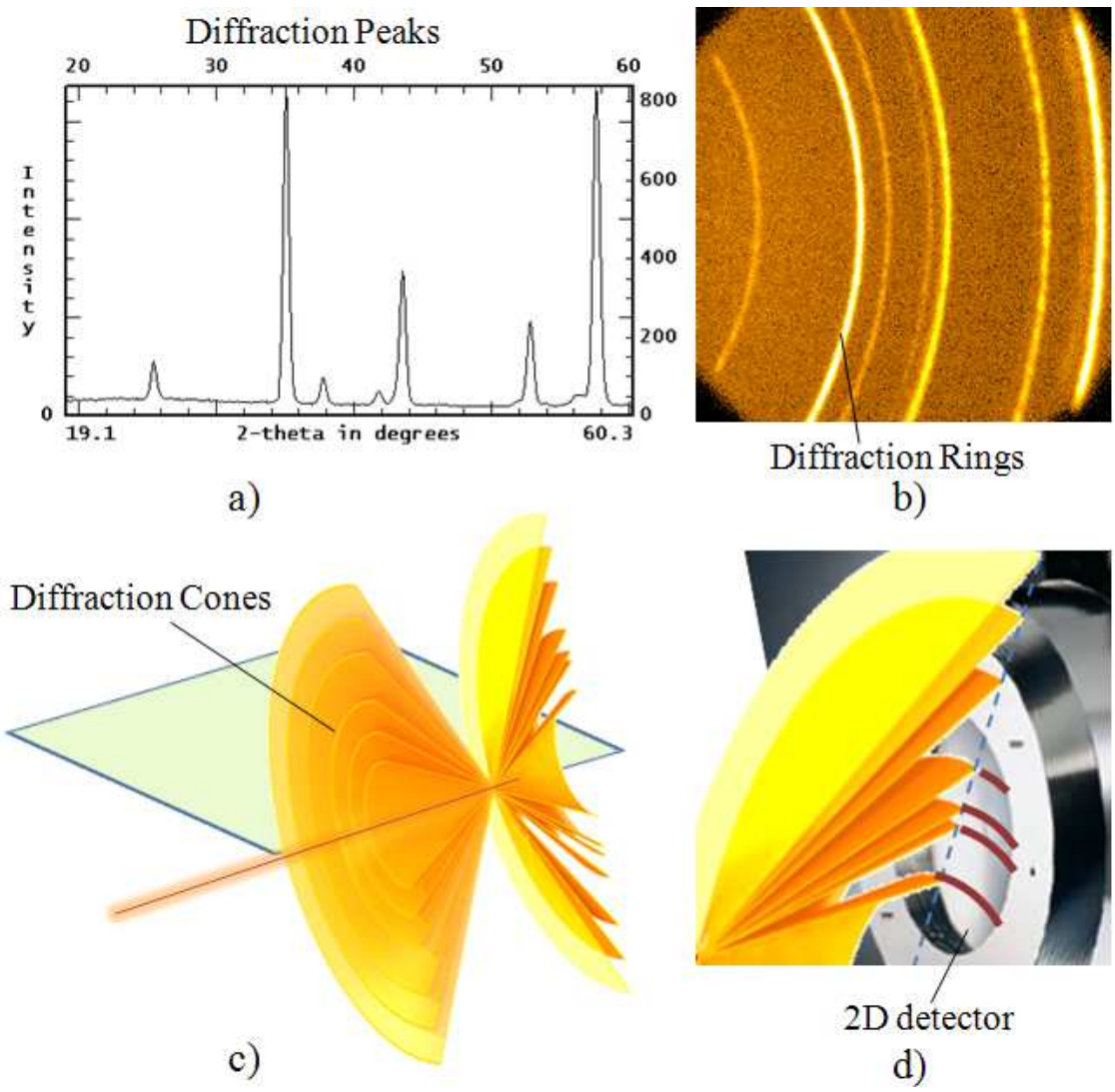

Figure 51 The diffraction pattern of polycrystalline alumina powder: (a) 1D diffraction pattern, (b) The 2D diffraction pattern, (c) The 3D diffraction pattern (simulated from ICCD card 00-046-1212) d) conic section of diffraction cone with 2D detector.

Figure 52 illustrates the geometry of a diffraction cone with detection surface of a flat 2D detector at two different distances between the sample and the detector (D_i). The detector swing angle is called α. The detector was kept at constant angular position ($\alpha = 20°$) for

all the 47 frames. Changing the swing angle conic sections are no longer circular and may be an ellipse, parabola, or hyperbola depending the way that detector plane cuts the diffraction cones [77]. In the case of a sample without residual stress, diffraction cones are right circular, where right means that the axis passes through the center of the base circular means that the base is a circle.

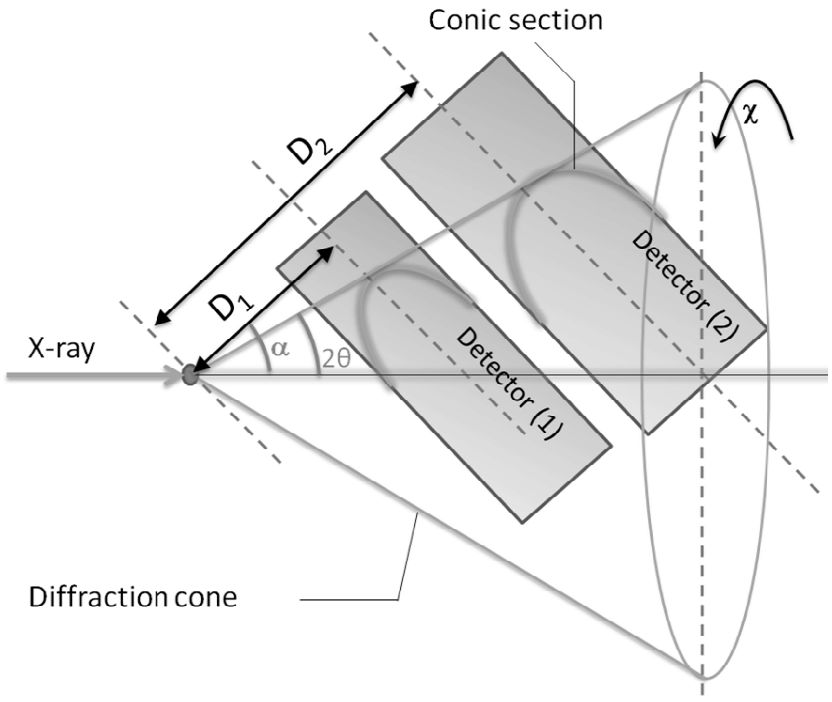

Figure 52 a) Schematic of conic section a 2D detector plane with a diffraction cone at two different distances.

A mosaic pattern of frames collected along different detector distances from the standard alumina sample is shown in Figure 53. The frame collected at the closest distance (7 cm) had the greatest number of rings and the frame collected at the furthest distance (30 cm) had the least rings. Frames close to the sample cover a larger segment of the diffraction cones in χ but they have less angular resolution. Along with conservation of energy, X-

rays are absorbed as they pass through materials according to an exponential law, so rings in frames at a closer sample detector distance are much brighter and have more intensity.

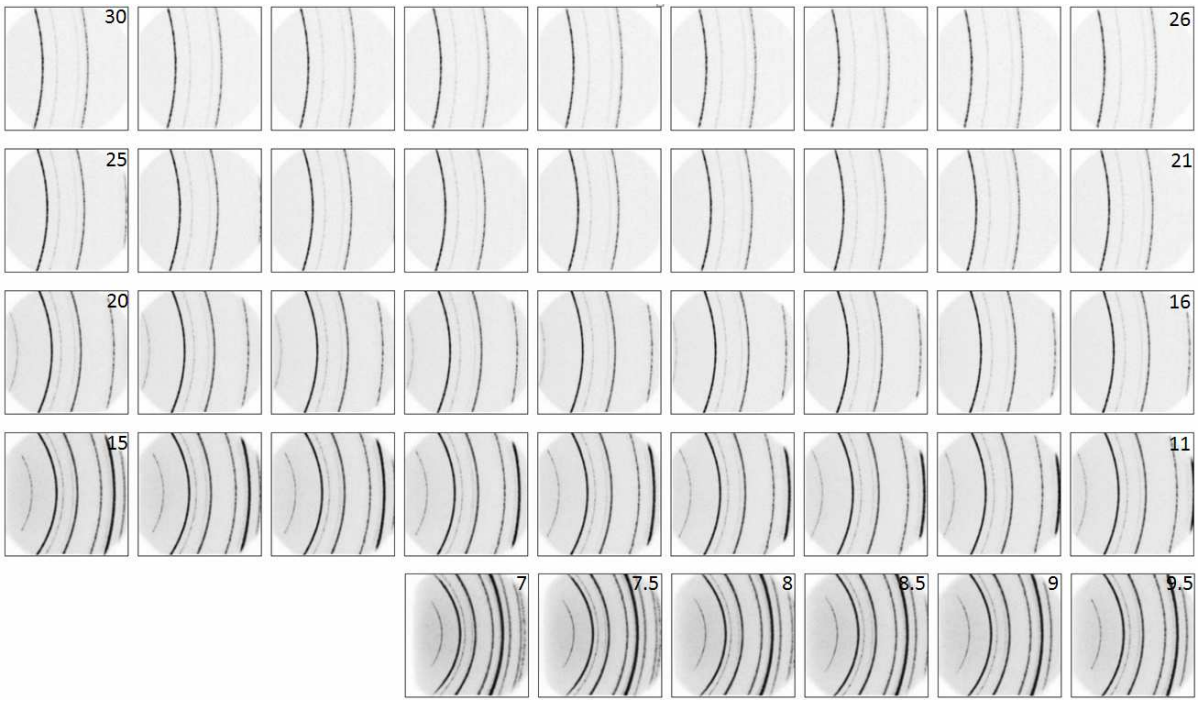

Figure 53 Mosaic pattern of 2D XRD frames with different detector distance starting from 7 cm to 30 cm with 5 mm steps. The number on right top corner of the frame represents the detector distance.

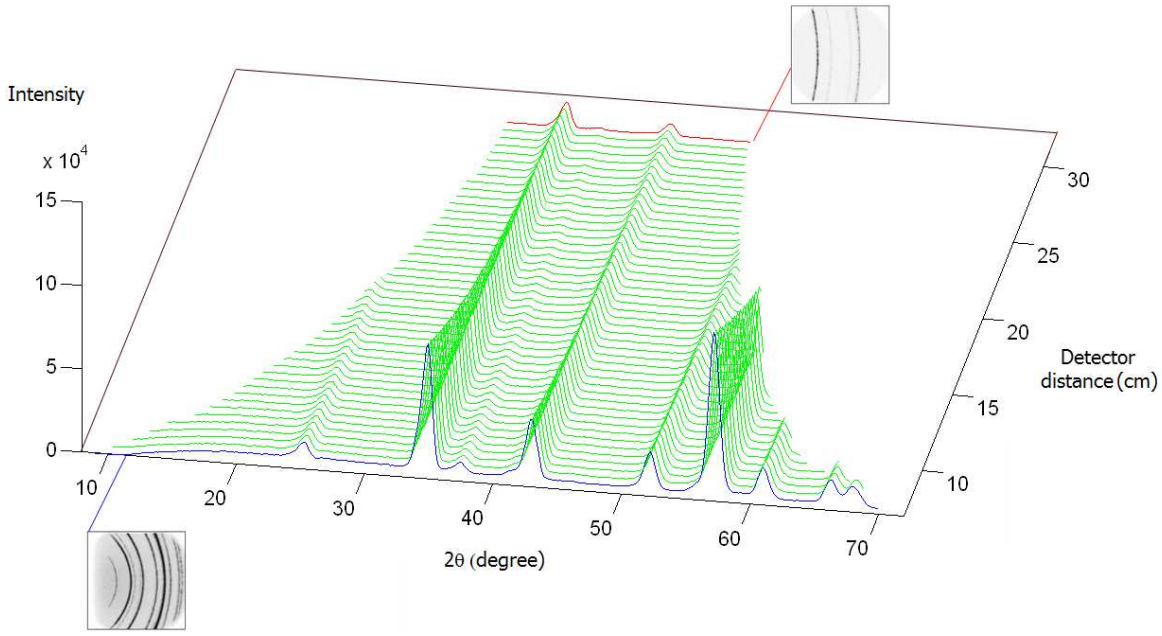

Figure 54 intensity change of rings vs detector distance.

The same trend of intensity decrement also exists for the frame background level. All frames were integrated in the χ direction and their intensity normalized to length of χ coverage is plotted in Figure 54. The intensities should be normalized to the length of χ coverage, as frames with increasing detector distance cover smaller segments of the diffraction cone.

The ".gfrm" files were opened in GADDS software with a proper contrast and then 1024×1024 pixel size ".TIF" format screen shots were captured. Using a global threshold, automatic image segmentation was effectively implemented in segmenting the diffraction rings from background of the frames. Figure 55 shows the rings distinguished from background and the passive area of a particular frame captured at a 12 cm sample-detector distance.

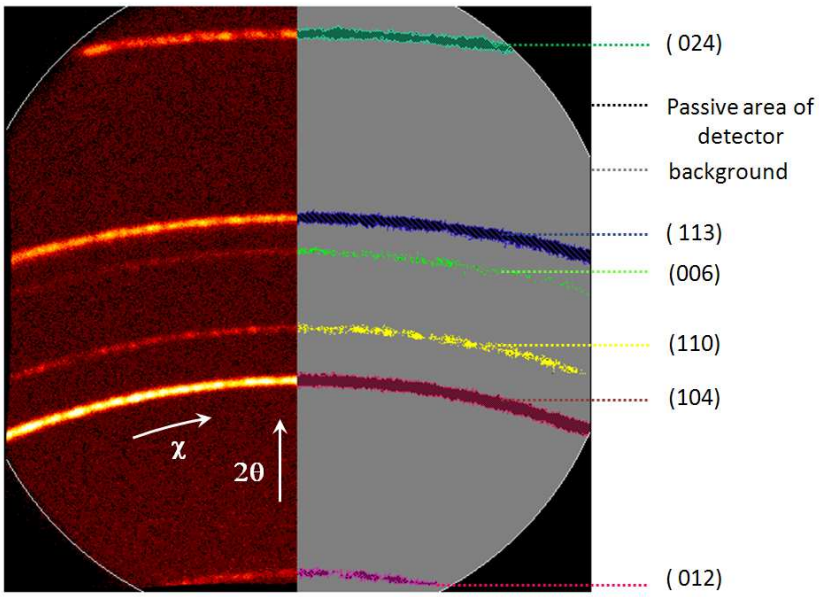

Figure 55 Semi segmented area of 2D frame. Gray color is the background, black is passive area of detector and different rings are separated with different color.

Figure 56a demonstrates all 47 frames imported as sequence of images.[†] In Figure 56b selected frames are shown with transparency.

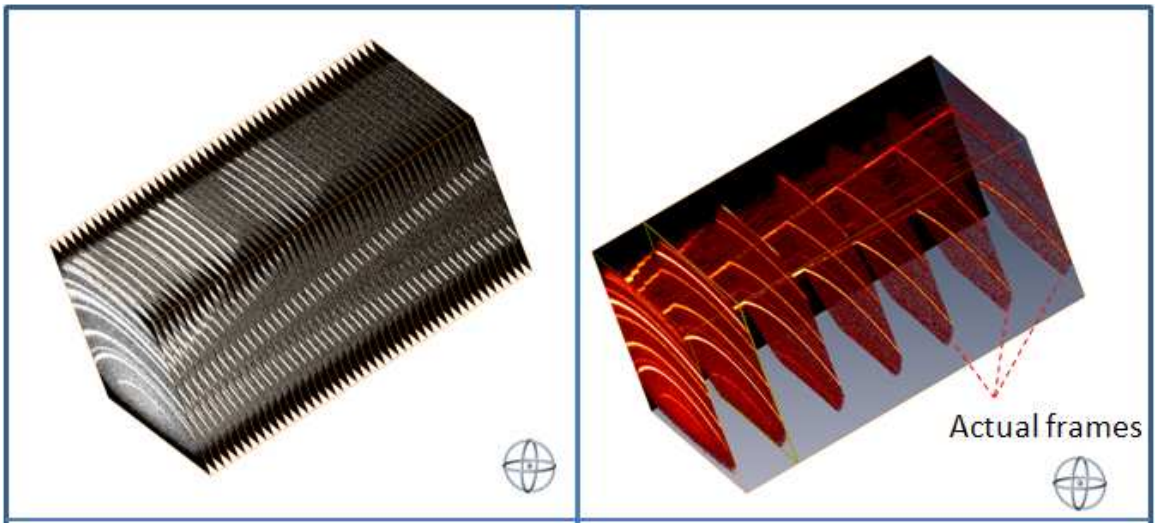

[†] Three dimensional data analysis and visualization was carried out using Amira 3.1.1.

Figure 56 a) Sequential frames b) Visualization of selected semi transparent frames.

Any arbitrary plane can be selected to see the cross section of the data set. This is a means to change the detector position and directions virtually among the data set and look at a particular **virtual frame**. We call these cross sections virtual frame as they can be used for all possible analysis similar to an actual raw data frame. Figure 57 and b show an oblique cross section cut and an orthogonal cross section (virtual frame). One can navigate through the data set and look at any arbitrary cross section.

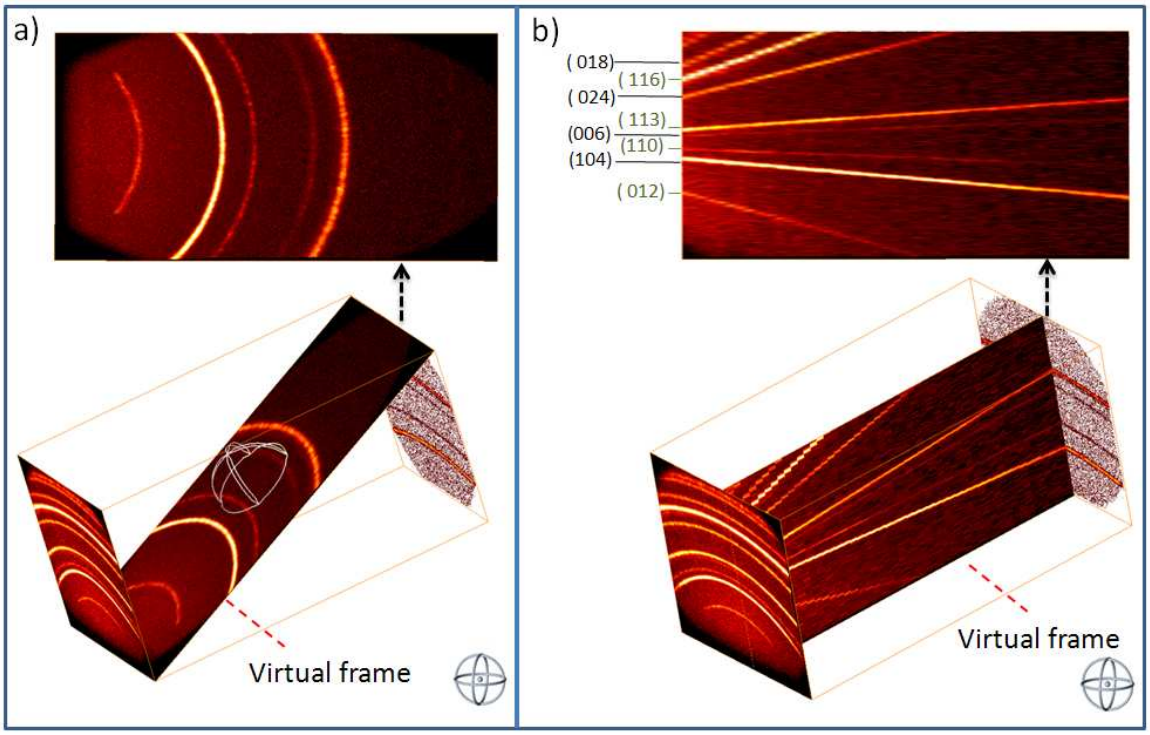

Figure 57 Oblique cross section (virtual frame). b) Orthogonal cross section (virtual frame).

6.3.1 Accessing the information of diffraction cone

In order to visualize the volumetric nature of diffraction cones, two solid volumetric parts of diffraction cones included in the data set from (113) and (104) are illustrated in Figure 58a. In the case of polycrystalline materials, each diffraction ring is made up a large number of small spots, each from a separate crystal particle. The spots lie so close together that they appear a continuous line when the detector is close to the sample as shown in Figure 58b. Figure 58c and d are frames collected from the same section of a diffraction cone at a larger sample-detector distance. When increasing the sample-detector distance, field of view, and intensity of rings decreases as resolution increases. The spottiness nature of cones is observable from Figure 58d. This spotty nature of diffraction makes the diffraction cone a discontinuous surface when the detector is located far from the sample. Rings with less intensity will be spotty at a much shorter sample-detector distance than high intensity rings. The ring (104) has 1.5 times higher intensity than the (113) ring, and as is observable from Figure 58d, the ring (113) is spotty at a 30 cm sample-detector distance while the (104) ring still is continuous.

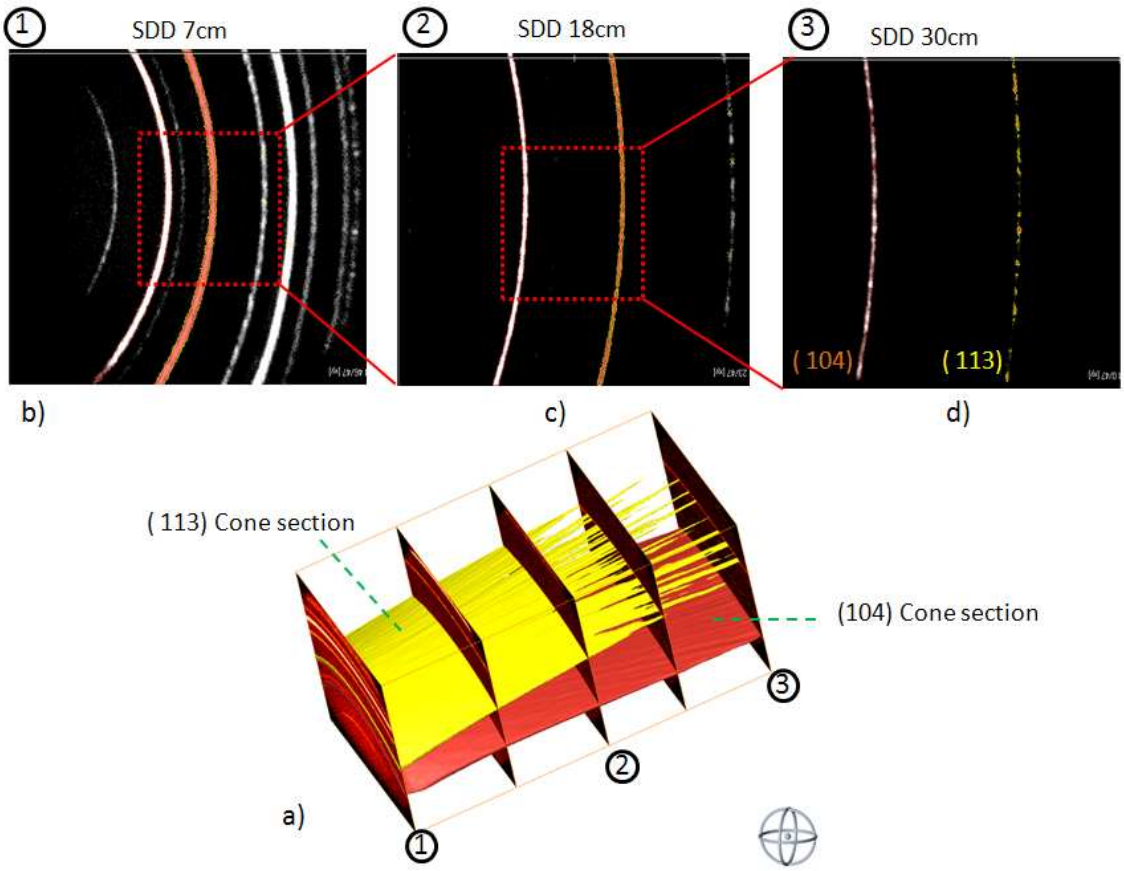

Figure 58 a) Volumetric visualization of two diffraction cone sections. (113) becomes discontinues after position (2) for detector b), c) and d) are frames at different sample-detector distance (SDD) from the same region of cones.

A surface mesh with closed boundaries consisting of triangles was generated for volumetric visualization of the diffraction cones that were included in the data sets, as shown in Figure 59a. Using a proper threshold, a diffraction cone can be considered as a shell between two top and bottom surfaces, as shown in the zoom image (Figure 59b). In conventional 1D XRD, the shape of a powder diffraction peak can be characterized by a Full Width at Half Maximum (FWHM). Here we define the average thickness of a diffraction cone shell as a simple way for characterization in correspondence to the

FWHM in conventional diffraction. The following discusses a method used to calculate the local thickness of a diffraction cone shell. There are two surface functions, for a top surface $f_t(x,y)$ and for the bottom $f_b(x,y)$, obtainable from the triangular surface mesh, as illustrated in Figure 59b.

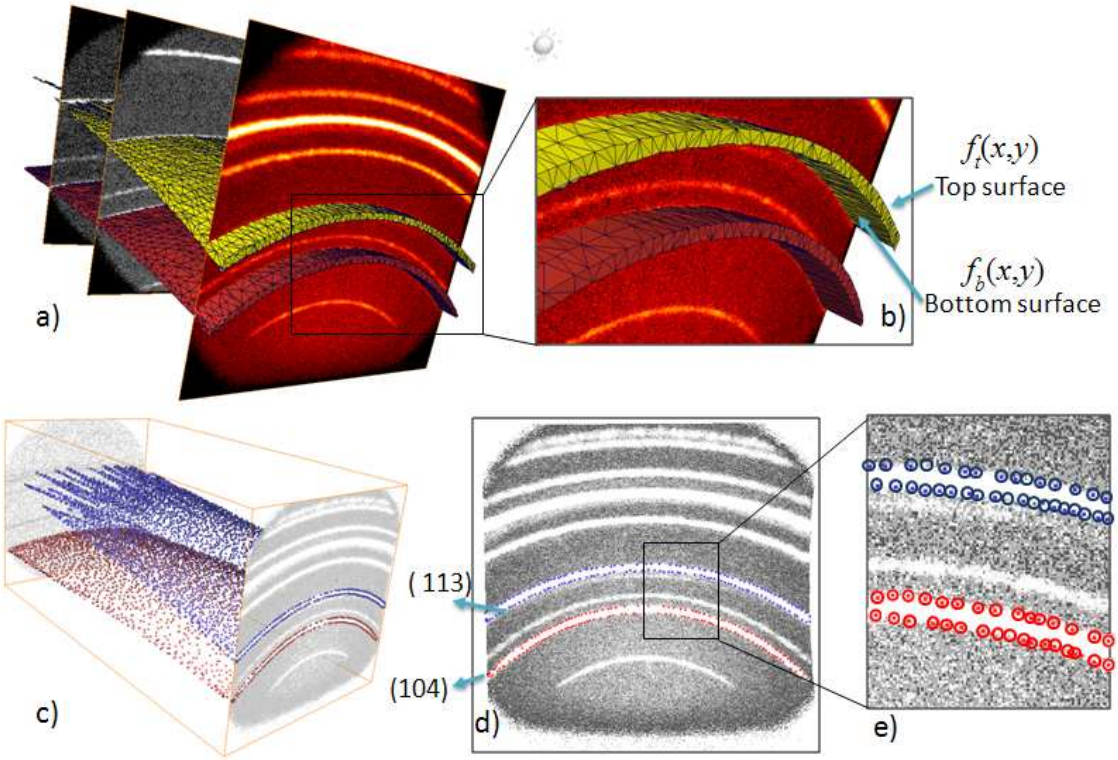

Figure 59 a) Surface mesh on (113) and (104) diffraction cones. b) The surface mesh confines the diffraction cone section between two upper and lower surfaces functions. c) Cloud of points placed on the top and bottom surfaces of diffraction shells. d) Points are located on lower and upper boundary of the rings. e) A zoom image showing the location of typical boundary points.

Because $f_t(x,y)$ and $f_b(x,y)$ are two locally variant curved functions, the distance between them is not well defied. First an interpolated surface function between the top and

bottom surfaces is fitted, and then the shortest point-to-surface distance for all points placed on the top and bottom surfaces was calculated. The average thickness for (104) and (113) cones was 0.95 and 1.16° respectively.

A right cone of apex to base *h* and base radius *r* oriented along the y axis, with vertex at origin as shown in Figure 60 can be described by the an implicit Cartesian equation.

$$z_i = \pm\sqrt{c^2 {y_i}^2 - {x_i}^2} \qquad \text{For } y_i \in [0,h] \text{ and } x_i \in [0,r] \qquad \textbf{6-1}$$

Where $c = \frac{r}{h}$ =tan (2θ). The opening angle 2θ of a diffraction cone which is the vertex angle made by a cross section through the apex and center of the base could have a constant value between 0 and π.

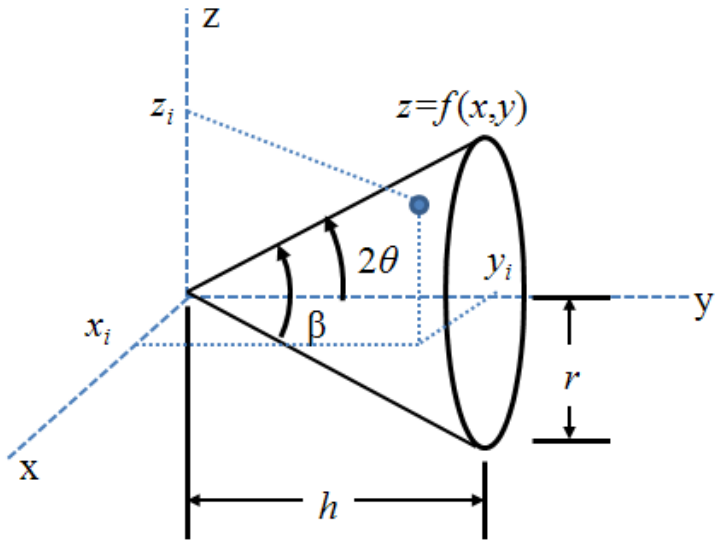

Figure 60 Diffraction cone geometry.

Similar to curve fitting on 2D detector frames for finding a diffraction ring, a customized Matlab code was developed to 3D-interpolate the diffraction cone surface with the

function in equation 1. This interpolated surface was used both for thickness measurement and to determine the 2θ value for the (104) and (113) cones. The results of 3D interpolation on (104) cone section is illustrated in Figure 61 and the 2θ value found to be 35.09°. This corresponds to 35.153° according to the 00-046_1212 ICCD Powder diffraction file.

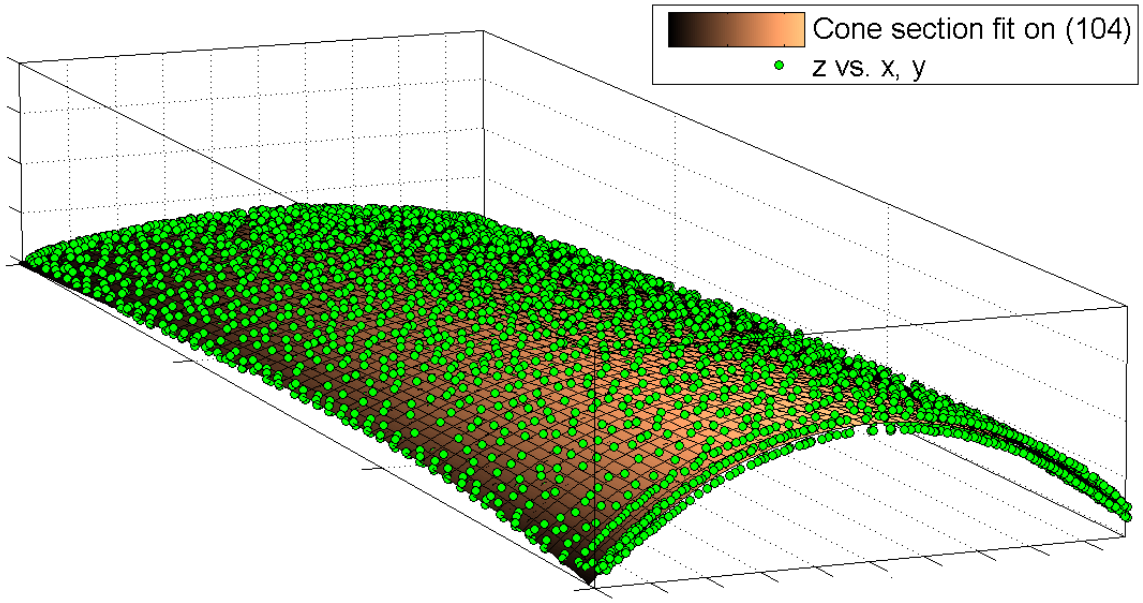

Figure 61 3D interpolated surface between points cloud for (104) cone.

6.4 Conclusion

Detecting the complete X-ray diffraction cone in 3D space is an attractive way for development of new experimental techniques in X-ray science. A new approach for characterizing materials using X-ray diffraction has been developed. Using a Bruker D8 Laboratory X-ray diffractometer and a 2D Hi-star detector, sequences of frames with a fixed experimental set-up at different sample detector distances were recorded. Recorded frames were visualized in 3D and the concept of a virtual frame was developed. Virtual

frames were introduced as an arbitrary cross section of the data set which is similar to what a 2D detector would record if it placed in such an arbitrary cross-section in a real experimental set up. Appling a proper threshold, rings were separated from background and solid shells of diffraction cones were visualized. Nodes on surface meshed solid shell represented the diffraction cone used for 3D interpolation. The thickness of the shell was measured and introduced to correspondence to the FWHM of peaks in conventional X-ray diffraction. The opening angle, 2θ of a diffraction cone was calculated from 3D interpolation on an example peak and found in agreement with the ICCD card corresponding value.

This is the beginning of 3D detection and visualization of X-ray diffraction cone. A more comprehensive data set is required for additional development of the method. A wider detector equipped with motorized sample-detector distance driver is recommended. The current method of data collection could be implemented for residual stress measurements. Residual stresses, depending on magnitude and direction, distort the diffraction cone. In polycrystalline samples, from the shape, intensity change along the surface of diffraction cone, and discontinuity of the 3D cones; useful data like graininess of the sample, depth of diffraction, grain size and distribution could be extracted.

CHAPTER VII

7 Conclusions

- Mapping contact induced phase transformation of dental ceramics

The zirconia polycrystalline tetragonal structure greatly exhibits phase transformation at the impacted region due to compressive stress concentration. Tetragonal to monoclinic phase transformations were observed in 2D micro X-ray diffraction frames from yttria stabilized zirconia using a 200 µm diameter X-ray beam. Results of an elastic strain map for the (101) tetragonal peak suggests stress relaxation by phase transformation. More phase transformation was detected at inner section of the lingual side, because the initial state of compressive residual stress assists this phase transformation at the inter section of lingual side of the core while initial tensile stress at the outer sides under the veneer relaxes under compression and initially prevents phase transformation.

- Investigating a combined residual stress and phase transformation measurement

Coupling phase transformation and residual stress measurement is an important factor in design, because transformation under critical load retards failure. Using Bruker D8 micro X-ray diffraction, a laboratory method of combined phase transformation and residual stress measurement were adapted for dental crown studies. A significant range of residual stresses from a compressive stress of -400 MPa up to tensile stress of 400 MPa

and up to 100% tetragonal to monoclinic phase transformation were observed for an impacted crown under a single load to failure.

- Development of a model for residual stress prediction of various porcelain layer thicknesses

The residual stress was tensile in the zirconia side of the interface and compressive in the porcelain side. The magnitude of the residual stress depends on initial and final temperature as well as the thickness of the porcelain and zirconia layers.

Based on the fundamental equations for strain, an analytical model for a bi-layer ceramic composite was developed. The bilayer model consisting of a 0.5 mm yttria stabilized tetragonal zirconia disk veneered with a 0.5 mm thick porcelain had a predicted residual stress (σx) of -60 MPa, 100 MPa, -40 MPa, and 10 MPa for the bottom of the zirconia layer, the zirconia at the interface, the porcelain at the interface, and the top surface of the porcelain respectively.

- A recommendation for minimum porcelain thickness in modern crown design

Considering the thickness measurement results with residual stress prediction for bi-layer ceramics shows locations where the thickness of the porcelain relative to the zirconia layer is small (<0.2 mm). These locations are high in residual stress and a likely initiation site for clinical failures, so therefore should be avoided. For a typical crown only 3.3% of the porcelain was below than 0.2 mm. This can be avoided by minor adjustments on the initial design.

7.1 Measurement advancements

- Development of a new method for X-ray diffraction mapping on curved surfaces

In case of dental crown, a part of surface may block the X-ray beam before reaching the desired point or diffracted rays might be blocked partially or completely before reaching the detector. Considering a complex geometry of a crown an efficient method for X-ray diffraction data collection mapping on a given curved surface was developed. This method is general and applicable to other complex geometry materials. Using this method, a correlation between tetragonal to monoclinic phase transformation and height of the local position was observed.

- X-ray Diffraction mapping with five axis stage and genetic algorithm optimization

A new approach for characterizing curved surface properties using micro X-ray diffraction was developed. Using genetic algorithm optimization, the required time for tilt and rotation between the exposures has decreased from 6 hours to 2 hours and 15 minutes, which is a 37.5% improvement.

- Porcelain layer thickness measurement method using X-ray micro tomography

Tomography data to reconstruct the 3D structure of the crown followed by finite element surface meshing to calculate the minimum distance between nodes on surfaces. Thickness measured using this method can be coupled by bi-material bending equations to approximate the state of residual stress at different locations of the crown.

-Three Dimensional X-Ray Diffraction Cone Detection and Visualization

A novel method of data collection and visualization of three-dimensional X-ray diffraction (XRD^3) was developed. A virtual frame as a new term in the XRD field was introduced, which is an arbitrary cross section of the data set, similar to what a 2D

detector would record if it is placed in such an arbitrary cross-section in a real experimental set up.

CHAPTER VIII

8 Future work

8.1 Phase mapping

The current research work so far has been focusing on developing models and techniques and validating the results. In collaboration with CEO Nautilus dental Studio we have received samples prepared with different parameters. Implementing the current methods on those samples and more collaboration with dental labs is one of the future directions. From this we will have information on residual stress as a function of differences in cooling methods and be able to provide a technique that can offer the dental community badly needed feedback on optimizing processing methods.

Comparing and validating the results with other techniques like nano indentation and simulation is the next goal. This comparison is planned to be done on a simplified flat disk sample to reduce the unknowns. This flat sample has been impacted by custom build load frame to mimic the chewing mechanism. Figure 62 shows the rectangular grids planed to be replaced with customized mesh.

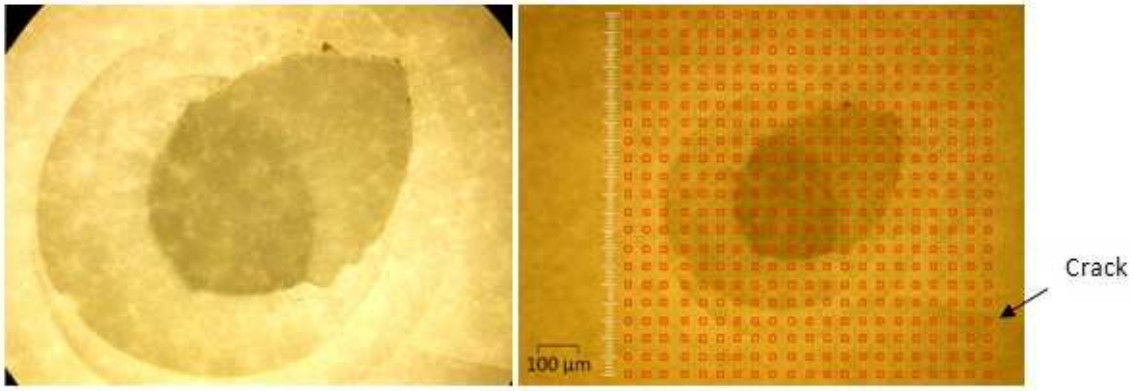

Figure 62 optical image of impacted area by fatigue loading on a flat zirconia sample.

The aim of collecting several micro XRD frames on impacted area is to map the phase transformation in zirconia structure. Phase transformation mostly occurs at the center of impact region and drastically decreases by distance from center. Instead of a rectangular grid, micro XRD frames could be collected on the specially designed grid as shown in Figure 63.

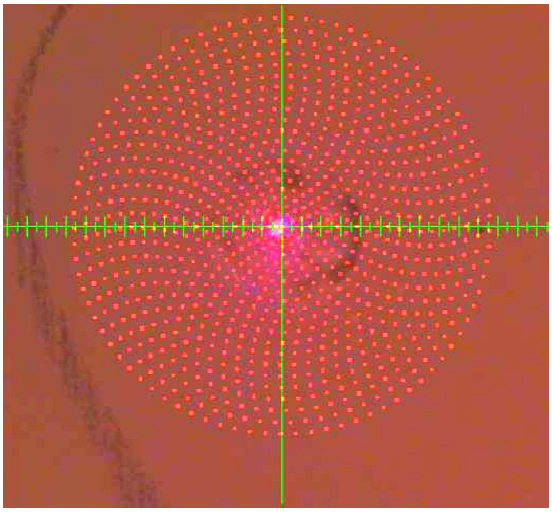

Figure 63 proves that it is possible to collect the data on customized mesh.

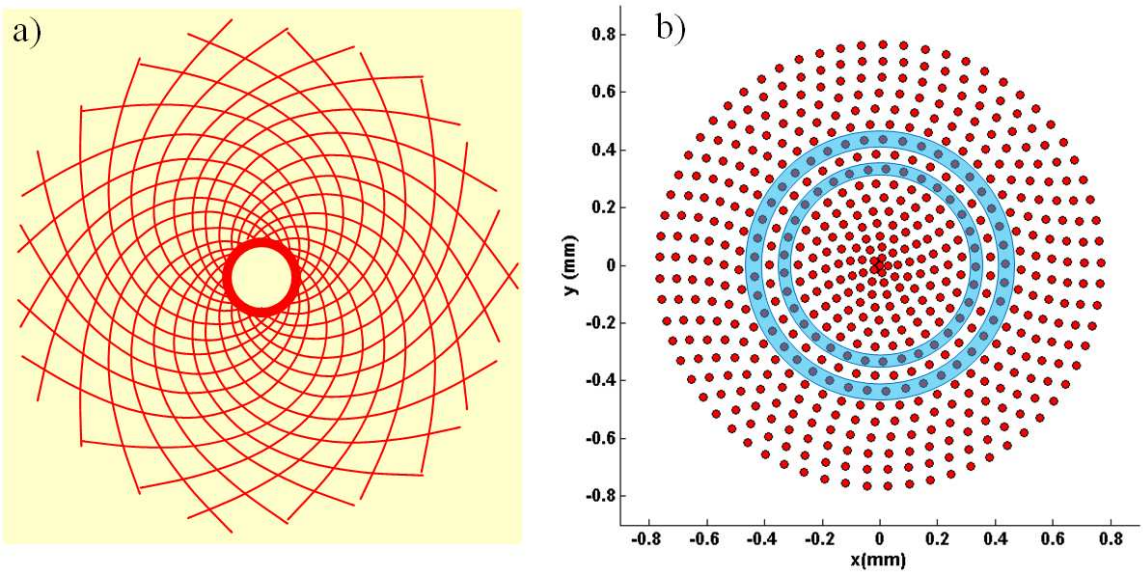

Figure 64 a) Fibonacci sequence appearing in sunflowers b) modified for our purpose.

Using a Matlab code, points initially were created in polar coordinates and then transformed to the Cartesian coordinate in a file understandable by the GADDS system controller software. The developed code creates fairly distributed points in the measurement domain. Each set of points is on a circumference of a circle with equal angular distance. Circles are not equally spaced and the distance between circles is growing by a growth factor of 1.3 in order to collect fewer frames at other regions. A similar pattern shown in Figure 64a appearing in nature in sunflowers is describable by a Fibonacci sequence. Here a following series was used to find the number of points on the consequent same center circles.

$$a_{n+1} = 2a_n - 1 \qquad \textbf{8-1}$$

8.2 Diffraction from single grains at interface

Studying and analyzing the collected data of the phase transformation for individual grains observed at the interface of porcelain and zircoina is the next goal to achieve. A typical frame containing individual phase transformed grain is shown in Figure 65.

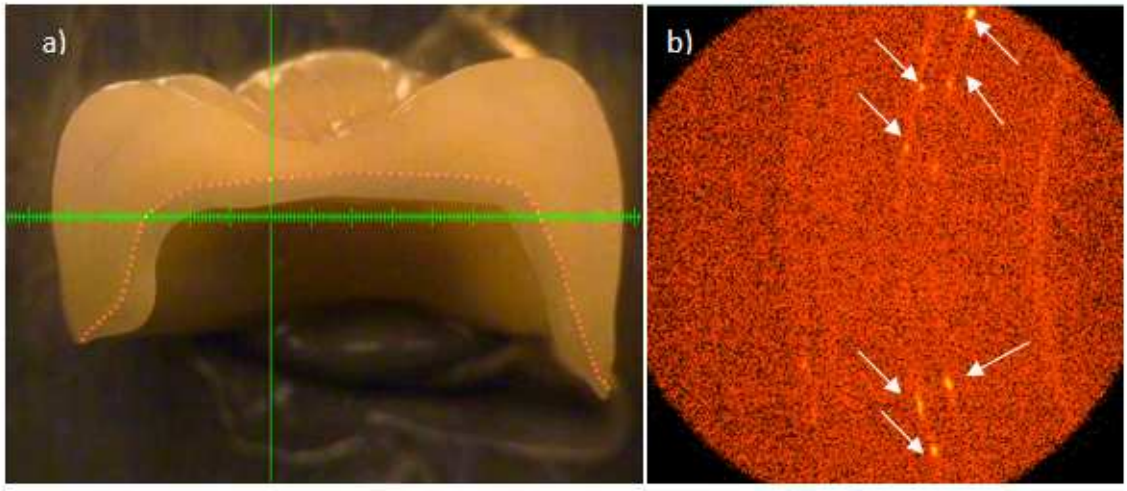

Figure 65 a) Measurement points located at interface b) individual grain transformed grains.

To develop a more theoretical and experimental relation between phase transformation and residual stress in meta stable zircoina crowns, more experiments are underway.

8.3 Three Dimensional X-Ray Diffraction and residual stress measurement

In Chapter 7 it has been tried to develop concepts of three dimensional X-ray diffraction data collection and visualization technique. The main goal of the chapter was to collect a three dimensional data set and visualize it. It is a long way to improve the method and implement it for real applications like residual stresses measurement. In recent decade, advances in 2D X-ray diffraction have been remarkable and it is well developed to be

considered comparable with conventional 1D XRD method. There is considerable room for developing the method.

8.4 Further developments

1) Repeat this study to further quantify and study the coupling of phase transformation and residual stress. This could be done first on flat plates.
2) The methods developed here could be used to confirm the minimization of residual stress from engineering the CTE of porcelain.
3) Measure the improvement on residual stress from avoiding the thin regions in a crown.
4) Nanoindentation measurement of residual stress could be validated by XRD in crystalline systems such as alumina or zirconia to then implement for determining the residual stresses in porcelain. In general the XRD methods developed here can be used to validate and infer the residual stresses in porcelain.
5) The methods developed here can be used to validate FEM models predicting residual stress in dental restoration associated with phase transformation.

REFERENCES

[1] R.J. Kohal, G. Klaus, J.R. Strub, “Zirconia-implant-supported all-ceramic crowns withstand long-term load: a pilot investigation”, Clinical Oral Implants Research, 17(5): 565-571, (2006).

[2] R.J. Kohal, G. Klaus, “A zirconia implant-crown system: a case report”, Int J Periodontics Restorative Dent, 24(2): 147-153, (2004).

[3] B. Kim, Y. Zhang, M. Pines, V.P. Thompson, “Fracture of porcelain veneered structures in fatigue”, J Dent Res, 86, 142-146, (2007).

[4] J.W. Kim, J.H. Kim, V. Thompson, Y. Zhang, “Sliding contact damage in layered ceramic structures, J Dent Res”, 86,1046-1050 (2007).

[5] I. Sailer, A. Feher, F. Filser, L.J. Gauckler, H. Luthy, C.H. Hammerle, “Five-year clinical results of zirconia frameworks for posterior fixed partial dentures”, Int J Prosthodont, 20, 383-388. (2007).

[6] J.W. Kim , J.H. Kim, M.N. Janal, Y. Zhang, “Damage Maps of Veneered Zirconia under Simulated Mastication”, J Dent Res, 87 (12), 1127-1132, (2008).

[7] N. Navruz, “Crystallography of the tetragonal-to-monoclinic phase transformation in ceria-zirconia”, Phase Transitions, 78(7-8), 539–545, (2005).

[8] N. Navruz, “A comparative crystallographic analysis of the tetragonal-to-monoclinic transformation in the yttria-zirconia system”, Physics of metals and metallography, 105(6): 580-585, (2008).

[9] Y. Zhang, H. Chai, J.J.W. Lee, B. R. Lawn, “Chipping Resistance of Graded Zirconia Ceramics for Dental Crowns”, Journal of Dental Research, 91 (3), 311-315 (2012).

[10] S.D. Campbell, "Esthetic modification of cast dental-ceramic restorations," Int J Prosthodont 3(2): 123-129, (1990).

[11] C.L. Chang, C.S. Chen, T.C. Yeung, M.L. Hsu, "Biomechanical effect of a zirconia dental implant-crown system: a three-dimensional finite element analysis," Int J Oral Maxillofac Implants 27(4): 49-57, (2012).

[12] H. Bale, “Measurement and Analysis of Residual Stresses in Zirconia Dental Composites Using Micro X-ray Dissertation”, Ph.D. 3499704, Oklahoma State University, United States, Oklahoma, (2010).

[13] Y. Zhang, M. Allahkarami, J.C. Hanan, “Measuring residual stress in ceramic zirconia–porcelain dental crowns by nanoindentation”, Journal of the Mechanical Behavior of Biomedical Materials, 6,120-127, (2012).

[14] M. Allahkarami, J.C. Hanan, “Residual Stress Delaying Phase Transformation in Y-TZP Bio-restorations”, Phase Transitions, 85(1–2): 169-178, (2011).

[15] S. Timoshenko, “Analysis of bi-metal thermostats”, J. Opt. Soc. Amm, 11: 233–255, (1925).

[16] C.H. Hsueh, S. Lee, T.J. Chuang, “An alternative method of solving multilayer bending problems”, Journal of Applied Mechanics, 70(1): 151-154, (2003).

[17] H.A. Bale, P.G. Coelho, J.C. Hanan, “3D Finite Element Prediction of Thermal Residual Stresses in a Real Dental Restoration Geometry”, submitted

[18] M. Allahkarami, J.C. Hanan, “Residual stress and phase transformation in zirconia restoration ceramics”, Advances in Bioceramics and Porous Ceramics V: Ceramic Engineering and Science Proceedings, John Wiley & Sons, Inc. 33(6): 37-46, (2012).

[19] Y. Zhang, “Residual stress in all ceramic zirconia-porcelain dental system by simulation and nanoindentation”, Ph.D. 3525681, Oklahoma State University, United States, Oklahoma, (2012).

[20] M. Allahkarami, J.C. Hanan, “Mapping the tetragonal to monoclinic phase transformation in zirconia core dental crowns, Dental Materials, 27(12): 1279-1284, (2011).

[21] J. Malzbender, “Curvature and stresses for bi-layer functional ceramic materials”, Journal of the European Ceramic Society, 30(16): 3407-3413, (2010).

[22] O. Addison, G.J.P. Fleming, “Application of analytical stress solutions to bi-axially loaded dental ceramic-dental cement bi-layers”, Dental Materials, 24(10):1336-1342, (2008).

[23] S. Timoshenko, “Analysis of bi-metal thermostats”, J. Opt. Soc. Amm, 11: 233–255, (1925).

[24] C.H. Hsueh, S. Lee, T.J. Chuang, “An alternative method of solving multilayer bending problems”, Journal of Applied Mechanics, 70(1): 151-154, (2003).

[25] C.H. Hsueh, C.R. Luttrell, P.F. Becher, “Analyses of multilayered dental ceramics subjected to biaxial flexure tests”, Dental Materials, 22(5): 460–469 (2006).

[26] C.H. Hsueh, G.A. Thompson, O.M. Jadaan, A.A. Wereszczak, P.F. Becher, “Analyses of layer-thickness effects in bilayered dental ceramics subjected to thermal stresses and ring-on-ring tests ”, Dental materials, 24(1): 9–17, (2008).

[27] M. Allahkarami, H.A. Bale, J.C. Hanan, “Analytical model for prediction of residual stress in zirconia porcelain bi-layer”, Advances in Bioceramics and Porous Ceramics III: Ceramic Engineering and Science Proceedings, John Wiley & Sons, Inc, 31: 19-26, (2010).

[28] N. Verdonschot, W.M.M. Fennis, R.H. Kuijs, J. Stolk, C.M. Kreulen, N.H.J. Creugers, “Generation of 3-D finite element models of restored human teeth using micro-CT techniques”, International Journal of Prosthodontics, 14(4): 310-315, (2001).

[29] M. Allahkarami, J.C. Hanan, H.A. Bale, “Regeneration of surface roughness by the Langevin equation using stochastic analysis on AFM image of a carbon fiber”, Applied Surface Science, 257(3): 857-860, (2010).

[30] M. Allahkarami, J.C. Hanan, “Finite Element Model Generation Based on Stochastic Analysis on AFM Images”, Imaging Methods for Novel Materials and Challenging Applications, Volume 3, Springer New York, 417-421, (2013).

[31] B.D. Agarwal, L.J. Brout-man, K. Chandrashekhara, “Analysis and Performance of Fiber Composites”, Wiley, 3rd edition, 212-273, (2006).

[32] E.H. Kisi, C.J. Howard, “Elastic constants of tetragonal zirconia measured by a new powder diffraction technique”, Journal of the American Ceramic Society, 81(6): 1682-1684, (1998).

[33] B. Jayakumar, M. Allahkarami, J.C. Hanan, “Inter-Cellular Joining for Amorphous Honeycombs”, Composite Materials and Joining Technologies for Composites, 7: 25-33, (2013).

[34] M. Allahkarami, L. Seyed Faraji, G. Kavei, Y. Zare, “Composition and thermoelectric power factor variation of $(Bi_2Te_3)_{0.96}$ $(Bi_2Se_3)_{0.04}$ crystal in growth direction”, Materials Chemistry and Physics, 119(1-2): 145-148, (2010).

[35] G. Kavei, M.A Karami, “Fabrication and characterization of the p-type $(Bi_2Te_3)_x$ $(Sb_2Te_3)_{1-x}$ thermoelectric crystals prepared via zone melting”, Bulletin of Material Science, 29(7): 659-663, (2006).

[36] L.S Faraji, R.P Singh, M. Allahkarami, “Pulsed laser deposition of bismuth telluride thin film and annealing effects”, The European Physical Journal Applied Physics 46(2): 20501P1-20501P5, (2009).

[37] M. Zakeri, M. Allahkarami, Gh. Kavei, A. Khanmohammadian, M.R. Rahimipour, “Synthesis of nanocrystalline Bi_2Te_3 via mechanical alloying”, Journal of materials processing technology, 209(1): 96-101, (2009).

[38] M. Zakeri, M Allahkarami, Gh. Kavei, A. Khanmohammadian, M.R. Rahimipour, “Low temperature synthesis of nanocrystalline Sb_2Te_3 by mechanical alloying”, Journal of Materials Science, 43(5): 1638-1643, (2008).

[39] M.V. Swain, “Unstable cracking (chipping) of veneering porcelain on all-ceramic dental crowns and fixed partial dentures”, Acta Biomaterialia, 5(5): 1668–1677, (2009).

[40] H.A. Bale, J.C. Hanan, N.Tamura, M. Kunz, P. Coelho, V. Thompson, “Interface Residual Stresses in Dental Zirconia Using Laue Micro-Diffraction”, JCPDS-International Centre for Diffraction Data, 368-375, (2009).

[41] M.W. Bowler, M. Guijarro, S. Petitdemange, I. Baker, O. Svensson, M. Burghammer, C. Mueller-Dieckmann, E.J. Gordon, D. Flot, S. M. McSweeney, G. A. Leonard, “Diffraction cartography: applying microbeams to macromolecular crystallography sample evaluation and data collection”, Acta Cryst, D66(8): 855–864, (2010).

[42] Bruker (2005), M86-EXX007 GADDS User Manual, ch 12, Bruker AXS Inc., Madison, Wisconsin, USA

[43] C. Boote, S. Dennis, K. Meek, “Spatial mapping of collagen fibril organization in primate cornea-an X-ray diffraction investigation”, Journal of Structural Biology, 146(3): 359–367, (2004).

[44] C. Moore, J. Hennessy, “Applications of XRD mapping to the control of compound Sem-conductor Processes”, Characterization feature, 6(6): 14-17, (1993).

[45] C. Moore, Philips Analytical, “Uniformity mapping using X-ray diffraction”, III-Vs Review,11(6): 30-34, (1998).

[46] J. Forest, J. Salvi, “A review of laser scanning three-dimensional digitizers”, Proceedings of the 2002 IEE/RSJ Intl. Conference on Intelligent Robots and Systems EPFL, Lausanne, Switzerland (October 2002).

[47] P. Magne, “Efficient 3D finite element analysis of dental restorative procedures using micro-CT data”, Dental Materials, 23(5):539-548, (2007).

[48] T.H. Cormen, C.E. Leiserson, R.L. Rivest, C. Stein, “Introduction to Algorithms”, Second Edition, MIT Press, (2001)

[49] B. Kim, Y. Zhang, M. Pines, V.P. Thompson, “Fracture of porcelain veneered structures in fatigue”, J Dent Res, 86(2): 142-146, (2007)

[50] J.W. Kim, J.H. Kim, V. Thompson, Y. Zhang, “Sliding contact damage in layered ceramic structures”, J Dent Res, 86(11): 1046-1050, (2007).

[51] N. Nezafati, F. Moztarzadeh, S. Hesaraki, M. Mozafari, “Synergistically reinforcement of a self-setting calcium phosphate cement with bioactive glass fibers”, Ceramics International, 37: 927-934, (2011).

[52] M. Azami, S. Jalilifiroozinezhad, M. Mozafari, “Synthesis and solubility of calcium fluoride/hydroxy-fluorapatite nanocrystals for dental applications”, Ceramics International, 37: 2007-2014, (2011).

[53] J.Y. Thompson, K.J. Anusavice, A. Naman, H.E Morris, “Fracture surface characterization of clinically failed all-ceramic crowns”, J Dent Res, 73(12):1824-1832, (1994).

[54] R.J. Kohal, G. Klaus, “A zirconia implant-crown system: a case report”, Int J Periodont Rest Dent, 24(2):147-153, (2004).

[55] N.R. Silva, E.A. Bonfante, B.T. Rafferty, R.A. Zavanelli, E.D. Rekow, V.P. Thompson, P.G. Coelho, “Modified Y-TZP core design improves all-ceramic crown reliability”, J Dent Res, 90(1): 104-108, (2011).

[56] M. Allahkarami, J. C. Hanan, H. A. Bale, “Characterization of non uniform veneer layer thickness distribution on curved based Zirconia ceramic using X-ray micro-tomography”, Developments in Strategic Materials and Computational Design II, 153-163, (2011).

[57] K. Asaoka, N. Kuwayama, J.A. Tesk, “Influence of tempering method on residual stress in dental porcelain”, J Dent Res, 71(12): 1623-1627, (1992).

[58] M. De Kler, N. De Jager, M. Meegdes and J.M. Vanderzel “Influence of thermal expansion mismatch and fatigue loading on phase changes in porcelain veneered Y-TZP, zirconia discs”, Journal of Oral Rehabilitation, 34(11): 841–847, (2007).

[59] S.J Lee, W.M. Kriven, “Shrinkage-free alumina–glass dental composites via aluminum oxidation”, Journal of American Ceramic Society, 80(8): 2141–2147, (1997).

[60] C.W. Fairhurst, K.J. Anusavice, D.T. Hashinger, R.D. Ringle, and S.W. Twiggs, “Thermal expansion of dental alloys and porcelains”, Journal of Biomedical Materials Research, 14(4): 435-46, (1980).

[61] Y. Zhang, J.W. Kim, “Graded zirconia glass for resistance to veneer fracture”, J Dent Res, 89(10):1057-1062 (2010).

[62] H.A. Bale, N. Tamura, J.C. Hanan, “Microbeam X-ray grain averaged residual stress in dental ceramics”, Advances in Bioceramics and Porous Ceramics IV: Ceramic Engineering and Science Proceedings, 32: 49-63, (2011).

[63] H.A. Bale, J.C. Hanan, J.E. Smay, “Thermal Interface Stresses Including 3D Microstructures in Layered Free-Form Ceramics”, Advances in Bioceramics and Porous Ceramics: Ceramic Engineering and Science Proceedings, 3-17, (2008).

[64] J.C. Hanan, H.A. Bale, “High residual stress between zirconia grains observed with Laue-micro diffraction”, ASME international mechanical engineering congress and exposition, (2009).

[65] P.S. Prevey, “X-ray Diffraction residual stress techniques”, Metals Handbook, 10, Metals Park, American Society for Metals, 380-392, (1986).

[66] J.T. Assis, V. Monin, J.R. Teodosio, T. Gurova, “X-ray analysis of residual stress distribution in weld region”, JCPDS-International Centre for Diffraction Data Advances in X-ray Analysis, 45: 225-231, (2002).

[67] H. Bale, N. Tamura, P. Coelho, J.C. Hanan, “Impact Fatigue Deformation and Residual Stress Evolution in Dental Ceramics”, Fatigue and Fracture in Non-metallic Materials, Society of Experimental Mechanics Annual Conference & Exposition on Experimental and Applied Mechanics, (2009).

[68] A.D. Krawitz, “Introduction to diffraction in materials, science, and engineering”, John Wiley, 2001

[69] M.T. Hutchings, P.J. Withers, T.M. Holden, T. Lorentzen, “Introduction to the Characterization of Residual Stress by Neutron Diffraction” , chapter 4, 2005, CRC press, Taylor& Francis

[70] B.B. He, U. Preckwinkel, K.L. Smith, “Comparison between conventional and two-dimensional XRD”, Advances in X-ray Analysis, 46: 37-42, (2003).

[71] B.B. He, U. Preckwinkel, K.L. Smith, “Advantages of Using 2D Detectors for Residual Stress Measurements”, Advances in X-ray analysis, 42: 429-438, (2000).

[72] D. Faurie, G. Geandier, P.O. Renault, D. Thiaudière, “$\mathrm{Sin}^2\,\psi$ analysis in thin films using 2D detectors: Non-linearity due to set-up, stress state and microstructure”, Thin Solid Films, (2012), doi:10.1016/j.tsf.2012.02.031

[73] M. Al-Jawad, A. Steuwer, S.H. Kilcoyne, R.C. Shore, R. Cywinski, D.J. Wood, “2D mapping of texture and lattice parameters of dental enamel”, Biomaterials, 28(18): 2908-2914, (2007).

[74] M. Allahkarami, J.C. Hanan, “X-ray diffraction mapping on a curved surface”, Journal of Applied Crystallography, 44: 1211–1216, (2011).

[75] S.N. Sulyanov, A.N. Popov, D. M. Kheiker, “Using a Two-dimensional detector for X-ray powder diffractometry”, Journal of Applied Crystallography, 27: 934-942, (1994).

[76] M.B. Dickerson, K. Pathak, K.H. Sandhage, R.L. Snyder, U. Balachandran, B. Ma, R.D. Blaugher, R.N. Bhattacharya, “Applications of 2D detectors in X-ray analysis”, Advances in X-ray Analysis, 45: 338-344, (2002).

[77] B.B. He, U. Preckwinkel, K.L. Smith ,“Fundamentals of two-dimensional X-ray diffraction (XRD^2)”, Advances in X-ray Analysis, 43: 273-280, (2000).

[78] H.A. Bale, J.C. Hanan, N. Tamura, “4D XRD for strain in many grains using triangulation”, Powder Diffraction, 21(2): 184-194, (2006).

[79] H.J. Bunge, L. Wcislak, H. Klein, U. Garbe and J.R. Schneider, “Texture and microstructure imaging in six dimensions with high-energy synchrotron radiation”, Journal of Applied Crystallography, 36: 1240-1255, (2003).

[80] B. B. He, “Two-dimensional X-ray diffraction”, Hoboken: John Wiley and Sons, (2009).

[81] H.F. Poulsen, S.F. Nielsen, E.M. Lauridsen, S. Schmidt, R.M. Suter, U. Lienert, L. Margulies, T. Lorentzen, D.J. Jensen, “Three-dimensional maps of grain boundaries and the stress state of individual grains in polycrystals and powders”, Journal of Applied Crystallography, 34, 751-756, (2001).

[82] B.B. He, Introduction to 2D XRD, Bruker AXS Document # M86-E00055

APPENDICES

Appendix 1

A meshed model in Amira was saved as a file with extension of“. hmascii” which could be opened by notepad. Typical hmascii file is shown bellow which contains nodes coordinates, triangle faces and volumetric meshes. Here we are just interested in the nodes and faces. Because the original file was too large, the main body has been replaced with dots.

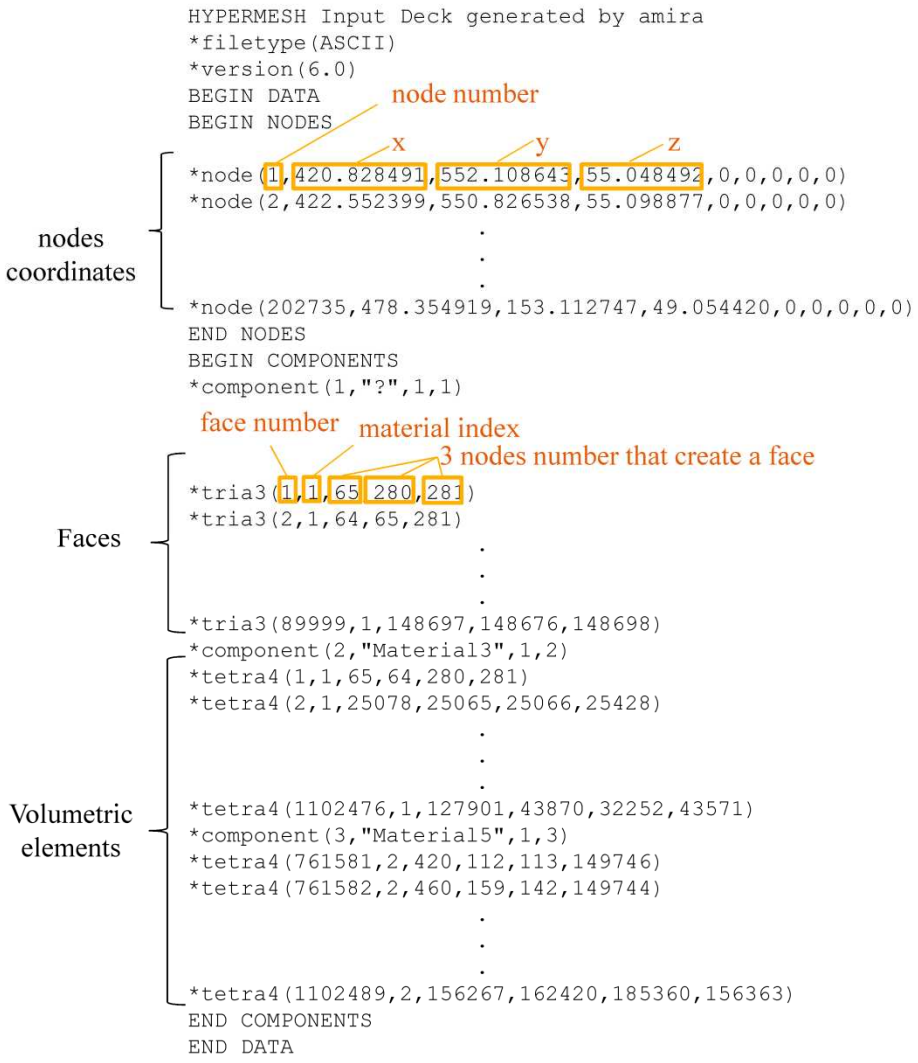

```
%Matlab code for minimum distance calculation
n=1;
x1=x(:); %face coordinates matrix imported to the workspace from
hmascii file
x2=sort(x1);
for i=1:length(x2)-1
    if x2(i+1)>x2(i)
        x3(n,1)=x2(i);
        n=n+1;
    end
end
for i=1:length(x3)
    x3(i,2)=nodes(x3(i),2);
    x3(i,3)=nodes(x3(i),3);
    x3(i,4)=nodes(x3(i),4);
end
n=1;
p1=p(:);
 p2=sort(p1);
for i=1:length(p2)-1
    if p2(i+1)>p2(i)
        p3(n,1)=p2(i);
        n=n+1;
    end
end
 for i=1:length(p3)
    p3(i,2)=nodes(p3(i),2);
    p3(i,3)=nodes(p3(i),3);
    p3(i,4)=nodes(p3(i),4);
end
ii=length(x3);
jj=length(p3);
% first let's calculate some initial value for dmin
for i=1:ii
    for j=1:1
        dmin(i)=((x3(i,2)-p3(j,2))^2+(x3(i,3)-p3(j,3))^2+(x3(i,4)-
p3(j,4))^2)^.5;
    end
end
%original loop for dmin
   for i=1:ii
    for j=1:jj
        d=((x3(i,2)-p3(j,2))^2+(x3(i,3)-p3(j,3))^2+(x3(i,4)-
p3(j,4))^2)^.5;
         if d<dmin(i)
             dmin(i)=d;
         end
    end
   end
   calib=11.5/550;
   dmin(2,:)=dmin(1,:)*calib;
%----------------histogram plot--------------------
   [muhat,sigmahat,muci,sigmaci] = normfit(dmin(2,:));
numbins = 25;
```

```
hist(dmin(2,:),numbins)
set(get(gca,'Children'),'FaceColor',[.8 .8 1])

hold on
hold on
[bincounts,binpositions] = hist(dmin(2,:),numbins);
binwidth = binpositions(2) - binpositions(1);
histarea = binwidth*sum(bincounts);
xh = binpositions(1):0.001:binpositions(end);
yh = normpdf(xh,muhat,sigmahat);
plot(xh,histarea*yh,'r','LineWidth',2)
xlabel('Porcelain layer thickness (mm)');
ylabel('Frequency');
```

Appendix 2

```
% Colored map of minimum distance measurement
% first lets calculate some initial value for dmin
 ii=length(nodes);
 jj=length(x3);
for i=1:ii
    for j=1:1
       dmin(i)=500;
     end
end
%orignal loop for dmin
d=0;
for i=1:ii
    for j=1:jj
        d=((nodes(i,2)-x3(j,2))^2+(nodes(i,3)-x3(j,3))^2+(nodes(i,4)-
x3(j,4))^2)^.5;
         if d<dmin(i)
             dmin(i)=d;
         end
    end
end

nodes(:,5)=dmin';

 %-------------------------------------------------------
c=0.5*ones(4080,3);
v=zeros(3,3);
for i=1:1:4080
      f=faces(i,(2:4));
      f1=f(1);
      f2=f(2);
      f3=f(3);
      faces(i,5)=dmin(f1);
      faces(i,6)=dmin(f2);
      faces(i,7)=dmin(f3);
```

```
      faces(i,8)=(dmin(f1)+dmin(f2)+dmin(f3))/3;
      v=[nodes(f1,2:4);nodes(f2,2:4);nodes(f3,2:4)];

   hold on;patch('Vertices',v,'Faces',[1 2 3],'FaceColor',[1 1-
faces(i,8)/max(faces(:,8))
faces(i,8)/max(faces(:,8))],'FaceAlpha',1)%spring;
%        axis equal;
       xlim([0 700]);
       ylim([0 700]) ;
       zlim([0 450]);
end

%---extra colors
% if faces(i,8)>=max(faces(:,8))/2
% %  hold on;patch('Vertices',v,'Faces',[1 2
3],'FaceColor',[2*faces(i,8)/(max(faces(:,8))) 0  0],'FaceAlpha',1)
% else
%       hold on;patch('Vertices',v,'Faces',[1 2 3],'FaceColor',[1 1-
faces(i,8)/(max(faces(:,8))) 0],'FaceAlpha',1)
% end
%     hold on;patch('Vertices',v,'Faces',[1 2
3],'FaceColor',[faces(i,8)/max(faces(:,8)) 1-faces(i,8)/max(faces(:,8))
1],'FaceAlpha',1)%cool;
%     hold on;patch('Vertices',v,'Faces',[1 2 3],'FaceColor',[1 1-
faces(i,8)/max(faces(:,8))
faces(i,8)/max(faces(:,8))],'FaceAlpha',1)%spring;
%     hold on;patch('Vertices',v,'Faces',[1 2 3],'FaceColor',[1-
faces(i,8)/max(faces(:,8)) 1
faces(i,8)/max(faces(:,8))],'FaceAlpha',1)%summer
%     hold on;patch('Vertices',v,'Faces',[1 2 3],'FaceColor',[0
faces(i,8)/max(faces(:,8)) 1-faces(i,8)/max(faces(:,8))
],'FaceAlpha',1)%Winter
%     hold on;patch('Vertices',v,'Faces',[1 2 3],'FaceColor',[1 1-
faces(i,8)/max(faces(:,8)) 0],'FaceAlpha',1)%Autumn
% hold on;patch('Vertices',v,'Faces',[1 2 3],'FaceColor',[.8-
faces(i,8)*0.8/max(faces(:,8)) .8-faces(i,8)*0.8/max(faces(:,8))  .8-
faces(i,8)*0.8/max(faces(:,8))],'FaceAlpha',1)%gary;
```

Appendix 3

a Matlab code was developed that calculates the required tilt and rotation angle for all data points using the z height matrix data.

```
%program for rotation and tilt Masoud allahkarami 2010 OSU
%target file saved using script file Run_Frame_X_Y_Z  5*700 ----RFXYZ
L1=length(RFXYZ);
%%initial input data was 25*28 matrix 700 data points 25=xL, 28=yL
xL=1;
count=1;
```

```
while count<=L1
    if count<L1 && RFXYZ(count,4)==RFXYZ(count+1,4)
       xL=xL+1;
         else
       count=count+ 2*L1;
    end
    count=count+1;
end

%input "yL",y length
yL=L1/xL;

%Rc Run column,%Fc Frame column,%Xc X column,% Yc column,%Zc Z column
Rc=RFXYZ(1:L1,1);
Fc=RFXYZ(1:L1,2);
Xc=RFXYZ(1:L1,3);
Yc=RFXYZ(1:L1,4);
Zc=RFXYZ(1:L1,5);
% xP, yP, x and y matrix that we need for plots they have origin at 0
and
% stepsize of Xc and Yc
xstep=abs(Xc(2)-Xc(1));
ystep=abs(Yc(xL)-Yc(xL+1));
xP=zeros(yL,xL);
yP=zeros(yL,xL);

for j=2:xL
     xP(:,j)=xP(:,j-1)+xstep;
end
for i=2:yL
     yP(i,:)=yP(i-1,:)+ystep;
 end
zmn=reshape(RFXYZ(1:L1,5),xL,yL);zmn=zmn';% matrix of height
zm=-zmn; %negative of height matrix (Useful for Excel modification)
%-------------------------------------------------------------------------
-
z=zm(:);
contourf(zm(1:yL,1:xL),10);figure(gcf);
hold on;
surfnorm(zm(1:yL,1:xL));view([-45 32]),colorbar;figure(gcf);

[Nx,Ny,Nz] = surfnorm(zm);
phi=atand(Ny./Nx);
%---------------------------------------------
phi360=[];
%---------------------------------------------
for i=1:yL
    for j=1:xL
        if  Nx(i,j)>=0 && Ny(i,j)>=0
            phi360(i,j)=phi(i,j);
        end
        if  Nx(i,j)<0 && Ny(i,j)>0
            phi360(i,j)=phi(i,j)+180;
```

```
        end
        if  Nx(i,j)<0 && Ny(i,j)<=0
            phi360(i,j)=phi(i,j)+180;
        end
        if  Nx(i,j)>=0 && Ny(i,j)<0
            phi360(i,j)=phi(i,j)+360;
            if phi360(i,j)==450;
                phi360(i,j)=450-180;
            end
        end

    end
end
%-----------------------------------------------
Lphi360=360-phi360;
Lphi90=90-Lphi360;
Sphi=180+Lphi90;
%-----------------------------------------------
Sfphi=Sphi;
for i=1:yL
    for j=1:xL
        if  Sphi(i,j)<0
           Sfphi(i,j)=360+Sphi(i,j);
        end

    end
end
% ------------------------------------------------

mat=0;
PhiRNx=[];
PhiRNy=[];
PhiRNz=[];
mat1=[];
for i=1:yL
    for j=1:xL
            r=[cosd(90-phi360(i,j))  -sind(90-phi360(i,j)) 0; sind(90-
...
            phi360(i,j)) cosd(90-phi360(i,j)) 0;0 0 1];
            v=[Nx(i,j), Ny(i,j), Nz(i,j)];
       mat=r*v';
       PhiRNx(i,j)=mat(1,1);
       PhiRNy(i,j)=mat(2,1);
       PhiRNz(i,j)=mat(3,1);
       mat1=[mat1 mat];

    end
end
%-------------------------------------------------------
chi=atand(PhiRNy./PhiRNz);
Schi=chi;
Sfphiinv= Sfphi';
SCulomnphi=Sfphiinv(:);
```

```
Schiinv=Schi';
SCulomnchi=Schiinv(:);
Sphichi=[SCulomnphi SCulomnchi];
%-------------------------------------------------------

rfxyz(1:L1,1)=RFXYZ(1:L1,1);
rfxyz(1:L1,2)=RFXYZ(1:L1,2);
rfxyz(1:L1,3)=RFXYZ(1:L1,3);
rfxyz(1:L1,4)=RFXYZ(1:L1,4);
rfxyz(1:L1,5)=RFXYZ(1:L1,5);
rfxyz=[rfxyz Sphichi];
```

Appendix 4

Prediction of the effect of the porcelain layer thickness (here for a fixed zirconia layer at 0.5 mm) on residual stress in particular positions of interest for the bottom of the zirconia layer, interface of the zirconia side, interface of the porcelain side, and top surface of the porcelain.

```
for j=1:1:400
    hold on
%---------------
% 2 & b index for upper layer
% 1 & a index for base layer t
ta=0.5;%layer thickness mm
tb=.05+j*.01;%layer thickness mm
T2=1173;
T1=273;
DT=T1-T2;
%------------1 & a----------------
ctea=11.3e-6;
CTEa=[ctea;ctea;0];
EL1=205;
ET1=EL1;
vLT1=0.22;
vTL1=vLT1;
GLT1=EL1/(2*(1+vLT1));
S11a=1/EL1;
S22a=1/ET1;
S12a=-vLT1/EL1;
S66a=1/GLT1;
```

```
Q11a=S22a/(S11a*S22a-S12a^2);
Q22a=S11a/(S11a*S22a-S12a^2);
Q12a=-S12a/(S11a*S22a-S12a^2);
Q66a=1/S66a;
Qa=[Q11a Q12a 0;Q12a Q22a 0; 0 0 Q66a];
a=DT.*(Qa*CTEa);
%------------2 & b----------------
cteb=10.3e-6;
CTEb=[cteb;cteb;0];
EL2=70;
ET2=EL2;
vLT2=0.22;
vTL2=vLT2;
GLT2=EL2/(2*(1+vLT2));
S11b=1/EL2;
S22b=1/ET2;
S12b=-vLT2/EL2;
S66b=1/GLT2;
Q11b=S22b/(S11b*S22b-S12b^2);
Q22b=S11b/(S11b*S22b-S12b^2);
Q12b=-S12b/(S11b*S22b-S12b^2);
Q66b=1/S66b;
Qb=[Q11b Q12b 0;Q12b Q22b 0; 0 0 Q66b];
b=DT.*(Qb*CTEb);
%-----------------------------------
N=(((ta+tb)/2)-(ta-(ta+tb)/2))*a+((ta-(ta+tb)/2)-(-(ta+tb)/2))*b;
M=0.5*(((ta+tb)/2)^2-((ta-(ta+tb)/2))^2)*a+0.5*(((ta-(ta+tb)/2))^2-(-
(ta+tb)/2)^2)*b;
A=ta*Qb+tb*Qa;
B=0.5*(((ta-(ta+tb)/2))^2-(-(ta+tb)/2)^2)*Qb+0.5*(((ta+tb)/2)^2-((ta-
(ta+tb)/2))^2)*Qa;
D=(1/3)*(((ta-(ta+tb)/2))^3-(-(ta+tb)/2)^3)*Qb+(1/3)*(((ta+tb)/2)^3-
((ta-(ta+tb)/2))^3)*Qa;
As=inv(A); %As=A*
Bs=-inv(A)*B; %Bs=B*
Cs=B*inv(A); %Cs=C*
Ds=D-B*inv(A)*B; %Ds=D*

Ap=As-Bs*inv(Ds)*Cs; %Ap=A'
Bp=Bs*inv(Ds); %Bp=B'
Cp=-inv(Ds)*Cs; %Cp=C'
Dp=inv(Ds); %Dp=D'
ABD=[Ap Bp; Bp Dp];
NM=[N;M];
e0k=ABD*NM;
e0=[e0k(1);e0k(2);e0k(3)];
k=[e0k(4);e0k(5);e0k(6)];
%-----------------------------------------

zmin=-(ta+tb)/2;
zmax=(ta-(ta+tb)/2);
zb=linspace(zmin,zmax,11);
for i=1:length(zb)
```

```
eb=e0+zb(i)*k-DT*CTEb;
sigmab(:,i)=Qb*eb;
end
zmin=(ta-(ta+tb)/2);
zmax=(ta+tb)/2;
za=linspace(zmin,zmax,11);
for i=1:length(za)
ea=e0+za(i)*k-DT*CTEa;
sigmaa(:,i)=Qa*ea;
end
%-----------------------------------------
sigma=[sigmab sigmaa];

z(j,:)=[zb za];
sigma1(j,:)=sigma(1,:);
plot(z(j,:),1000*sigma1(j,:),'-g')
grid on
result(1,j)=1000*sigma(1,1);
result(2,j)=tb;

result(3,j)=1000*sigma(1,11);

result(4,j)=1000*sigma(1,12);

result(5,j)=1000*sigma(1,22);

end
figure(2)
hold on
plot(result(2,:),result(1,:),'-g','LineWidth',2)
plot(result(2,:),result(3,:),'--g','LineWidth',2)
plot(result(2,:),result(4,:),'--r','LineWidth',2)
plot(result(2,:),result(5,:),'-r','LineWidth',2)


xlabel('Thickness of porcelain layer (mm)')
ylabel('Stress(GPa)')
legend('Zirconia Bottom Surface','Interface Zirconia side','Interface
Porcelain side','Porcelain top Surface' )
```

VITA

Masoud Allahkarami

Candidate for the Degree of

Doctoral of Philosophy

Thesis: X-RAY DIFFRACTION ANALYSIS OF RESIDUAL STRESS IN ZIRCONIA DENTAL COMPOSITES

Major Field: Mechanical Engineering

Biographical:

Education:

Completed the requirements for the Doctoral of Philosophy in Mechanical Engineering at Oklahoma State University, Stillwater, Oklahoma, USA, in December, 2012

Received Master of Science in Theoretical Physics at Urmia University, Urmia, Iran, in 2005

Received Bachelor of Science in Solid State Physics at Teacher Training University of Tehran (Tarbiat Moallem University), Iran, in 2002

Experience:

Research Associate at Material & Energy Research Center (MERC), 2006-2007

Professional Memberships:

- Phi Kappa Phi National Honor Society
- International Center for Diffraction Data (ICDD)
- Editorial board of Crystal Structure Theory and Applications (CSTA) Journal
- International Society of Automation (ISA)
- Society for Experimental Mechanics (SEM)
- American Ceramics Society (ACerS)
- American Physics Society (APS)
- International Society for Optics and Photonics (SPIE)
- American Concrete Institute (ACI)
- Iranian Nanotechnology Society, (INS)
- Institute of Transportation Engineering (ITE)
- International Association for Fire Safety Science (IAFSS)